Characterization of a carbon aerosol generator in a helium gas-jet for the extraction of fission products from the research reactor TRIGA Mainz

Martin Eibach

Diplomarbeit von

Martin Eibach

Institut für Physik
Johannes Gutenberg-Universität Mainz

Characterization of a carbon aerosol generator in a helium gas-jet for the extraction of fission products from the research reactor TRIGA Mainz

20. Mai 2009

Contents

List of Figures

List of Tables

Chapter 1

Introduction

The existence of more than 9000 different nuclides is predicted by recent nuclear models, whereas only about 3200 nuclides are presently known and investigated. They can be distinguished by their different nuclear ground-state properties like masses, half-lives and spins. About 12% of the known nuclides can be found in nature today with different abundances whereas most of the naturally occurring nuclides being stable [1].
Investigations of the origin of the universe showed that shortly after the Big Bang only hydrogen, helium and lithium were produced. Thus, the other elements emanate from nuclear fusion processes in stars, commonly referred to as stellar nucleosynthesis. The fact that the maximum of the binding energy per nucleon is at ^{56}Fe rises the question [2]: Why do the heavier elements exist and how were they produced? In the first phase of the primordial nucleosynthesis proton- as well as neutron-capture processes are assumed, which are followed by a β^+- and β^--decay, respectively. Two different neutron-capture processes are distinguished: Within a low neutron flux the (slow) s-process takes place, in which every neutron-capture is directly followed by a decay. At a high neutron flux the nucleus captures several neutrons and decays afterwards far away from the valley of stability in the so-called (rapid) r-process, which is alone responsible for the creation of half of the heavy elements. Each of the capture processes reaches some nuclei, where the reactions (n,γ) and (γ,n) are in a state of equilibrium. At these so-called waiting points the synthesis is waiting until a β^--decay enables further captures.
As nuclear ground-state properties reflect the interactions inside the nucleus, they determine the path of the different processes and thus, high precision data of masses, moments and half-lives are required to gain reliable interaction models of the nucleons, and a general understanding of the matter in the universe. Especially the mass is most important since it reflects the nuclear binding energy via Einsteins formula $E = mc^2$, whereas spins and moments contain informations about the nuclear shape and the distribution of the nucleons. High-precision measurements of the quantities, especially on short-lived nuclides far away from the valley of stability, are performed by mass spectrometric and laser spectroscopic facilities worldwide [3].
One of these facilities is TRIGA-SPEC, located at the research reactor TRIGA Mainz at the Institut für Kernchemie, University of Mainz, consisting of two branches, the trap

branch called TRIGA-TRAP, and the laser branch called TRIGA-LASER [4]. The goal of this facility is the online investigation of short-lived neutron-rich radionuclides produced by thermal neutron-induced fission of a fissionable target for the improvement of nuclear models, and a better understanding of the nucleosynthesis processes. In addition the trap branch extends the range of directly measured high-precision mass data to the transuranium region by offline mass measurements on long-lived heavy nuclides up to californium. TRIGA-TRAP is a double Penning trap mass spectrometer where the mass measurement of the nuclide of interest is based on the determination of the cyclotron frequency ν_c of the stored ion [3]: $\nu_c = qB/(2\pi m)$. TRIGA-LASER aims for the investigation of nuclear spins and moments by the measurement of isotope shifts and hyperfine structure splittings using collinear laser spectroscopy [5].
Since short-lived radionuclides are not available in nature they must be produced in the laboratory. They can be obtained at the research reactor TRIGA Mainz by thermal neutron induced fission of a target [6], are slowed down and transported out by a gas-jet system. Chapter 2 gives an overview of the production of radionuclides and the extraction principle and introduces the TRIGA-SPEC experiment. Due to the relatively low mass of the fission products a transport medium is needed. Therefore carbon aerosols will be used to which the fission products attach. The principle of carbon aerosol production is explained in Chap. 3 including a description of the detection and size classification. Since nearly every mean of aerosol production can not generate only one single size, it is necessary to examine the size distribution of the aerosol particles. This requires an explanation of the origin of the size distribution and the determination of the produced aerosol amount as well as the mean of the size distribution as function of different parameters. For the use of aerosols under experimental conditions it is also important to assure the longterm stability of the aerosol production.
The focus of Chap. 4 is the extraction of the fission products. For a differentiated understanding of the extraction it will be pointed out, how it is possible to verify the energy calibration of a germanium-lithium detector and which fission products can be identified by the means of gas-jet transport and γ-spectroscopy. Two different ways of spectral data evaluation will be introduced for the examination of the fission product extraction. Since the extracted radionuclides decay, the time that is needed to extract the fission products is an important limiting factor. It is essential to know this time to be able to estimate, which radioactive species are in principle available for further investigations after extraction. The production rate is defined by target and reactor properties. Since they can not be changed easily to gain a several orders of magnitude higher production it is required to extract the fission products as efficient as possible, which is addressed in detail in Chap. 4. Another limit is the number of particles that are available for investigation. Thus it is important to know their absolute number in order to estimate whether enough particles are available for measurements or not. These numbers will be calculated from the data used for the transport efficiency measurement to have comparable values, which requires an efficiency calibration of the detector. In addition some assumptions are made due to target geometry and absorption processes.

Chapter 2

Principle of production, extraction and usage of radionuclides at the research reactor TRIGA Mainz

For the determination of the properties of radionuclides numerous radioactive ion beam facilities have been set up worldwide [7–12]. In order to gain access to as many nuclides as possible different production methods have been used: Accelerator facilities produce mainly neutron-deficient nuclides by the bombardment of a heavy target with light charged particles like protons [9] or ^{4}He nuclei and by an increase of the projectile mass heavy and super-heavy elements can be produced [8]. A distinction is drawn between ISOL/IGISOL [9, 10] and fragmentation [13] facilities where the radionuclide production is realized by the bombardment of a thick and a thin target, respectively. In opposition to accelerators nuclear reactors deliver neutrons and thus provide access to the neutron-rich area of the nuclide chart by induced fission of a fissionable target. As the fission yield depends on the material [14] different nuclides from ^{227}Th to ^{249}Cf can be used as targets to gain the maximum yield for different mass regions. Instead of the radionuclide production by thermal neutron-induced fission it is possible to use a material that fissions spontaneously as it was realized with ^{252}Cf at the CARIBU experiment [15].
In this chapter the fission process and the function of the research reactor TRIGA Mainz are introduced and the TRIGA-SPEC experiment for investigations of nuclear ground-state properties is presented [4] . The main focus is on the helium gas-jet and aerosol generator system, which was built up and characterized in the context of this thesis and is used for extraction of fission products from the reactor.

2.1 The fission process

In order to explain why fission of a nucleus can occur, it is necessary to understand the composition of the binding energy of a nucleus. Therefore the liquid drop model, the first developed nuclear model, is introduced here before the neutron induced fission process is

discussed. Despite the development of numerous nuclear models, as e.g. Duflo-Zuker [16], the liquid drop model describes the nuclei still most precisely [17].
The liquid drop model describes the nucleus as an analogy to an incompressible homogeneously charged liquid drop. Its binding energy is described by Weizsäcker's semi-empirical formula consisting of five different terms: [18]

$$E = E_V - E_S - E_C - E_{Sym} + E_P \quad . \tag{2.1}$$

The nucleus is hold together by nuclear forces with a small range that allow only interactions of the nucleons with their closest neighbors. Therefore, the estimation $E_V \propto A$ of the volume energy is made with A being the atomic mass number, i.e. the number of nucleons. The surface correction $E_S \propto A^{2/3}$ is necessary as nucleons at the surface of the sphere have less neighbors than the ones inside. Due to the charge of the protons the repulsive coulomb correction $E_C \propto Z(Z-1)A^{-1/3}$ represents the interactions of one proton with the others. Both remaining terms are the result of observations that showed that nuclides i) with the same number of neutrons and protons are more stable than others, which results in the symmetry correction $E_{Sym} \propto (N-Z)^2/4A$, and that ii) an even number of protons or neutrons stabilizes the nucleus in addition. This is represented by the pairing term

$$E_P \propto \delta\, A^{1/2} \tag{2.2}$$

with δ being $+1$ for nuclei with even numbers of protons and neutrons, -1 for nuclei with odd numbers of protons and neutrons and otherwise 0.
A small deformation of the nucleus increases the surface and therefore reduces the binding energy. At the same time the distance of the protons is increased and thus the Coulomb repulsion decreased. In this case fission is impossible as long as E_C and E_S compensate each other as the binding energy did not change and the nucleus is still stable. According to Bohr and Wheeler [19] spherical drops can be parameterized by the radius vector $R(\theta)$ in terms of Legendre polynomials due to a multipolar expansion:

$$R(\theta) = R_0 \left(1 + \sum_{n=1}^{\infty} \alpha_n P_n(\cos(\theta))\right) \quad . \tag{2.3}$$

For the examination of small distortions they found that $\Delta E_C = -\frac{1}{5}\alpha_2^2 E_C$ and $\Delta E_S = \frac{2}{5}\alpha_2^2 E_S$, where ΔE_C is the change in the Coulomb correction, ΔE_C is the change in the surface correction and α_2 is the quadrupolar coefficient of $P_2(\cos(\theta))$ from Eq. (2.3). Thus, they showed that nuclei will be unstable if

$$\frac{E_C}{2E_S} > 1 \quad . \tag{2.4}$$

According to this equation the liquid drop model predicts one saddle point in the potential as a function of the deformation of the nucleus and in addition a spherical shape for all stable nuclei. Observations showed that this is an inadequate description as both are not

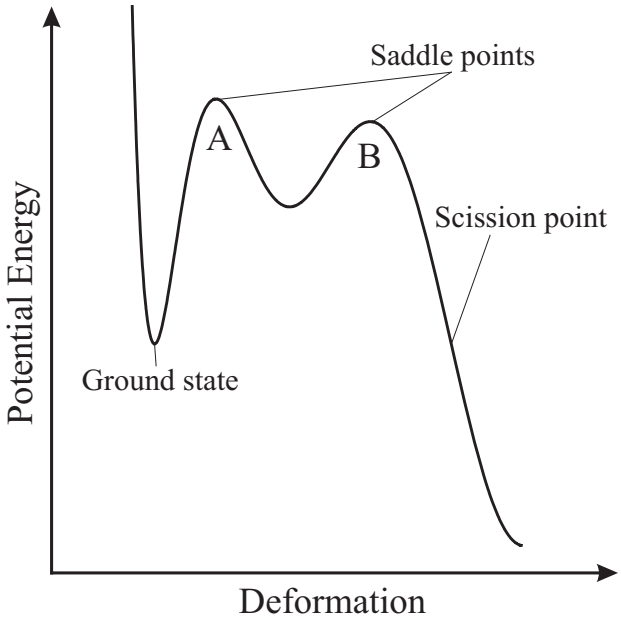

Figure 2.1: Potential energy of a heavy nucleus as a function of the deformation. The fission barrier is marked with the two thresholds A and B, respectively. A can be explained with the liquid drop model, B is introduced with the shell corrections.

consistent with observations for actinide nuclides. This problem can be solved with the so-called shell corrections [20] that predict a double potential barrier [21] as shown in Fig. 2.1. As thermal neutron fission is the dominating process for the fission in a nuclear reactor at which TRIGA-SPEC is situated, the focus will be on this process for further explanations. In the case of nuclides that are fissionable by thermal neutrons the energy that is released by the bond of the neutron to the nucleus is sufficiently high to excite the nucleus to an energy above the fission barriers A and B shown in Fig. 2.1, since the kinetic energy of the neutron is very low. According to Weizsäcker's formula Eq. (2.1) and Eq. (2.2), the binding energy is especially for odd numbers of protons and neutrons very low and thus, heavy nuclides with an odd number of neutrons are fissionable since additional energy is released due to the pairing term after neutron capture. Due to the shell corrections to the liquid drop model nuclides with an even number of neutrons can be fissioned as well by thermal neutrons but with orders of magnitude smaller cross sections [24].
A general formulation for the low-energy fission is

$$\mathrm{A} + \mathrm{n} \rightarrow \mathrm{B} + \mathrm{D} + \lambda\mathrm{n} + \Delta E \quad , \tag{2.5}$$

which expresses that by the fission of a nuclide A induced by the capture of one neutron n, the two nuclides B and D as well as λ neutrons are generated and the energy ΔE is emitted. λ is a statistical value and is typical for the fissioned material (e.g. $\lambda = 2.4$ for ^{235}U, $\lambda = 2.9$ for ^{239}Pu). The illustration of the fission process is shown in detail in Fig 2.2. Fission is initiated by the capture of a neutron as an energy of about 6 MeV is released after its bond to the nucleus. This causes an excitation of the nucleus with strong deformation

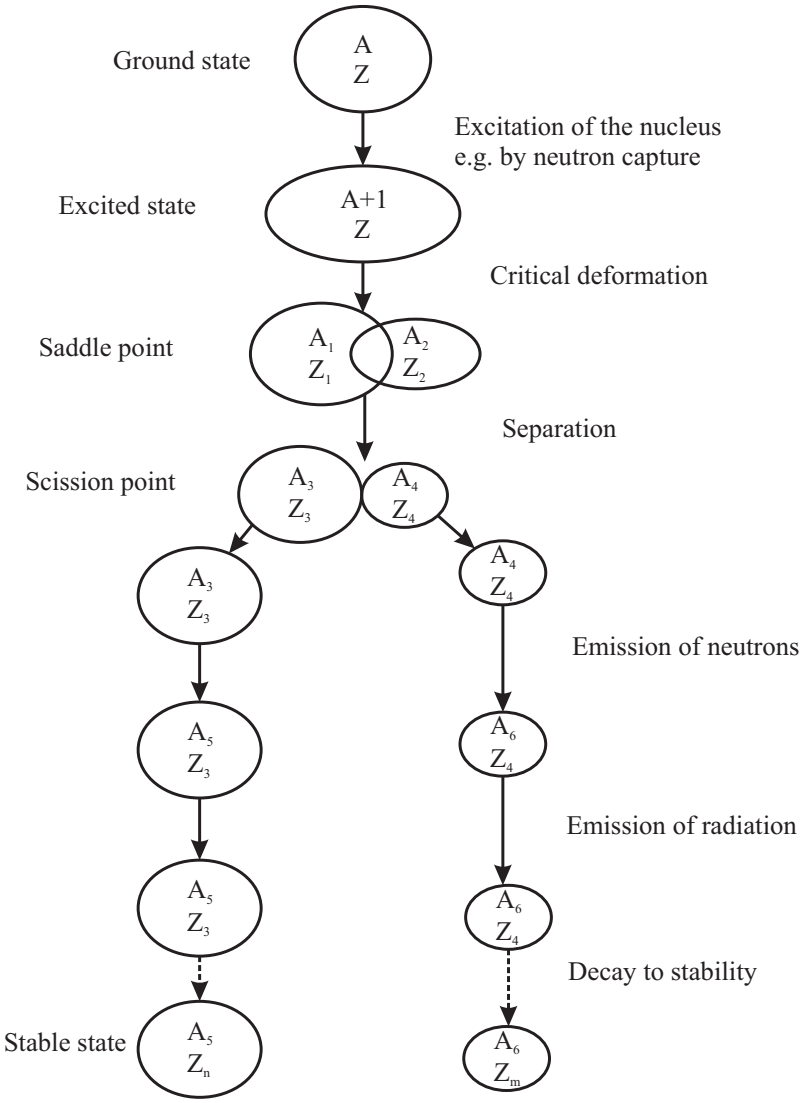

Figure 2.2: Different steps during nuclear fission. If energy is supplied to a fissionable nucleus, e.g. by neutron capture, the nucleus is excited, constricts after $\approx 10^{-15}$ s until the fission takes place. The fission products gain kinetic energies up to 100 MeV, emit neutrons and γs until they end as stable nuclei.

vibrations while the nuclear forces constrain the nucleus to the ground state shape. After approximately 10^{-15} s the deformation has reached the saddle point of the potential and the nucleus is separated after additional 10^{-20} s. Due to the Coulomb repulsion the two fragments are separated and lower their energies by the emission of prompt neutrons and γ-radiation. After a series of β^--decays these nuclides reach the valley of stability [25]. A small fraction of neutrons, about 0.7% for ^{235}U [26], is emitted after a delay of 0.08 s to 100 s when a nucleus reaches an highly excited state after a β^--decay.
Generally the mass distribution of fission products is asymmetric for thermal neutron

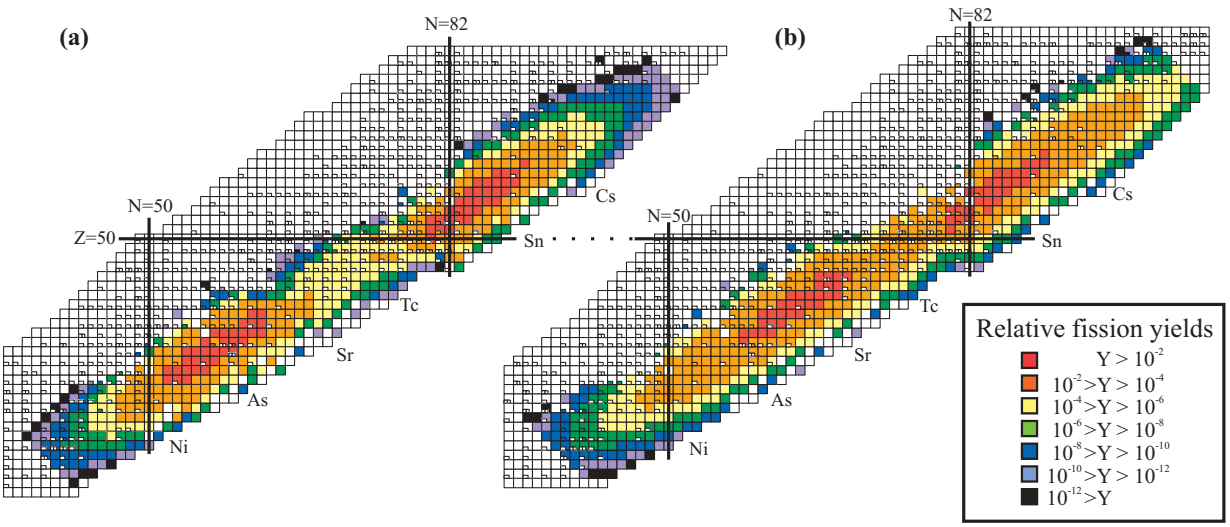

Figure 2.3: Thermal neutron fission yields of (a) ^{235}U and (b) ^{249}Cf. The maximum yield of the lighter fission products deviate to heavier masses by an increase of the mass of the fissioned nuclide whereas the maximum of the heavy fission products remains approximately the same [22, 23]. The production rates for the test target that was used within this thesis is presented later.

induced fission [27]. As shown in Fig. 2.3(a), where the colors indicate the relative fission yields of the nuclides, there are two maxima for the fission of ^{235}U, one around mass number A=100 the second at about A=138. Since nuclides apart from the maxima are produced with an orders of magnitude less amount, symmetric fission is about three orders of magnitude smaller than asymmetric fission. In Fig. 2.3(b) the fission yields for ^{249}Cf are shown and it becomes apparent that the maximum of the light fission products are shifted towards heavier masses whereas the maximum of the heavy fission products remains at the same position. Its position is at about $A = 138$ near the doubly magic nucleus ^{132}Sn. Experimental data showed in general that the maximum of the light fission products increases with the mass of the fissioned nuclide until symmetric fission as dominating process is reached for ^{258}Fm [22]. Thus, in case of the light branch the yield of the nuclide of interest can be increased by selection of an appropriate target material. The fission of light nuclides with $Z \leq 85$ results in symmetric fission as well.
If other projectiles as e.g. high energetic neutrons are available, the fission yields become symmetric due to the faster direct fission process at higher energies. In addition, other nuclear reaction processes like the emission of a proton or an α-particle can occur. Fission induced with protons or heavier charged particles show a similar behavior but with lower fission yields since high energies are required due to the Coulomb repulsion.
At the research reactor TRIGA Mainz uranium, plutonium and californium targets are used routinely as targets for fission induced by thermal neutrons. In the following the reactor is described.

2.2 The research reactor TRIGA Mainz

The research reactor TRIGA[1] Mainz was built in 1965 by the company General Atomic [28] and is a freestanding reactor located at the Institut für Kernchemie at the Johannes Gutenberg-Universität in Mainz. It is a light water cooled reactor equipped with 76 fuel moderator elements of an alloy of uranium-zirconium-hydride (UZrH) with an enrichment of about 20 % in ^{235}U. The cylindrical elements with a length of 72.2 cm and a diameter of 3.5 cm are placed inside a 20 m^3 aluminium tank surrounded by a concrete shield. Two control rods and one pulse rod made of boron carbide or boron nitride, respectively, are used for power regulation.
Two different operation modes are possible: (i) In the steady-state mode the reactor can be operated at power levels from 100 mW$_{\mathrm{th}}$ to 100 kW$_{\mathrm{th}}$, which corresponds to thermal neutron fluxes in the order of 10^5n/ (cm^2 s) to 10^{11}n/ (cm^2 s). The maximum fluxes of thermal neutrons are shown in detail in Tab. 2.1 for different irradiation positions. (ii) The TRIGA reactor can also be operated overcritical, i.e. in the so-called pulse mode [29] with a maximum allowed power of 250 MW$_{\mathrm{th}}$. Under these conditions the pulse width is about 30 ms. The inherent safety of the reactor allows the safe operation in the pulse mode. Due to composition of the fuel matrix [30], the neutrons are mainly moderated by interactions with the hydrogen in the UZrH alloy. If the fuel temperature increases, e.g. if one moderator rod is removed very fast, the neutrons lose less energy in collision with the hydrogen atoms due to the high thermal energy of the hydrogen. Thus the neutrons cause less fissions due to smaller cross sections at higher energies and escape to the water where they are moderated. If such a thermal neutron penetrates a fuel element, its energy is increased again due to the higher temperature of the rod. Hence, the chain reaction is aborted within a few milliseconds, faster than any engineered device can operate. By the consideration of the activity A after an irradiation of N atoms for a time t

$$A = \sigma \Phi N \left(1 - e^{\lambda t}\right) \quad , \tag{2.6}$$

with the neutron capture cross section σ, the neutron flux Φ, and the decay constant $\lambda = \frac{\ln 2}{T_{1/2}}$, it is obvious that a short irradiation time suppresses activity of long-lived radionuclides. Thus the pulse mode is ideal for investigations on short-lived radionuclides up to half-lives of 55 s due to the high neutron flux and the short irradiation time [29].
Sufficient radiation protection is provided by the surrounding concrete shielding and the

Irradiation position	thermal neutron flux / n/ (cm^2 s)
rotary specimen rack	7×10^{11}
pneumatic transfer system	1.6×10^{12} – 1.8×10^{12}
beam tubes	1.0×10^{11} – 5.4×10^{11}

Table 2.1: Thermal neutron fluxes at different irradiation positions at TRIGA Mainz for a power of 100 kW$_{\mathrm{th}}$.

[1] Training Research Isotope production General Atomic

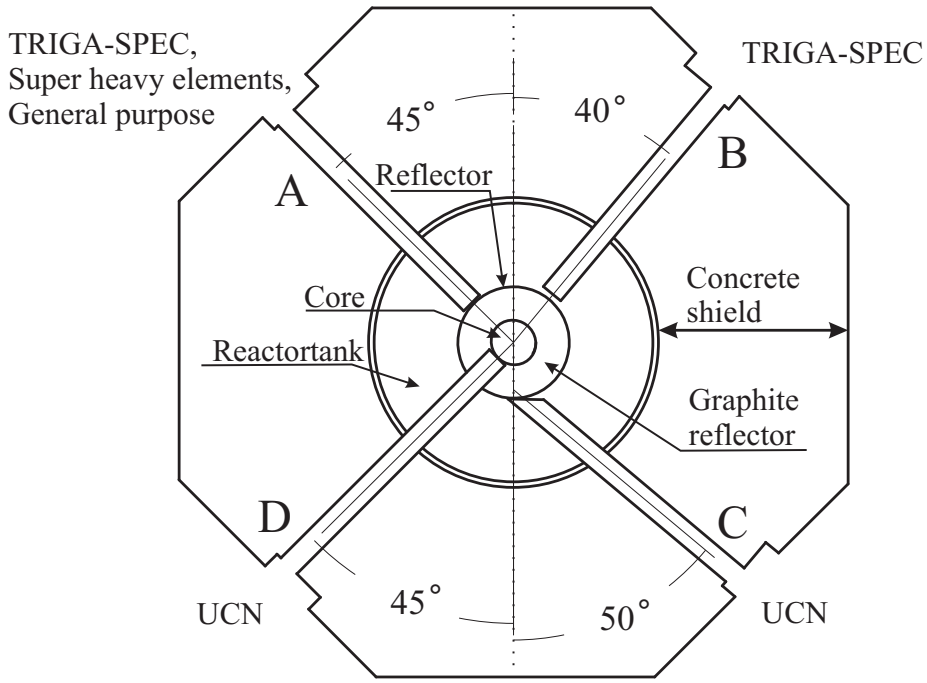

Figure 2.4: Beam tube arrangement at the research reactor TRIGA Mainz. The beamports provide different neutron fluxes. Whereas the flux at A and B is almost equal, the flux at D is substantially higher, since the beam tube points directly to the reactor core through a hole in the graphite reflector. The TRIGA-SPEC experiment is located at beamport B with a maximal neutron flux of $1.8 \times 10^{11} \frac{\mathrm{n}}{\mathrm{cm}^2\,\mathrm{s}}$ at 100 $\mathrm{kW_{th}}$. Beamport A serves as a test station for the studies of the radionuclide transport and detection with aerosols performed within this thesis and for further tests concerning the on-line coupling of TRIGA-SPEC to the reactor.

approximately 5 m shielding water, which provides the opportunity to work near and on the reactor or to place and remove samples during full power operation.
The TRIGA reactor offers different positions that can be used for irradiations. For isotope production and neutron activation analysis a rotary specimen rack with 80 irradiation positions can be used at a rather constant neutron flux due to the continuous rotation of a sample around the reactor core. As the samples have to be inserted and removed manually it is impossible to extract them in a sufficient time for the work with short-lived radionuclides. Therefore the reactor is equipped with pneumatic transfer systems, which achieve transport times of one to five seconds. For a very low epithermal neutron flux the thermal column can be used, which is a huge graphite block with an irradiation position that ensures a very good moderation. As an advantage of a freestanding reactor the TRIGA Mainz is equipped with four beam tubes, which are located in the arrangement shown in Fig. 2.4, pointing to the reactor core. In beam port B different targets can be irradiated to produce short-lived nuclides for further investigations at the TRIGA-SPEC facility, which is presented in section 2.4.

2.3 Gas-jet transport systems

Gas jets are in use since the 1960s [31] to transport radioactive nuclides from the production site to an accessible region with a low background count rate. The method is based on the principle that nuclear reaction products recoiling out of a thin target are thermalized in a gas cell, attach to the aerosol particles that are continuously fed in with a carrier gas and are flushed out through a capillary to the experimental area. After the production radionuclides have energies up to a few 100 MeV and therefore a maximum range of several ten centimeters in light gas at atmospheric pressure. To avoid losing the fission products by attaching to the walls of the target chamber it is necessary to reduce their range in the gas by increasing the density of the gas. The energy loss can be estimated with the Bethe-Bloch-Formula [32]

$$-\frac{\mathrm{d}E}{\mathrm{d}x} = \frac{z^2 e^4 n_e}{4\pi\varepsilon_0^2 c^2 m_e \beta^2}\left(\ln\frac{2m_e c^2\beta^2}{I(1-\beta^2)} - \beta^2\right) \tag{2.7}$$

with the electron density of the material n_e, the charge number of the particle z and the average ionization potential of the material I. The energy loss is proportional to the density of the material for the non-relativistic case and due to $n_e = \frac{Z}{A}\rho N_a$:

$$-\frac{\mathrm{d}E}{\mathrm{d}x} \propto \rho \quad . \tag{2.8}$$

Thus an increase of the gas density increases the energy loss of the fission products as well and therefore their range in the gas is reduced. This can either be assured by the use of a heavier non-reactive gas like argon or by an increase of the pressure, which is according to the law of Boyle and Mariotte

$$p\,V = m\,p/\rho = \text{const.} \tag{2.9}$$

directly proportional to the pressure. Typical ranges of fission products for different pressures and gases are presented in Tab. 2.2. As the whole system is flushed with gas, an increase of the pressure can just be assured by an increase of the gas flow.
For short distances and therefore short capillaries of a few centimeters length the transport can be realized with pure gases especially helium but is rather impossible for longer distances [34] as the particles attach to the capillary when they reach its walls due to diffusion and are lost. According to [35] the distance between a particle and the center of the capillary after a certain time t is given by

$$d = tNl = tv_D = t\sqrt{2E/m} \tag{2.10}$$

with the mean free path l, the number of collisions per second $N = v_D/l$ and the diffusion velocity v_D. As the velocity of a particle can be expressed with its mass m and energy $E = \frac{f}{2}k_B T$ with temperature T, degrees of freedom f and Boltzmann constant k_B, the distance is proportional to

$$d \propto \sqrt{T/m}\,. \tag{2.11}$$

Pressure / bar	Range in N_2 / mm	Range in ^{4}He / mm	Range in ^{40}Ar / mm
1.0	26.0	144	26.7
1.5	17.3	96	17.8
2.0	13.0	72	13.4
2.5	10.4	58	10.7
3.0	8.7	48	8.9

Table 2.2: Ranges of ^{102}Mo in different gases at different pressures [33]. The range of particles in nitrogen and argon are almost equal although their atomic masses are 14 amu and 40 amu respectively. This is due to the formation of nitrogen molecules as they have a low ionization potential, which increases the energy loss during transmission through matter according to Eq. (2.7)

Usually the decrease of the gas temperature is not an option because of the capillary length. Hence, the diffusion can only be damped by an increase of the mass of the particles the radionuclides attach to. This is realized by the insertion of aerosols into the gas. These aerosols are produced in the gas flow and have typical sizes of about 10 nm − 1000 nm, so that their mass is in the order of $(10^5 - 10^{11})$ amu to avoid attaching to the capillary due to diffusion.
According to Stokes' law the sedimentation of heavy aerosols due to gravity is analogous to Eq. (2.11)

$$d \propto m \ . \tag{2.12}$$

Hence, light aerosols attach to the capillary due to diffusion, heavy aerosols sediment due to the influence of gravity or inertia. Thus, neither light nor heavy aerosols can transport the fission products sufficiently, which means that medium-heavy particles are required. Different materials like carbon, KCl or NaCl can be used due to the intended application. A detailed description of the production and investigation of carbon aerosols and their use is given in the next chapter as they have been used for the first time at TRIGA Mainz within this thesis. A sketch of the principle is shown in Fig. 2.5.
After the thermalization it is assumed that two processes effect the attachment of radionuclides to the aerosols, diffusion and impaction. Impaction into the aerosols is a very improbable process because the geometric cross section of the aerosols is very small due to their density of about $10^6\,\mathrm{cm}^{-3}$ and their average size of approximately 100 nm. As the energy of the fission products is high before thermalization electrostatic effects can be neglected and thus it is sufficient to estimate the geometric cross section, which is comparably small. Therefore diffusion is the dominating process for which it is assumed that the nuclides attach to the aerosols with the first physical contact whereas the exact process is still unknown [36].
In the case of spherical particles it is possible to estimate the diffusion agglomeration. The

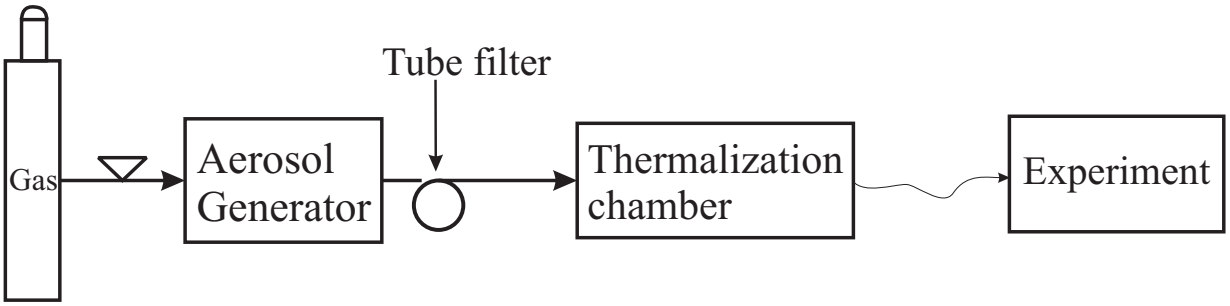

Figure 2.5: Sketch of the gas-jet principle. Aerosols are produced in a gas atmosphere and guided to the target chamber where thermalized radionuclides attach to them and are flushed out through a capillary to the experiment.

attachment coefficient for a neutral atom to a large particle can be expressed as [37]

$$\beta_0 = \frac{\pi\, v\, R_P^2}{1 + \frac{v\, R_P}{4\, D} \times \frac{1}{1+\frac{\lambda_D}{R_P}}} \tag{2.13}$$

with the diffusion constant of an atom D, the radius of the aerosol R_P, the average thermal velocity of the atom v and the mean free path of the atom λ_D. This expression can be approximated for large mean free paths and small velocities with

$$\beta \approx \pi\, v\, R_P^2 \tag{2.14}$$

and is thus approximately proportional to the surface of the aerosols. The coefficient for ions is given by

$$\beta_\pm = \frac{\pi\, v\, R_P^2 \left(1 \pm \sqrt{\pi\, y}\right)}{1 + \frac{v\, R_P}{4\, D}} \tag{2.15}$$

with $y = q^2/2RkT$ and therefore also the attachment of ions is proportional to the aerosol surface for small velocities. This is an important fact because due to the ionizing β- and γ-radiation in accelerator facilities or nuclear reactors it is necessary to know the influence charges cause on the attachment process. For low charge states the relation $\beta \propto R_P^2$ is still valid.

During the transport it is necessary to preserve a laminar flow in the system as occurring turbulences can force the aerosols to touch the wall of the thermalization cell. Therefore crucial points are at positions where the laminar flow is expanded or compressed, e.g. at the entrance of the capillary. The transport time through the capillary is determined by the pressure gradient between its beginning and end. With a large gradient it is possible to increase the gas flow up to the sonic speed in the gas under laminar flow conditions. At higher speeds the flow will become turbulent due to developing shock waves and thus a large amount of aerosols will be lost. As aerosols and gas have the same velocity in the capillary the minimum of the transport time is determined by the used gas [38].

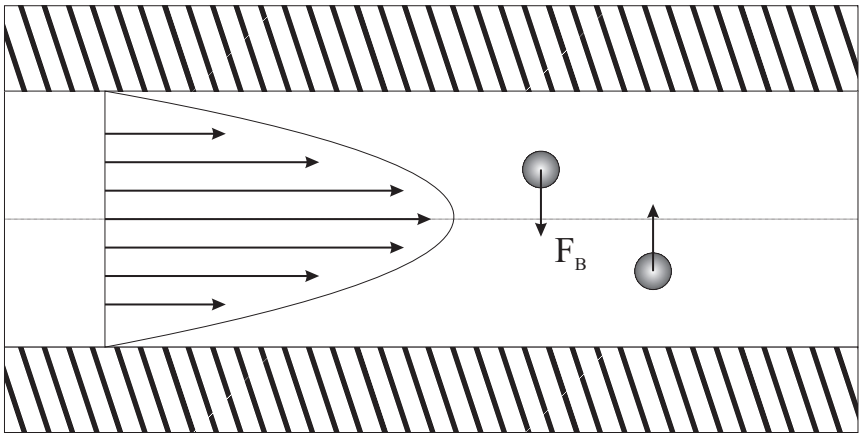

Figure 2.6: The parabolic velocity distribution across the cylindric shape causes a force F_B on the particles, which points to the center of the capillary.

Though there are many effects that decrease the transport efficiency by forcing the aerosols to touch the wall, there is also one effect which causes the return of the aerosols to the center of the capillary: According to inner friction of different layers in fluids and gases under laminar flow conditions, the velocity is parabolically distributed in a cylinder with the maximum in the center. That implies considering Bernoulli's law a force directed to the center (see Fig. 2.6). Another effect is the occurrence of so-called dead water turbulences at the entrance of the capillary. They cause that the gas containing the aerosols can only enter at the center [35].

2.4 The TRIGA-SPEC experiment

The reactor TRIGA Mainz, where the TRIGA-SPEC experiment is located [4], is an ideal facility to get access to short-lived neutron-rich radionuclides. For mass spectrometric and laser spectroscopic studies a double Penning trap mass spectrometer as well as a collinear laser spectroscopy beamline are being installed. A sketch of the planned experimental setup is shown in Fig. 2.7, a photo of the already existing TRIGA-SPEC experiment is presented in Fig. 2.8. It consists of two branches, the trap branch called TRIGA-TRAP and the laser branch called TRIGA-LASER. The TRIGA-TRAP beamline has been completed and currently offline mass measurements are performed, whereas the TRIGA-LASER experiment is under construction but first fluorescence signals have been obtained recently. The online coupling of TRIGA-SPEC is still incomplete whereas the ECR ion source is already in position. The separator magnet and the radiofrequency quadrupole ion beam cooler and buncher will be installed in 2010.

In order to produce the nuclides of interest a chamber containing a heavy-element target, that is fissionable by thermal neutrons, is placed inside the reactor near the core. Three different targets are presently available for radioactive isotope production: 310 μg of ^{235}U, 300 μg of ^{239}Pu and 310 μg of ^{249}Cf, which provide different amounts of fission products due

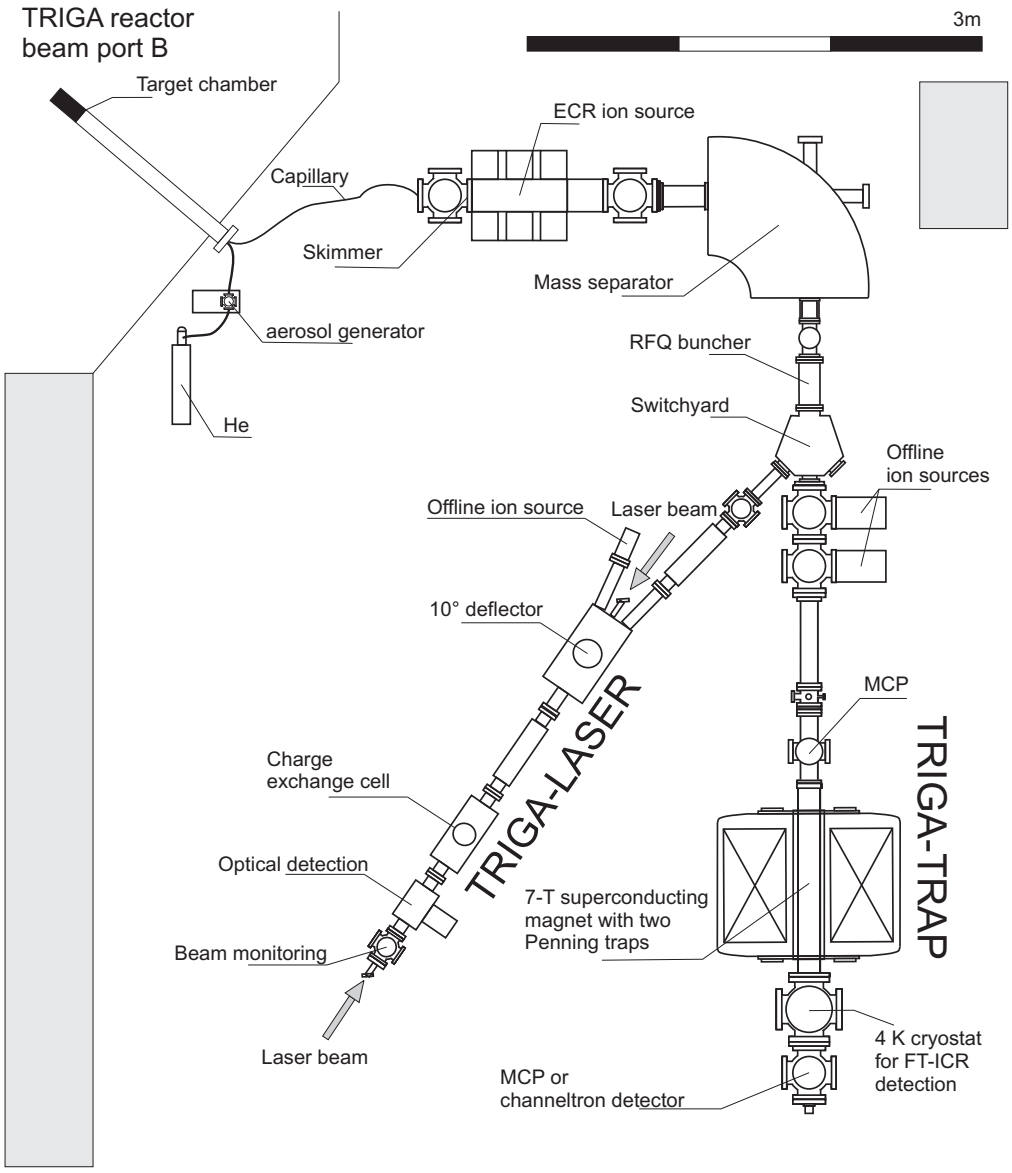

Figure 2.7: TRIGA-SPEC setup with the mass spectrometry experiment TRIGA-TRAP and the laser spectroscopy beamline TRIGA-LASER.

to different fission cross sections and fission yields. Inside the target chamber the radionuclides created by fission are thermalized in a helium gas atmosphere at an overpressure of about 1.7 bars and attach to the provided carbon aerosols. The gas-jet system and the aerosol generator were set up and tested within this thesis. The aerosols with attached fission products are flushed out through a capillary into a vacuum region where the helium is pumped away by a $275\,\mathrm{m}^3/\mathrm{h}$ roots pump down to a pressure of about 10^{-1} mbar. In the expanding gas-jet the aerosols with the fission products remain in the center due to their inertia. Thus, the helium can be efficiently separated from the aerosols by using a skimmer.

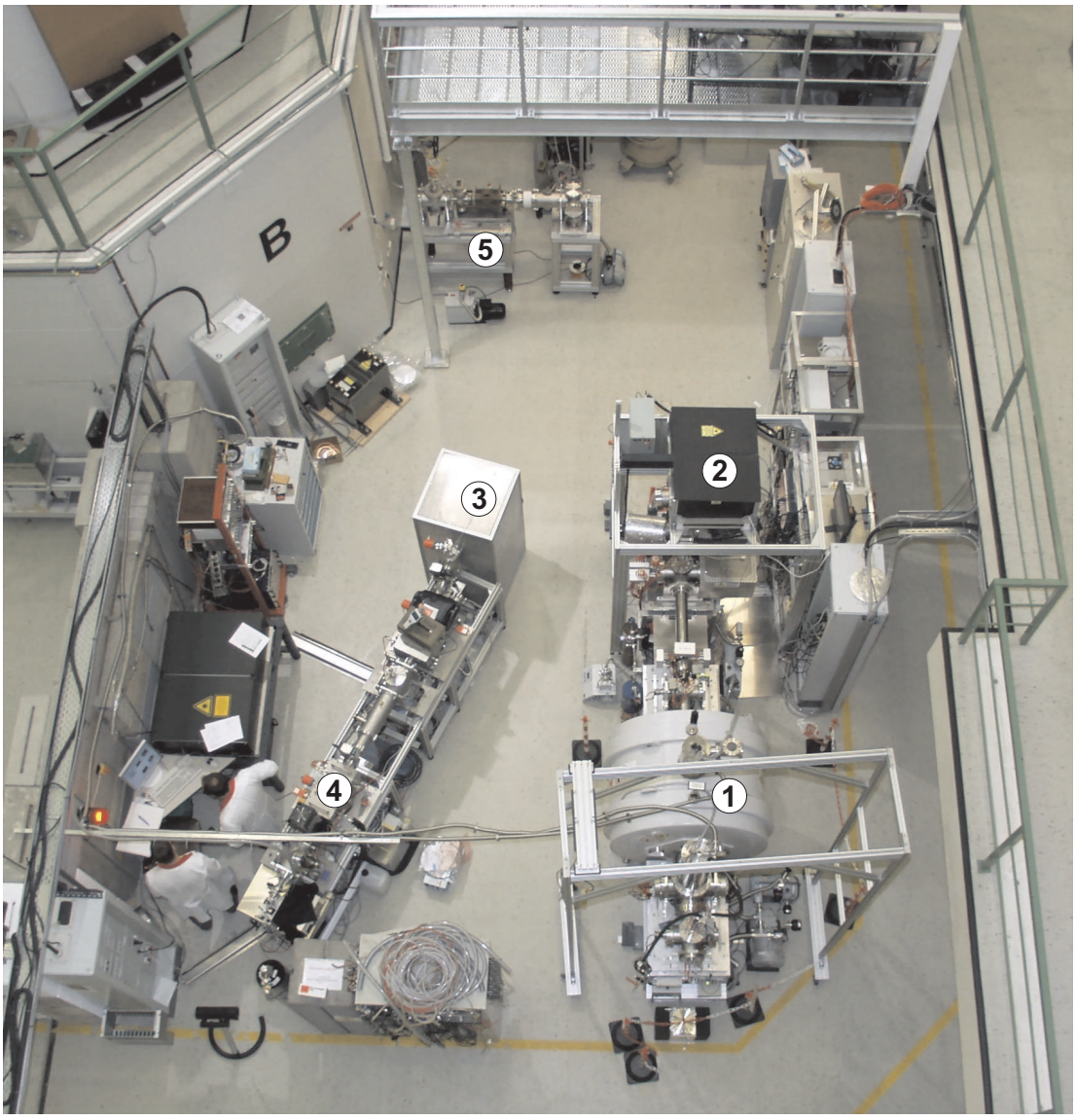

Figure 2.8: Photography of the TRIGA-SPEC setup. On the right the TRIGA-TRAP experiment with the superconducting magnet (1) is located. A laser ablation ion source [39] and a surface ion source (2) provide a variety of ion species for offline studies. The TRIGA-LASER setup on the left is being set up, whereas an offline ion source (3), a charge exchange cell (4), a 10° deflector and the detection system are already visible. Also the ECR ion source (5) is in position.

After the separation the particles will be injected into an ECR ion source [40, 41] where the fission products get detached from the aerosols and ionized by electron impact. For this purpose a plasma is confined in a magnetic field minimum due to the magnetic mirror effect. The electrons in the plasma are heated by a 2.45 GHz microwave on a closed surface of constant magnetic field strength, where the radiofrequency matches the cyclotron

frequency of the electrons. Thereby, high energetic electrons for the ionization process are provided. Ions will be extracted from the plasma by an electrode of Pierce geometry, which is on negative potential with respect to the plasma tube. Isobaric selection of the fission products with a mass resolution $\Delta m/\ m = 1000$ is foreseen by a 90° dipole magnet with a bending radius of 0.5 m and a magnetic field up to 1.12 T, which allows the mass selection for isotopes up to californium with acceleration voltages up to 60 kV. The selected isotopes will be guided to an electrostatic 45° switchyard, similar to the one at ISOLDE [9], and finally delivered either to the Penning trap mass spectrometer TRIGA-TRAP or the collinear laser spectroscopy beamline TRIGA-LASER. In case carbon cluster ions can be extracted from the ECR source they could be used for calibration purposes in precision mass spectrometry.
After first online tests, techniques to improve the sensitivity will be integrated to the setup such as beam cooling and bunching. Therefore a radiofrequency quadrupole (RFQ) ion beam cooler and buncher will be placed in front of the switchyard. It consists of a linear Paul trap with segmented electrodes, which is filled with helium buffer-gas. Ions are stored in the RFQ in a superposition of a time-independent and an oscillating electric field. While the RFQ is continuously loaded with ions they accumulate after a cooling time of a few milliseconds in the potential minimum in the RFQ due to interactions with the buffer gas [42]. Nuclides with low production rates can be collected before they are transferred to the experiment. In case of the Penning trap experiment a bunched beam is anyhow preferred, and for the collinear laser spectroscopy the benefit is that the particle density increases compared to the continuous beam. In addition background events can be suppressed adjusting the detection interval to the ejection trigger of the RFQ. Furthermore, the emittance of the beam decreases due to the cooling, which improves the transport efficiency through the setup. This is especially important for loading the ions into the Penning traps as they need to be decelerated from 30 or 60 keV to a few 10 eV in order to be able to trap them. During the deceleration the emittance increases by a factor $\sqrt{E_{\mathrm{kin},1}/E_{\mathrm{kin},2}}$ and therefore buffer gas cooling is applied in the RFQ to make the ion transport to the traps more efficient.
TRIGA-SPEC serves also as a test facility for the experiments MATS and LaSpec at the future facility FAIR [43]. On a shorter timescale TRIGA-TRAP is used in addition as a test facility for SHIPTRAP [44], which is installed behind the velocity filter SHIP [8] at GSI Darmstadt. At SHIPTRAP mass measurements of heavy and super heavy elements are performed and will therefore benefit from developments at TRIGA-TRAP such as the non-destructive single-ion FT-ICR detection, which can be tested with heavy elements like uranium, americium or californium before the final installation at SHIPTRAP. At the TRIGA-LASER setup new techniques for a precision increase of collinear laser spectroscopy will be tested by an accurate determination of acceleration voltages up to 60 kV. In addition absolute frequency measurements of transitions are planned by locking the system to a fiber-laser based frequency comb. These techniques are important for investigations on light isotopes and are additionally of interest for the COLLAPS/ISOLDE experiment at CERN [45].

2.4.1 The laser spectroscopy setup TRIGA-LASER

The collinear laser spectroscopy (CLS) method to be applied at TRIGA-LASER is well known for optical spectroscopy studies. In general a continuous-wave (cw) laser is overlapped with a fast singly-charged ion or neutral atom (after charge exchange) beam at energies of $30 - 60\,\mathrm{kV}$ in collinear or anti-collinear geometry. This allows to study nuclear ground state properties like charge radii, moments and spins of short-lived radionuclides by isotope shift and hyperfine structure measurements [5]. The high kinetic energy reduces the velocity spread of the beam. Considering Fig. 2.9 the decrease of the velocity spread is obvious. At higher beam energies the energy spread remains the same while the velocity spread decreases. As fine tuning of the laser frequency is often difficult it is possible in this case to use a fixed-frequency laser and tune the accelerating voltage to change the Doppler-shift, so that a transition of the ions is resonant to the laser wavelength.
Model independent high precision data about nuclear ground and isomeric states are required for accurate nuclear structure studies. Measurements that are performed in combination with an online coupling to an isotope production facility like TRIGA Mainz allow even investigations on short-lived rarely produced radionuclides. The properties that can be studied are the nuclear spin I, the magnetic moment μ_I, the spectroscopic quadrupolar moment Q_S, and the difference of mean-square nuclear charge radii between isotopes $\delta\langle r^2\rangle$. These parameters are measured directly and therefore the collected data is completely model independent.
A detailed description about the extraction of nuclear data from optical spectra is given in [46] and will be summarized here. Between two isotopes the transition frequency of an electronic transition is shifted. Two components contribute to the shift of the transition frequency: the so-called mass shift (MS) and the field shift (FS). The mass shift is caused by the difference in nuclear mass and thus different center-of-mass motions:

$$\delta\nu_{\mathrm{MS}}^{MM'} = (K_{NMS} + K_{SMS})\frac{M' - M}{M'\,M} \ . \tag{2.16}$$

K_{NMS} denotes the constant for the normal mass shift, which is due to the interaction of nucleus and electrons, and K_{SMS} denotes the constant of the specific mass shift, which is due to the interactions of the electrons among each other. The shift in the charge distribution $\delta\langle r^2\rangle$ causes the field shift between two isotopes with the masses M and M'

$$\delta\nu_{\mathrm{FS}}^{MM'} = \frac{2\pi\,Z}{3}\Delta|\Psi(0)|^2\,\delta\langle r^2\rangle \tag{2.17}$$

and effects the transition frequency as well as the mass shift. $\Delta|\Psi(0)|^2$ is the change of the electron density at the nucleus in the transition. For the hyperfine structure information the Casimir formula connects the electronic spins J and the nuclear spin I, the magnetic dipole moment μ_i and the spectroscopic quadrupole moment Q_S with the hyperfine correction of the transition frequency

$$\Delta\nu_{\mathrm{HFS}} = \frac{A}{2}C + \frac{B}{4}\frac{\frac{3}{2}C(C+1) - 2I(I+1)\,J(J+1)}{(2I-1)(2J-1)\,I\,J} \ . \tag{2.18}$$

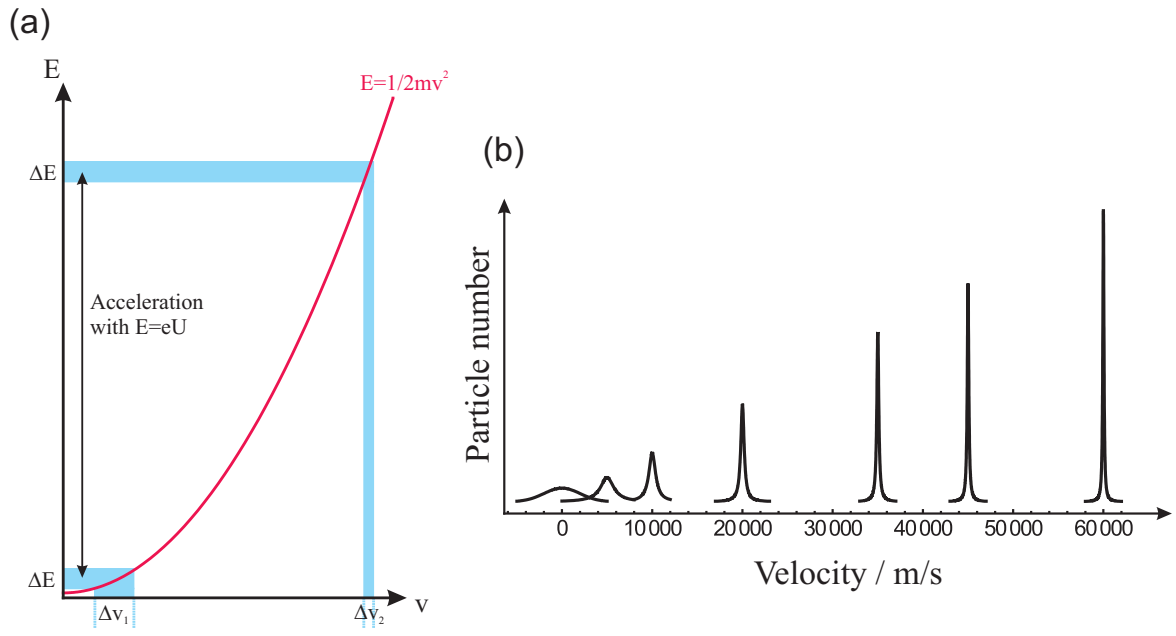

Figure 2.9: Principle of decreasing the velocity spread. When particles are accelerated in one specific direction their velocity spread decreases while the energy spread remains the same (a). During acceleration the number of particles and therefore the area under the Lorentzian function that describes the velocity spread are constant. Thus the amplitude of the peak increases when the velocity spread is decreased (b).

Here $C = F(F+1) - I(I+1) - J(J+1)$, $A = \frac{\mu_I B_e(0)}{I\,J}$ is the magnetic dipole coupling constant and $B = eQ_sV_{zz}$ is the electric quadrupolar coupling constant with the magnetic field created by the electron motion $B_e(0)$ and the electric field gradient V_{zz} at the nuclear site. The present sensitivity limit for CLS [47, 48] is in the order of 100 ions/s and a minimum half-life of $T_{1/2} = 8.8\,\text{ms}$, which has been obtained with ^{11}Li [49, 50].
At TRIGA-LASER, which is shown in Fig. 2.10, a 10° deflector overlaps the ion beam either coming from an offline surface ion source or from the ECR ion source with the laser beam. To bring the ions in resonance with the laser beam the velocity of the ions is tuned by changing their kinetic energy. As most ions and atoms do not have a closed two-level transition outside the ground state, a decay into a state without interaction with the laser light will follow excitation. This would result in a very weak signal, thus interactions of light and particles have to be avoided until the detection region is reached. Therefore the particle velocity can be fine-tuned by applying a potential to a metal tube in the detection region for ions or to the charge exchange cell (CEC) for neutral atoms, which is needed if transitions in the ionic spectrum are disadvantageous for cw lasers to neutralize them and perform spectroscopy on neutral atoms. At present only optical ion detection is planned in a section that is designed to reflect the fluorescence light via a lens to an adjacent pair of photomultipliers. Operation is possible in a wide spectrum from 200 nm to 750 nm with a quantum efficiency up to 20 %.

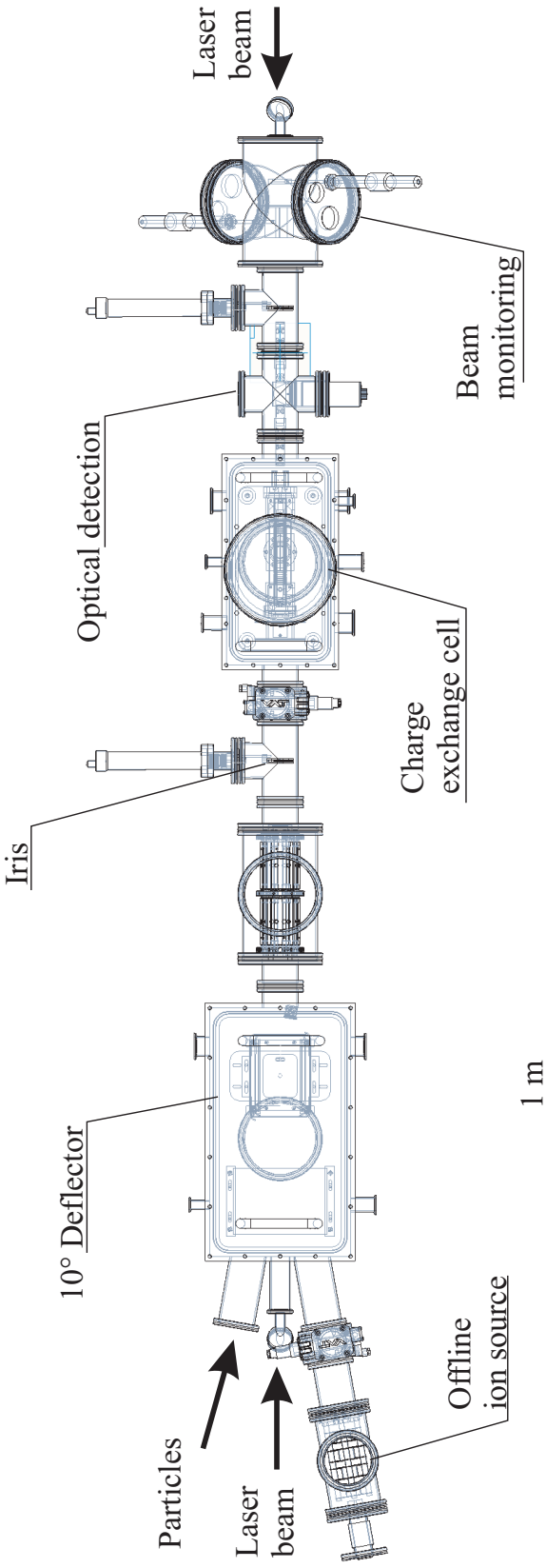

Figure 2.10: Sketch of the TRIGA-LASER setup. The ions are either produced in the offline ion source or enter the laser beamline on the left coming from the online coupling to the reactor. The 10° deflector overlaps particle and laser beam. The ions are neutralized in the charge exchange cell and detected in the optical detection region. A more detailed explanation is given in the text.

At the first stage of TRIGA-LASER limits for the fluorescence detection of $10^5 - 10^6$ ions/s are expected but even this limited sensitivity should provide the opportunity to investigate some fission products of ^{249}Cf, e.g. rhodium isotopes of which neither isotope shifts nor hyperfine structures have ever been measured. For measurements far away from stability cooling and bunching of the ion beam is a method to increase the signal-to-noise ratio and thus the sensitivity limit to about 100 ions/s [47, 51].

2.4.2 The mass spectrometry setup TRIGA-TRAP

Mass measurements with Penning traps is a well-established procedure. Unrivaled precision can be reached on stable as well as on short-lived nuclides [3]. A detailed description of a Penning trap, which is shown in Fig. 2.11(a), is given in [52] and only a brief summary is provided here.
The trap electrodes are placed in a strong homogeneous magnetic field with the end caps pointing in B-field direction defining the z-axis, and a weak quadrupolar electric field is generated by applying a voltage to the trap electrodes. The motion of ions with charge-to-mass ratio q/m in an ideal trap can be separated in three independent eigenmotions as shown in Fig. 2.11(b), which are characterized by their frequencies

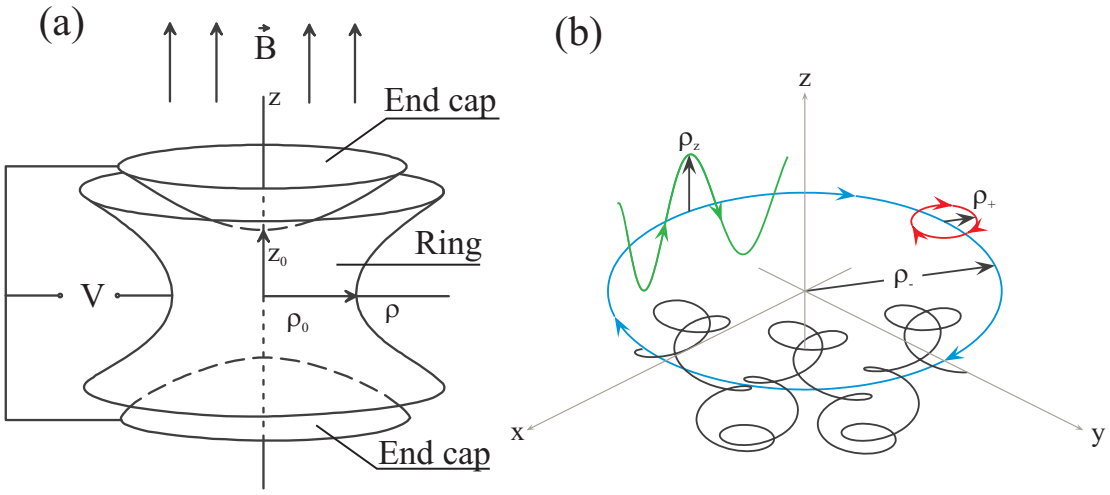

Figure 2.11: Sketch of a hyperbolic Penning trap (a) and the ion motion in the trap (b). The trap electrodes are placed inside a homogeneous magnetic field and a quadrupolar field is created by applying a proper voltage to them. The ion motion can be separated into three eigenmotions, reduced cyclotron motion with radius ρ_+, magnetron motion ρ_- and axial motion ρ_z.

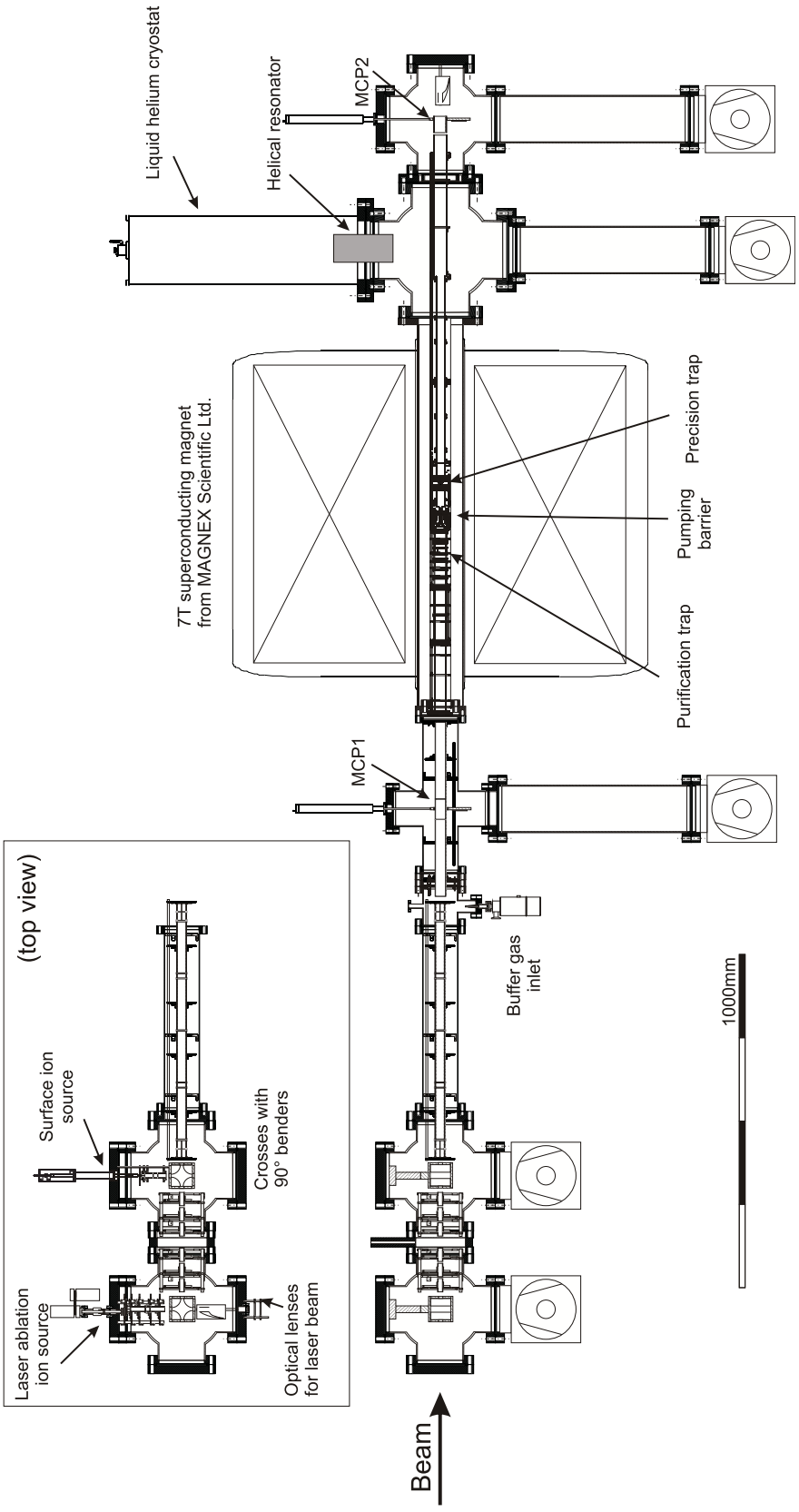

Figure 2.12: Overview of the TRIGA-TRAP setup. The 7-T magnet contains the two Penning traps, which are separated by the pumping barrier. The ions are either produced in one of the offline ion sources or enter the trap beamline on the left coming from the online coupling to the reactor. The 4-K cryostat hosts the amplifiers for the single ion detection with the narrowband FT-ICR method. In the cryogenic setup the vacuum is typically in the order of 10^{-9} mbar.

$$\nu_+ = \frac{1}{2}\left(\nu_c + \sqrt{\nu_c^2 - 2\nu_z^2}\right) \tag{2.19}$$

$$\nu_- = \frac{1}{2}\left(\nu_c - \sqrt{\nu_c^2 - 2\nu_z^2}\right) \tag{2.20}$$

$$\nu_z = \frac{1}{2\pi}\sqrt{\frac{qV}{mD^2}} \ , \tag{2.21}$$

the reduced cyclotron frequency ν_+, the magnetron frequency ν_- and the axial frequency ν_z. Here B denotes the strength of the magnetic field and V the electric potential inside a trap with the characteristic parameter

$$D = \sqrt{\frac{1}{2}\left(z_0^2 + \frac{\rho_0^2}{2}\right)} \tag{2.22}$$

defined by the minimum distance of the end caps $2z_0$ and the minimum radius of the ring electrode ρ_0. The eigenfrequencies in the trap are connected to the free cyclotron frequency

$$\nu_c = \frac{1}{2\pi}\frac{q}{m}B \tag{2.23}$$

via the invariance theorem

$$\nu_c^2 = \nu_+^2 + \nu_-^2 + \nu_z^2 \ , \tag{2.24}$$

which can be simplified to $\nu_c = \nu_+ + \nu_-$ for an ideal Penning trap [52]. Assuming singly charged ions, the atomic mass m_{atom} of the ion of interest can be calculated from the cyclotron frequency of the reference ion $\nu_{c,\mathrm{ref}}$, used for the calibration of the magnetic field strength, the cyclotron frequency of the ion of interest ν_c, the atomic mass of the reference ion m_{ref} and the electron mass m_e:

$$m_{\mathrm{atom}} = \frac{\nu_{c,\mathrm{ref}}}{\nu_c}(m_{\mathrm{ref}} - m_e) + m_e \ . \tag{2.25}$$

Adequate references are carbon cluster ions as they are integer multiples of the atomic mass unit[2]. At TRIGA-TRAP a laser ablation ion source was built, which produces carbon clusters up to C_{27}^+ and which allows to perform absolute mass measurements [39].
Under experimental conditions the radioactive ion beam is guided through the switchyard in straight direction to the TRIGA-TRAP experiment. A detailed drawing of the TRIGA-TRAP setup is presented in Fig. 2.12. The online produced ions enter the beamline on axis, the two offline ion sources have each a 90° electrostatic deflector to bend the beam into the beamline. MCP1 is a movable detector to optimize the beam before injection into the strong magnetic field. The optimized ion beam is guided to the first trap, which is a cylindrical trap used for preparation and purification processes. After ion preparation the ions of interest pass the pumping barrier and can be stored in the second trap, which

[2]Electron and cluster binding energies are neglected here.

is a hyperbolic trap, where the actual mass measurement is performed, either by a non-destructive detection technique or by the TOF-ICR technique, which involves measuring the flight time to a detector at the end of the beamline. Presently measurements are performed at room temperature and at a pressure of 10^{-8} mbar, which is generated by a set of turbo pumps. By cooling the trap tube down to 77 K a pressure of 10^{-9} mbar can be reached. The detection electronics can be cooled down to 4.2 K in the liquid helium cryostat for low noise measurements with superconducting circuits. Investigations on the magnetic field inside the magnet showed a very homogeneous field for the Penning traps with a homogeneity of $\Delta B/B \approx 0.14\,\mathrm{ppm/cm^3}$ in the inner volume [53]. Inside the homogeneous magnetic field two Penning traps are in use for mass measurements. In the cylindrical purification trap the mass-selective buffer-gas cooling technique [54] is applied. The ion motions are cooled by collisions with helium buffer gas at a pressure of about 10^{-4} mbar. First, a dipolar excitation is applied to increase the magnetron radius of all particles mass independently. With the subsequent application of a quadrupolar excitation at ν_c ions of one selected mass are centered due to the conversion of magnetron to modified cyclotron motion, which is cooled much faster than the magnetron motion. Thus the ions of interest are centered in the trap while all other species remain on their initial magnetron radius. Therefore a mass-selective extraction is possible as only centered ions can pass the pumping barrier between the purification and the precision trap. With this procedure a mass resolving power of $\Delta m/m = 10^5$ has been demonstrated at TRIGA-TRAP. The pumping barrier is also necessary for lowering the gas pressure in the precision trap by limiting the helium flow, which is necessary as a high gas pressure is needed for ion cooling in the first trap and a low pressure for high-precision measurements in the second trap [55]. As a non-destructive detection method of the ions in the purification trap, a broadband Fourier transform-ion cyclotron resonance (FT-ICR) detection system is being developed [53, 56]. This offers the advantage to analyze all ion species inside the trap without losing the trapped ions. A detection limit of a few ten ions is envisaged.
The FT-ICR detection method is based on the detection of the image current in the ring electrode segments induced by oscillating ions. Hence, the measurement is only limited by the storage time and the lifetime of the ion of interest. In addition the number of required ions to gain sufficient statistics is very low since the ions are not lost during detection. By the assumption of an oscillating ion inside a parallel-plate capacitor with infinite size, the image current can be calculated as [57]:

$$i(t) = \frac{2\pi q \nu_{\mathrm{ion}} r_{\mathrm{ion}}(t)}{d} \tag{2.26}$$

where ν_{ion} is any of the eigenfrequencies and d the modified distance between two opposite electrodes [58]. The FT-ICR detection principle is presented in Fig. 2.13. The induced current is converted into a voltage drop by external circuits, which is amplified and subsequently converted from time into frequency space. Thus, the Fourier transformation of the detected signal yields the frequency ν_{ion}. For the mentioned broadband FT-ICR detection it is sufficient to use conventional amplifiers as the current induced by the large number of trapped ions is sufficiently high. In order to define a radius and a coherent motion the

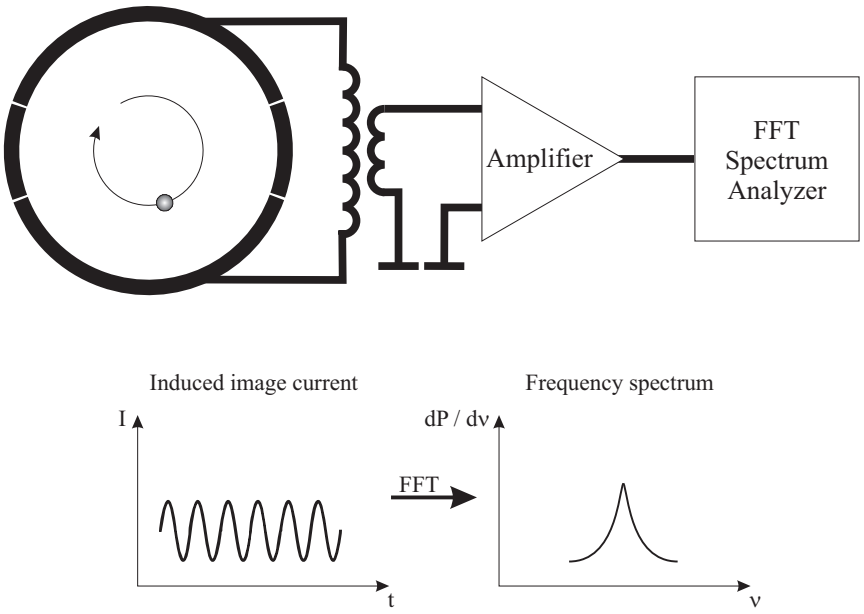

Figure 2.13: Detection scheme of the non-destructive FT-ICR detection. The ion motion in the trap induces an image current in the electrodes, which is converted into a voltage drop, amplified and Fourier transformed into frequency space. The narrowband FT-ICR for single ion detection requires a cryogenic amplifier.

ions are excited by a dipolar excitation at the eigenfrequency to be observed. In the precision trap the narrowband FT-ICR technique is implemented for the high precision mass measurement of singly charged ions. Since it is aimed for single ion detection the image current is typically in the range of 10 to 100 fA depending on the motional amplitudes. Hence, compared to the broadband FT-ICR a different detection is required. Due to the low signal of a single ion a superconducting transformer and a helical resonator is used to increase the signal-to-noise ratio [53]. In addition the circuit has to be resonant to the ion motion to amplify the signal sufficiently. In the TRIGA-TRAP experiment only the reduced cyclotron frequency ν_+ is determined to obtain the mass value of the stored ion. The precision trap is a hyperbolic trap followed by a system of drift tubes and therefore the key part of the time-of-flight ion cyclotron resonance (TOF-ICR) and FT-ICR measurement as well. For the frequency determination of short-lived nuclides in a Penning-trap the TOF-ICR method is the ideal choice [59]. In Fig. 2.14(a) a sketch of the measurement principle with the ion flying from the trap to the detector is shown. Fig. 2.14(b) shows the theoretical curve of the time of flight as function of $(\omega_q - \omega_c)T_q$ with the excitation frequency ω_q, the excitation time T_q, and the cyclotron frequency ω_c [59]. Here the frequencies are given as angular frequencies. For an excitation frequency $\omega_q = \omega_c$ the time of flight is minimal. For the TOF-ICR measurement an electric quadrupolar field with the frequency $\nu_+ + \nu_-$ is used to couple the radial eigenmotions. The radial energy, which determines a magnetic moment, is mainly determined by ν_+. A force depending on the energy and the magnetic field gradient effects the ions: $\vec{F} = -\frac{E_{\mathrm{rad}}}{B}\frac{\partial B}{\partial z}\vec{e_z}$. Thus, if they

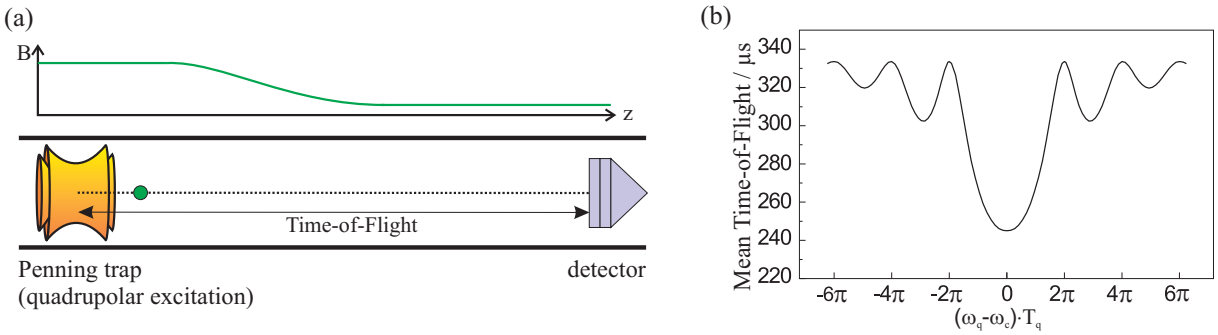

Figure 2.14: Sketch of the time-of-flight measurement principle (a). Ions are excited in the trap with different frequencies and fly to the detector where their time-of-flight is measured. The time of flight as function of $(\omega_q - \omega_c)T_q$ (b) with the excitation frequency ω_q, the excitation time T_q, and the cyclotron frequency ω_c is minimal for an excitation with the frequency $\omega_q = \omega_c$ [59].

are ejected from the trap with different energies, their time of flight deviates for different excitation frequencies around a minimum for ν_c. A higher precision can be gained by the so-called Ramsey excitation technique, where instead of a continuous excitation the excitation signal is separated by waiting times, leading to multiple fringes, and a decreased line width of the TOF resonance as shown in Fig. 2.15 [60, 61].
A limitation for high-precision mass measurements is the time variation of the magnetic field, especially for longer measurements of several hours. For the correction of the nearly linear drift of the magnet a cyclotron frequency measurement of a reference ion is carried out before and after the actual measurement of the ion of interest [62, 63]. Also misalignments of the position of the trap electrodes in the magnetic field, the inhomogeneity of the field and imperfections of the electrodes, like their segmentation, limit the precision [3]. For measurements of exotic short-lived nuclides limiting factors for TOF-ICR technique are the relatively slow buffer gas cooling in the purification trap and the excitation in the precision trap, which can last from milliseconds up to several seconds depending on the desired resolving power. The shortest-lived nuclide that has ever been investigated in a Penning trap is ^{11}Li with a half-life of 8.8 ms [64]. In the FT-ICR mode the observation time is the limiting factor. It has to be 1 to 10 s for a sufficient long detection of the image current in the precision trap [65, 66]. Summing up, the TOF method allows the detection of short-lived radionuclides down to half-lives of a few milliseconds depending on the production rate, whereas the FT-ICR method can only be used for nuclides with half-lives down to 1 s. The strength of the latter method is that it can work in principle with one single ion. Thus it can be applied also when production rates are very low, even down to one per minute and less. TRIGA-TRAP aims for single ion detection with FT-ICR to investigate particles with very low production rates but sufficiently long half-lives. The implementation of TOF-ICR and FT-ICR detection techniques in the same Penning trap mass spectrometer is unique and offers the chance to measure the cyclotron frequency in two different ways for the comparison of both methods and to benefit from the advantage

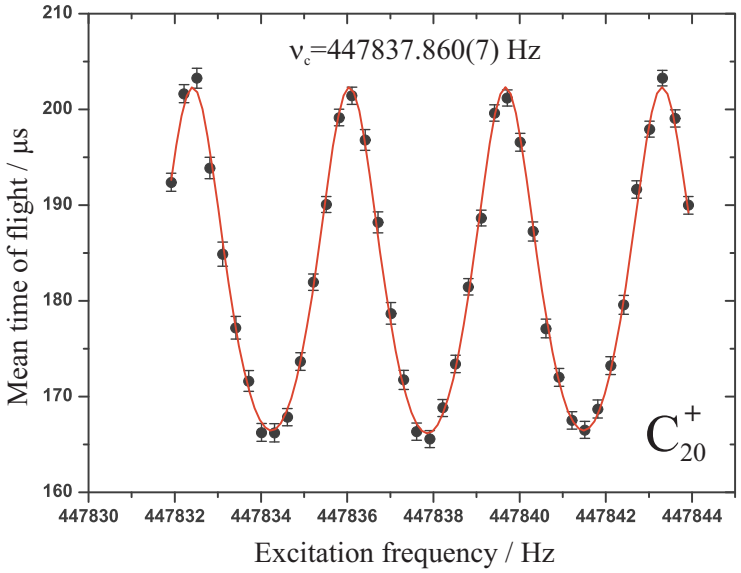

Figure 2.15: Time-of-flight resonance of C_{20}^+ using the Ramsey excitation technique of time separated oscillatory fields at TRIGA-TRAP. The red line is a fit of the theoretical line shape to the measured values [60, 61].

of both techniques.
First offline mass measurements at TRIGA-TRAP have already been performed on ^{241}Am. Together with the results of $^{252-254}$No from SHIPTRAP these are the very first direct mass measurements of transuranium nuclides. Since all nuclides heavier than uranium are linked by alpha-decay chains to the known masses, direct mass measurements on these nuclides can confirm the result of the decay spectroscopy experiments and provide new anchor points in the region of transuranium elements for the super heavy isotopes.

Chapter 3

Aerosol classification

TRIGA-SPEC aims for the investigation of neutron-rich nuclides. Therefore fission products have to be extracted from the reactor TRIGA Mainz and guided to the setup [4]. As the transport capillary has an approximate length of 7 m, it is not possible to transfer them in pure gas and hence, aerosols are used as means of transport. Aerosols are small solid or fluid airborne particles inside a carrier gas in which they usually are produced under different experimental conditions. Usually they consist of single atoms that form conglomerates in a chaotic way. In the case of TRIGA-SPEC it is sufficient to use solid aerosols for the transport as they have already been tested [36] and the aerosol generators are available. Aerosols have been used in the Institut für Kernchemie at the HELIOS experiment for the extraction of fission products from the reactor [67]. As carbon aerosols shall be used at TRIGA-SPEC, which is the first use of this kind of aerosols at the TRIGA reactor, investigations on the size distribution of the aerosols as well as the influence of external parameters on the production are necessary. Especially the time dependent behavior of the aerosol production over long periods is important as investigations on radionuclides with low production rates can take several hours, in which a stable fission fragment transport is required.

3.1 Principles of aerosol production and detection

The production of e.g. KCl aerosols can be realized by heating up the salt inside a tube furnace within a gas flow for aerosol transport and better temperature control. At temperatures of about 600°C (melting point 770°C) KCl starts to sublimate from the salt surface into the gas and aerosols are produced [67]. For the use of fluid aerosols the gas has just to be guided through a fluid. This causes turbulences in which liquid aerosols are generated and flushed out with the gas. By adding solid particles of one single size to water and drying the gas after the generation process, which means removing the fluid aerosols by guiding the gas through silica gel, it is even possible to produce monodisperse aerosols in a gas. This thesis deals with the production and investigation of carbon aerosols. Although this is a known technique it was applied for the first time at the reactor TRIGA Mainz.

3.1.1 The carbon aerosol generator

For the carbon aerosol production an aerosol generator that has been built at the Paul Scherrer-Institut is in use. It's principle is shown in Fig 3.1. The capacitor C, which is connected to two pure graphite electrodes having a distance of about one millimeter, is charged by a constant current source. When the breakdown voltage of about 1.5 kV is reached a discharge takes place between the electrodes and carbon is evaporated into the helium gas flow. Immediately after the discharge the vapor cools down and condenses to particles of a few nanometers size due to the present supersaturation. Due to Brownian motion and absorption of smaller particles they grow to aerosols with diameters between 10 nm and 1 μm [68] and can be guided to the experiment.
It is possible to decrease the breakdown voltage and thus to increase the discharge frequency by adding a small amount of nitrogen to the gas as the binding energy of the electrons are lower for nitrogen than for noble gases. Depending on the experiment other noble gases like argon and krypton or even methane and butane can be used as carrier gas.

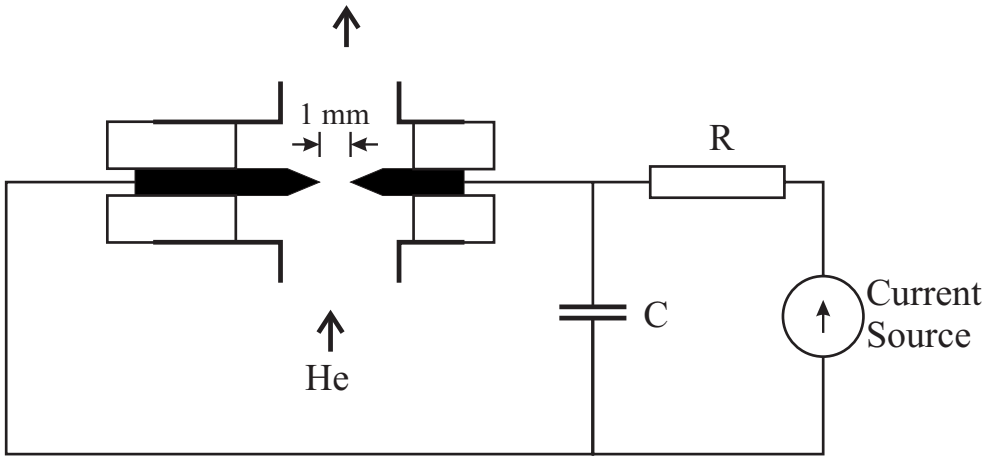

Figure 3.1: Sketch of the carbon aerosol generator. The capacitor C, which is connected to the pure graphite electrodes, is charged by a constant current source. When the breakdown voltage is reached a discharge takes place and graphite is evaporated.

3.1.2 Determination of the aerosol size

To determine the size of an aerosol particle a commercial Scanning Mobility Particle Sizer (SMPS) is used. It is in fact a combination of two devices: The Electrostatic Classifier (EC) and the Condensation Particle Counter (CPC). A detailed sketch of the setup for an aerosol size measurement is presented in Fig. 3.2. Particles of different q/m can be separated by the EC. Before the particles reach the classifier, they are guided through the so-called impactor, a small nozzle, where the gas is accelerated in front of an impaction plate, to which the heaviest particles attach due to their inertia. Then the aerosols enter the EC and are guided through an ^{85}Kr source, which charges the smallest particles by

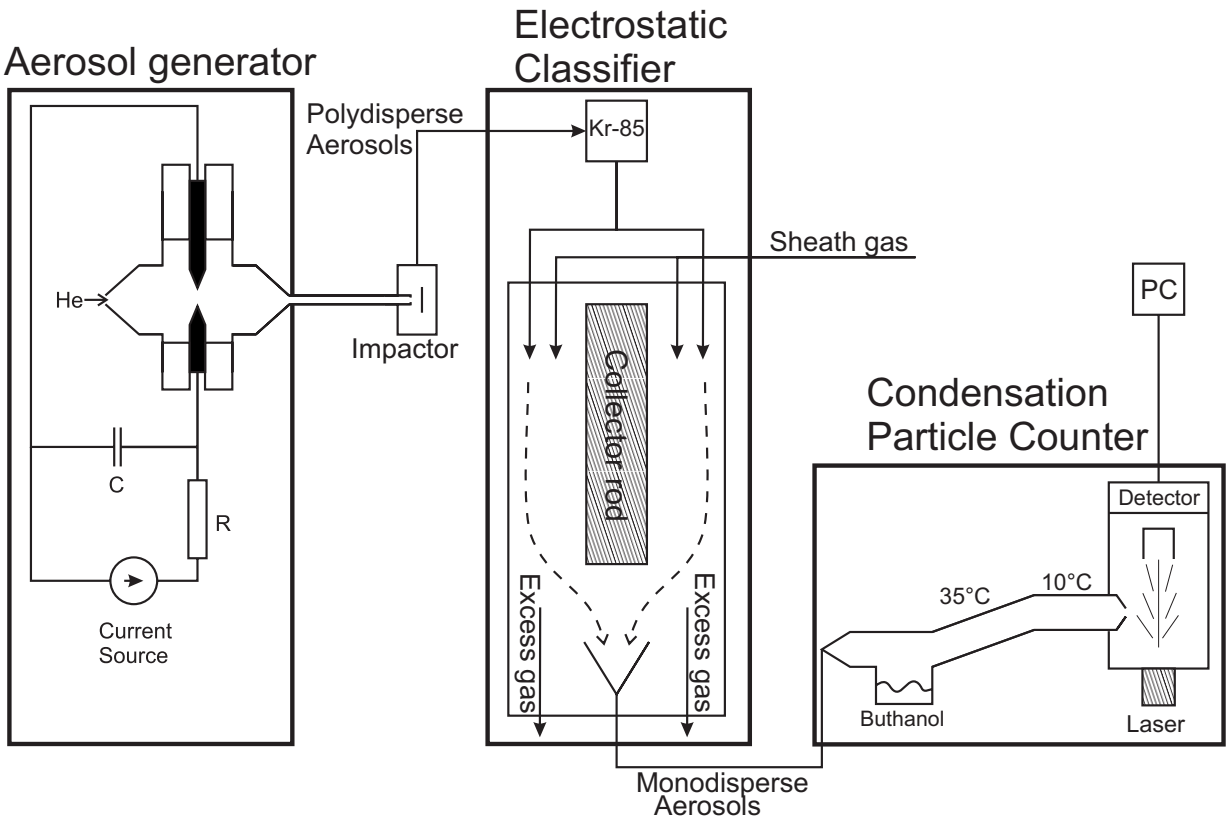

Figure 3.2: Sketch of a test setup to determine the aerosol size. The aerosols are produced inside the aerosol generator and guided to the Electrostatic Classifier, in which aerosols of one mass are selected. These selected particles are guided to the Condensation Particle Counter, where their number is determined. With the assumption that the aerosols are spheres their size distribution can be calculated. A detailed description is presented in the text.

β^-−radiation in a bipolar equilibrium [69, 70] and particles with a diameter of more than 10 nm according to the Boltzmann distribution, respectively. The observable particles with diameters from about 10 nm to at least 400 nm are mainly singly charged whereas larger particles have a higher probability to be multiple charged, which would falsify the classification. As particles with diameters larger than 800 nm are removed by the impactor it is assured that the measurement is done correctly.

A particle with the charge $q = n\,e$ in an electric field E will move through the field due to the electric force. As the motion is inside a gas atmosphere the Stokes' friction counteracts the electric force. Hence, both forces can be equalized and the electric mobility, a measure for the ability to move in an electric field, can be calculated as shown in [71, 72]. In the following, the result of the calculations is presented. The electrical mobility is

$$Z_p = \frac{n\,eC}{3\pi\eta\,D_p} \tag{3.1}$$

for spherical particles with diameter D_p, the viscosity η and the slip correction factor C, which is a function of D_p. However, instead of particles with a certain mass-to-charge ratio the EC selects only an electrical mobility class in dependency of the applied voltage U:

$$Z_p(U) = \frac{\ln \frac{r_2}{r_1}}{2\pi U L} \left(Q_t - \frac{1}{2} \left(Q_a + Q_m \right) \right) \tag{3.2}$$

with the radius of the inner electrode $r_1 = 9.37\,\text{mm}$, the diameter of the outer electrode $r_2 = 19.58\,\text{mm}$, the length of the collector rod $L = 444.4\,\text{mm}$, the polydisperse gas flow Q_a, the monodisperse gas flow Q_m and the total gas flow into the EC Q_t. The finite width of the slit for the monodisperse aerosols causes a mobility bandwidth to pass [72]:

$$\Delta Z_p(U) = \frac{\ln \frac{r_2}{r_1}}{2\pi U L} \left(Q_a + Q_m \right) \quad . \tag{3.3}$$

Thus, the EC separates the charged aerosol particles only by their electrical mobility, whereas the exact shape of the aerosols can not be determined. Therefore the aerosols are assumed to be spherical with diameter D_p and a constant density. Hence, the particle diameter has to be considered as a lower limit.
In order to analyze the aerosol size distribution the gas flow is guided to a tube with a collector rod in the center, to which a negative voltage is applied. The collector rod is surrounded by laminar flowing particle-free sheath gas, typically air or nitrogen, to assure that unwanted particles can not reach the monodisperse outlet due to turbulences and particles of the selected size will reach it. Thus, the gas containing the aerosols has to flow laminar as well. The charged aerosols are attracted by the collector rod and the aerosols of the requested q/m are guided to the small monodisperse outlet, whereas the others either attach to the rod or leave the EC via the exhaust outlet.
After the separation of aerosols of one class these particles are guided to the Condensation Particle Counter (CPC) for the determination of the particle density. They pass a region with a reservoir of butanol that is kept at 35°C to saturate the gas with butanol vapor and subsequently reach a condensation region where the butanol condenses to the aerosols due to a lower temperature of 10°C according to the Kelvin equation [73]

$$\frac{p}{p_s} = \exp \frac{4\sigma V_m}{kTD_p} \tag{3.4}$$

with the vapor pressure p, the saturation vapor pressure p_s, the surface tension of butanol σ, and the molar volume of the vapor V_m. The saturation $S = p/p_s$ determines the critical diameter, which is approximately 10 nm in the CPC. Smaller particles can not be registered as no condensation takes place whereas all particles of sufficient large diameters are increased up to several micrometers. These enlarged particles are counted in the detection region by light scattering. Thereby the light intensity is measured by a photo diode, whereas the calibration is given by TSI Inc.
By varying the voltage applied to the collector rod and measuring the correspondent number of particles the Scanning Mobility Particle Sizer (SMPS) calculates the numbers of particles per size interval and returns the size distribution of the aerosols.

3.2 Aerosol size distribution

Particle size distributions are important means to describe the properties of finely divided systems like aerosols. For the description of properties like electric charges, light scattering and their behavior in processes like diffusion and condensation a detailed knowledge of the size distribution is important [74, 75]. As already described in Sect. 3.1.1 the aerosols that are available for investigations grow by the absorption of small carbon particles in a vapor. The size distribution of the aerosols can be determined by measuring the number of aerosols in various mobility classes. Whereas measurements show very precise the log-normal shape of the distribution, an entire description of the growth process has not been achieved yet. In the following the theoretical model of the growth process is discussed and the experimentally determined size distribution of the carbon aerosols at TRIGA-SPEC presented.

3.2.1 Theory of lognormal growth processes

Theoretical investigations on the particle size distribution are performed since the beginning of the 20$^{\text{th}}$ century with the achievement of general theories [76, 77]. For the carbon aerosols, which evolve from a vapor, the initial growing is due to vapor absorption and continued by coagulation, whereas the coagulation process is not verified theoretically. Very detailed studies on the growing process have been performed with metal aerosols, which were therefore evaporated and cooled in helium. It was shown that after the gas evaporation the diameter x of the aerosols was lognormally distributed [78]

$$f(x) = \frac{1}{\sqrt{2\pi}\sigma x} e^{-\frac{(\ln(x)-x_a)^2}{2\sigma^2}} \quad . \tag{3.5}$$

With x_a being the mean diameter and σ the standard deviation. Due to these investigations it has been criticized the first time that models, which are based only on Brownian motion, could never explain the fundamental reason for lognormal size distributions as they are based on the theory of Smoluchowski [76] and thus assume the lognormal size distribution [79]. Another problem is that Smoluchowskis investigations consider a closed system of particles, which is not the case for most experimental setups including the aerosol generator at TRIGA-SPEC, as always particles are added and removed. A more recent model is proposed by Söderlund *et al.* [80], which shows how the lognormal distribution can be motivated without coagulation. It is introduced in the following.
The size distribution model by Söderlund *et al.* describes the growth of ultrafine particles in a growth zone. In this one-dimensional model the particles are only transported by diffusion and drift to the growth zone, which has a distance L to the production place. Diffusion is the normal random motion of a particle, whereas the drift is due to convection and flow around the point of origin of the ultrafine particles caused by the flowing gas. In the case of the previously described carbon aerosol generator convection is the major drift process due to the abrupt cooling of the vapor after the discharge. The assumption of a linear relation between growth time and size is legitimated by considering a spherical

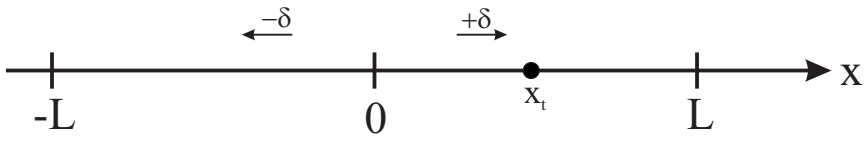

Figure 3.3: Description of the model introduced in Eq. (3.7). The particle starts at $x = 0$ moves by means of diffusion and drift $\pm\delta$ and is absorbed at $x = \pm L$. The time steps needed to reach the absorption barrier are counted and shown in Fig. 3.4.

particle with surface A located in atomic vapor absorbing atoms with a constant rate γ per surface area and time. Thus, the volume V increases with

$$\frac{\mathrm{d}V}{\mathrm{d}t} = \gamma A \ , \tag{3.6}$$

with $V \propto d^3$, $A \propto d^2$ and therefore $d \propto t$. d denotes the particle diameter. Now it becomes clear that the size distribution is lognormal if the time distribution is also lognormal. Hence, the time an atom needs to be absorbed by the particle and thus the first passage time of a random walk in one dimension has to be investigated next [81].
It is considered that a particle starts at the reflecting boundary $x = 0$ and the time it needs to be absorbed at $x = L$ can be measured. As the reflecting boundary can be simulated by a second absorbing one at $x = -L$ the time of a particle propagating to $x = \pm L$ is determined. Therefore a random walk has been implemented:

$$x_{t+1} = x_t + \varepsilon_t + \delta s \ . \tag{3.7}$$

Here δ is the drift speed, $s = \mathrm{sign}(x)$ its direction and ε the diffusion term, which is uniformly distributed on the interval [-1,1]. This means that the position of the wandering atom after $t + 1$ time steps is deviated from the position after t steps by a diffusion term and a directed drift term, see Fig. 3.3. The motivation for the drift direction is obvious as the first approach for the model contained the reflecting barrier, which has been simplified with a second absorbing barrier.
As diffusion and drift are opposed processes some estimations can be made. The diffusion equation $\langle x^2 \rangle = Dt$, with the mean-square displacement $\langle x^2 \rangle$ and the diffusion constant D, results in the fact that particles travel the distance L in the mean passage time $\langle t \rangle$ expressed by $L^2 = D \langle t \rangle$, which can be extracted from diffusion theory. The drift motion is considered to be a linear uniform motion with the drift velocity δ. In case the velocity of drift motion and diffusion are in the same range the corresponding drift is called critical drift with the critical drift velocity δ_0:

$$\delta_0 := \frac{D}{L} = \frac{1}{3L} \ , \tag{3.8}$$

with the diffusion constant assumed to be $D = 1/3$ in this model. Simulations have been done by Söderlund *et al.* [80] and have been reproduced within this thesis. For

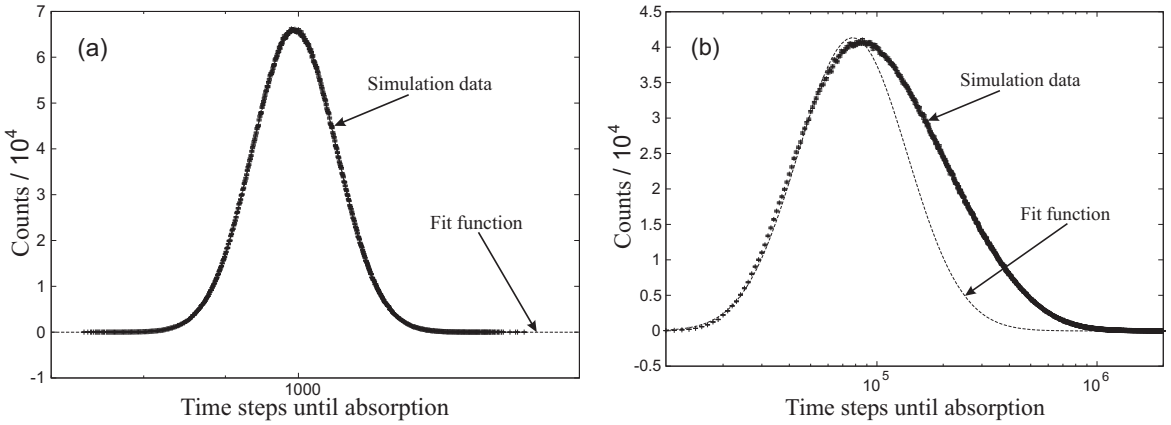

Figure 3.4: Distribution of the particle number a function of the absorption time of an atom by a huge particle. The distribution has been recorded with a drift speed to critical drift speed ratio of (a) $\delta/\delta_0 = 270$ and (b) $\delta/\delta_0 = 0.27$. A high drift speed causes a perfect lognormal distribution whereas a dominating diffusion deforms the lognormal distribution.

a representative simulation of the random walk a very uniformly pseudorandom number generator is necessary. Thus, the faster Mersenne Twister has been used [82] instead of the previously used RANLUX [83]. The result is presented in Fig. 3.4. According to [80] units have been neglected. Each simulation has been performed with 10^7 particles and the same distance $L = 300$ to the growth zone. The drift has been varied according to [80] and two representative results are presented. Fig. 3.4(a) has been performed with a drift to critical drift ratio of $\delta/\delta_0 = 270$ and fits perfectly to a lognormal distribution as demonstrated by $\chi^2 = 1.0$, whereas the simulation shown in Fig. 3.4(b) with a drift to critical drift ratio of $\delta/\delta_0 = 0.27$ clearly deviates from the lognormal distribution ($\chi^2 = 54.3$). In addition, mean and standard deviation of the distribution increase for lower δ/δ_0. This is an expected effect, especially the increase of the mean, as a decrease of the drift lowers the influence of the only directed motion. Hence, one can conclude that as the time distribution for absorption is lognormal for high drift velocities, the size distribution is lognormal as well.

3.2.2 Size distribution of the carbon aerosols

For the measurement of the size distribution the experimental setup shown in Fig. 3.2 was developed. A photography of the test setup is shown in Fig. 3.5. The voltage applied to the collector rod was varied to count the number of particles in all mobility classes. This has been done at a helium gas flow of 2.0 l/min and a loading current of the capacitor of $I_C = 1.25$ mA. The particle motion is a superposition of convection and uniform motion directed by the gas flow. As the gas flow accelerates all particles to the same velocity [38] this motion is not expected to effect the lognormal character of the size distribution. Thus, the lognormal size distribution is due to the convection caused by the fast cooling after the discharge, as discussed in the previous section. A first result of this kind of measurements is presented in Fig. 3.6. The plotted values are the numbers of aerosols N that arrived at

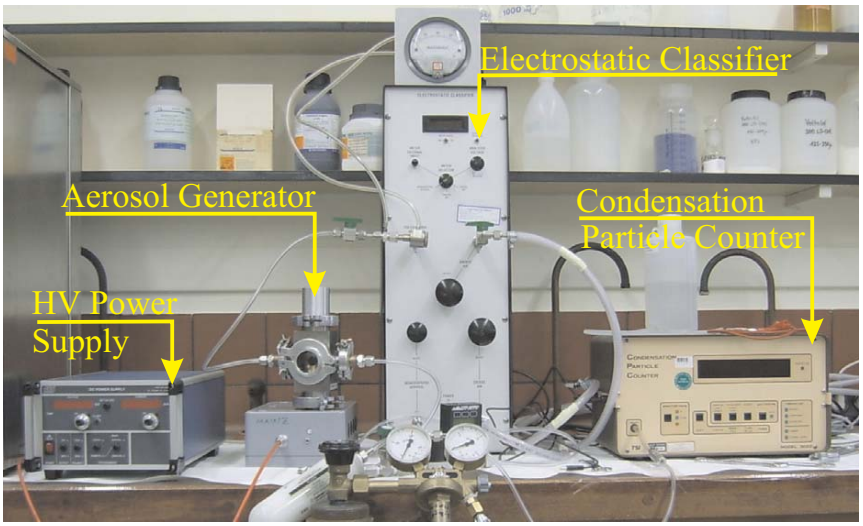

Figure 3.5: Photography of the experimental setup realized within this thesis for investigations of the aerosols.

the Condensation Particle Counter in dependency of the previously selected size. This is based on the already mentioned assumption that the aerosols are spheres.
A lognormal size distribution of the carbon aerosols was observed with the maximum at (112.9 ± 0.3) nm. The measurement of the whole size range that is available with

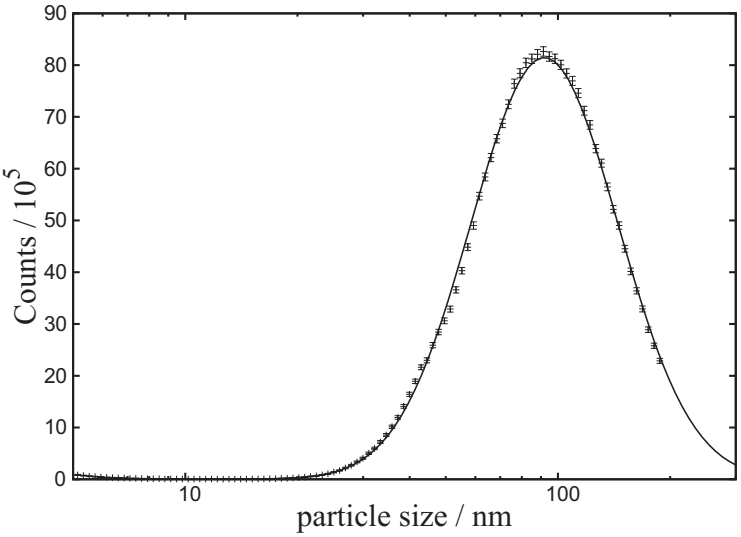

Figure 3.6: A typical measured size distribution of the carbon aerosols produced by the aerosol generator with a maximum intensity at (112.9 ± 0.3) nm. The helium gas flow was 2.0 l/min and the loading current of the capacitor was $I_C = 1.25$ mA. The statistical uncertainties are given by $\sqrt{N}$ as a Poisson distribution for the number of measured particles is assumed. The solid line is a fit of a lognormal function to the data points.

the Electrostatic Classifier lasts 120 s and consists of 120 data points. The average over several measurement cycles has been recorded. As the detected size distribution is perfectly lognormal a high drift to critical drift ratio δ/δ_0 is achieved in this experiment. This shows the perfect match of experiment and theory and indicates the drift caused by convection to be high enough to generate a lognormal size distribution.

3.3 Experimental results

Variation of operation parameters of the aerosol generator like gas flow and loading current might be needed for the extraction and investigation of different radionuclides from the TRIGA reactor. Thus, it is important to know, which parameters have to be varied to tune the properties of the emitted aerosols to maximize the transport efficiency. It is important to know the influence of the production parameters on the most important properties like the mean of the size distribution, the width of the size distribution and especially the variation of the aerosol number. It is also advantageous to know the real shape of the aerosols because this helps to understand and estimate errors made in the classification process. Thus, several investigations have been performed within this thesis to understand the function and properties of the carbon aerosol generator. Procedure and results of these tests are presented in the following section.

3.3.1 Test of the particle size calibration

In order to validate the particle size scale of the Electrostatic Classifier standard particles of a well-defined size were used. The functionality of the device is assured if the size of these particles can be reproduced, otherwise a recalibration is necessary.

For the injection in the gas two devices were used, first the gas is guided into a closed bottle, which contains a mixture of water and an emulsion of polystyrene standard particles with a diameter of (105±0.1) nm. While the gas is passing through the liquid water aerosols as well as standard particles are solved in the gas flow. Due to the size of the standard particles, they mainly do not form aerosols in combination with water but exist in the gas as single aerosols of a defined size. Gas and aerosols are guided out of the bottle through a small hole and into a gas dryer, which is an about 30 cm long tube filled with silica gel. Inside this tube a second perforated tube is located, which allows interactions between aerosols and silica gel. Due to the hygroscopy of silica gel the water is mainly removed from the gas and in the ideal case only monodisperse aerosols, the standard particles, are transported and registered afterwards in the Classifier.

First the background, as presented in Fig. 3.7(a), has been measured to ensure that it is sufficiently low and does not contain significant peaks. Afterwards is was necessary to determine the signal caused by pure water without the dryer to investigate possible contaminations. Therefore the distribution in Fig. 3.7(b) has been recorded and it has been observed that pure water induces a very high and in addition broad distribution with a particle size maximum at about 20 nm. But as the standard particles have a certified

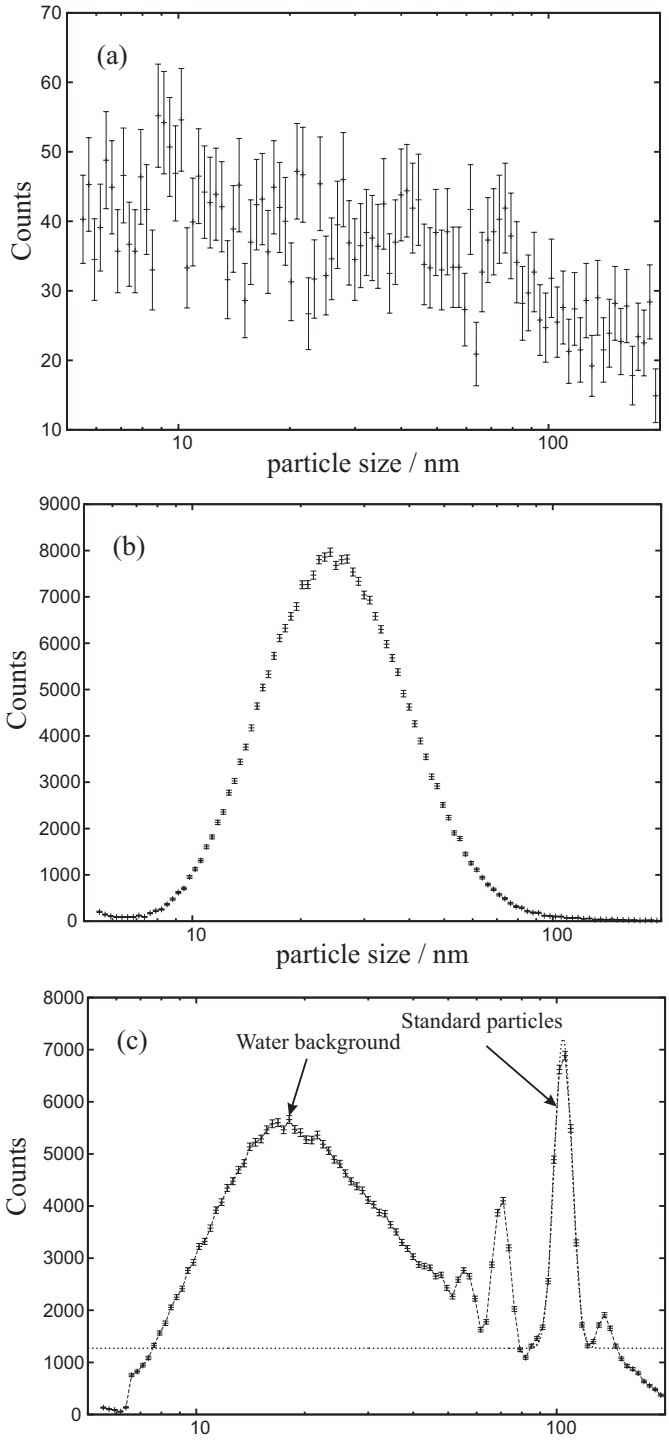

Figure 3.7: Background measurement of (a) gas and (b) pure water without previous drying. Afterwards the standard particles have been added (c). A significant peak appears at 105 nm, the size of the standard particles. For more details see text.

size of 105 nm, the size distributions of water and standard particles will not interfere with each other. Finally the standard particles were added to the water. Although no overlap has been expected the gas was guided through the dryer to the Classifier. In the result shown in Fig. 3.7(c) a significant peak with a maximum at a particle size of (104.2 ± 0.9) nm appeared, which is perfectly in agreement with the calibrated size of the standard particles. The two smaller peaks could not be identified, but it is assumed that they are caused by contaminations or multiple charged polystyrene particles as they only appeared after adding the particles to the water. But nevertheless it is verified due to the position of the largest peak that the calibration of the Classifier is correct. It has been observed as well that the maximum of the size distribution according to water shifted from Fig. 3.7(b) to (c). This is due to the gas dryer, which has been added after the measurement of the size distribution of water since the silica gel absorbs larger water particles with a higher efficiency in this size range.

3.3.2 Aerosol production in dependency on the loading current

The loading current of the capacitor C (see Fig. 3.1) can be changed at the power supply in a range from 0 to 2.5 mA. An increase of the current causes an increase of the discharge frequency, which is expected to result in an increase of the amount of generated aerosols as more carbon is evaporated.
The voltage at the capacitor that is loaded via a resistor R is given as

$$U(t) = I_0\, R\, \left(1 - e^{-t/(RC)}\right) \tag{3.9}$$

as the current source delivers a constant current I_0. Thus the time t_B it lasts to reach the breakdown voltage U_B is

$$t_B = \frac{-\ln\left[1 - \frac{U_B}{I_0\, R}\right]}{R\, C} \quad . \tag{3.10}$$

With a series expansion of the logarithm this can be approximated as

$$t_B = -\frac{1}{R\, C} \sum_{k=1}^{\infty} (-1)^k \frac{\left(-\frac{U_B}{I_0\, R}\right)^k}{k} \approx \frac{U_B}{I_0\, C\, R^2} \ , \tag{3.11}$$

which indicates that the discharge frequency is proportional to the loading current in first order approximation. As it is assumed that the same amount of carbon is vaporized in every discharge if neither gas pressure nor flow are varied, a linear dependency between the generated carbon aerosols and the loading current is expected. To characterize the behavior of the carbon aerosol generator the produced mass per time was chosen as measure, which is calculated from the measured size distribution of the aerosols with the approximation that the aerosols are massive spheres. The so produced amount describes the behavior better than the number of aerosols as deviations of the maximum size and therefore the whole

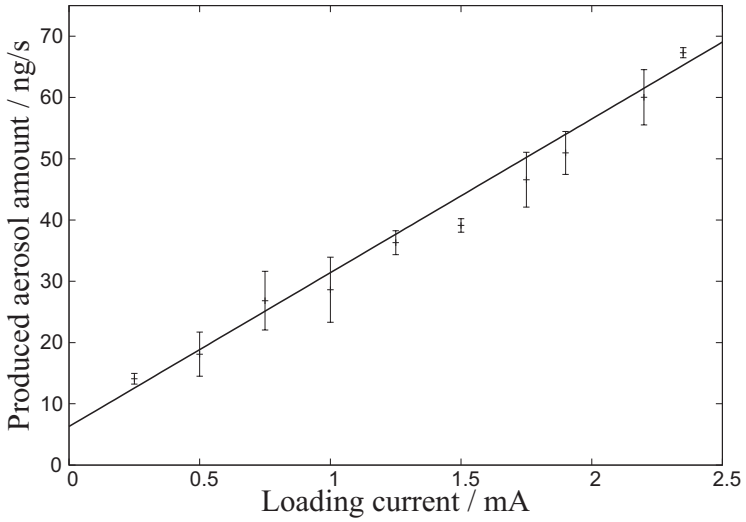

Figure 3.8: Aerosol amount produced per second as a function of the loading current of the capacitor C shown in Fig. 3.1. The amount was calculated from the measured size distribution with the assumption that the aerosols are spheres. The solid line is a linear fit to the data points with $\chi^2 = 3.85$.

size distribution can cause deviations of the number of aerosols but not their overall mass. It has been demonstrated with KCl aerosols that fluctuations in the generated number can appear without fluctuations in the overall mass [36] by collecting the aerosols on a filter and determine their overall mass with a chemical analysis. These kind of measurements are impossible for carbon because all filters with a sufficient pore size contain carbon and are thus inappropriate for these analytical methods.
As shown in Fig. 3.8 the result fits very well to the expectations, which is indicated by the fit. The presented values are the weighted mean of three measurements and the errors accordingly the weighted standard deviation of these values. Since the breakdown voltage fluctuates in every discharge because the shape of the electrodes changes continuously and the amount of evaporated carbon particles in their environment fluctuates as well, a fluctuation of the discharge frequency and the produced mass are observed. Due to these fluctuations the errors vary in a wide range as well. From the statistical uncertainty the magnitude of these fluctuations can be estimated to about 10 to 20 %. But in correlation with Eq. (3.11) the expected linear relationship between loading current and produced amount of aerosols has been proven. The uncertainties of loading current, helium flow and therefore gas pressure can be neglected in all further measurements since current and flow are controlled by current source and flowmeter, respectively.

3.3.3 Aerosol production in dependency on the helium gas flow

The variation of the gas flow follows the fact that different flows through tubes with a defined diameter cause different pressures. This effect can be minimized by using a large

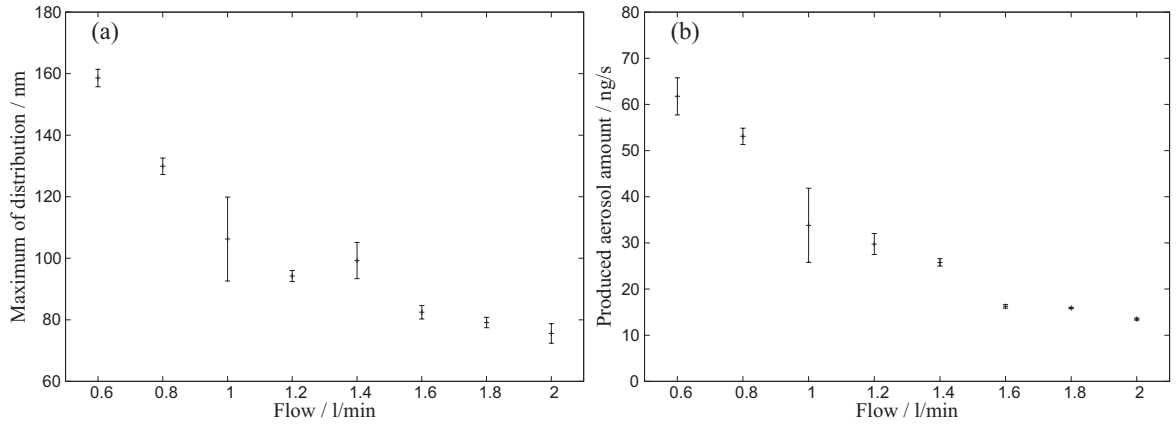

Figure 3.9: Maximum of the size distribution (a) and produced amount of aerosols per unit time (b) as a function of the helium flow. The maximum of the size distribution and thus the whole distribution shifts to lower particle diameters. But also the produced amount of aerosols decreased significantly with increasing flow.

tube. Due to the design of the aerosol generator a tube with a diameter of 2.5 mm has been chosen and kept as short as possible in order to guarantee that no pressure can build up due to its length. The diameter matches the size of the outlet of the aerosol generator. An increase of the pressure could not be avoided completely but the maximum pressure difference was only 160 mbar in the full measurement range from 0.5 $\frac{\text{l}}{\text{min}}$ to 2 $\frac{\text{l}}{\text{min}}$ with a pressure of 1045 mbar and 1255 mbar, respectively.
It is expected that the variation of the flow has no significant influence on the discharge and therefore on the produced amount of aerosols. In addition the increasing flow increases the effect of the turbulences inside the aerosol generator and thus it is not astonishing if less aerosols are flushed out of the generator at higher flows. Additionally it has to be assured that the flow in the tubes is not supersonic as the occurring turbulences would also decrease the detected number of aerosols. But this effect is irrelevant in this case due to the diameter of the used tubes and the high sonic velocity of helium of 981 m/s under normal conditions. It was also observed that an increase of the flow causes a shift of the maximum of the size distribution to smaller diameters [84]. Since less carbon is evaporated per unit of gas volume at higher gas flows the probability that particles absorb each other decreases. This effect has already been tested for flows from 10 $\frac{\text{l}}{\text{min}}$ to 40 $\frac{\text{l}}{\text{min}}$. As shown in Fig. 3.9(a) the maximum of the size distribution and thus the whole distribution behaves as expected since the maximum of the size distribution shifts to smaller diameters for an increasing flow. Concerning the amount of produced aerosols it was observed, as shown in Fig. 3.9(b), that the produced mass decreases with an increase of the flow as well. But this is not as unexpected as it seems because the measurement range decreases with an increasing flow rate as the Electrostatic Classifier can not handle large aerosols at high flows. The largest detectable size decreases from 526 nm at 0.5 $\frac{\text{l}}{\text{min}}$ to 198 nm at 2 $\frac{\text{l}}{\text{min}}$. Thus a smaller fraction of the generated aerosols is detected at higher flow rates. Furthermore it is not possible to compare single particle size intervals since the maximum also shifts

# of filter	flow / l/min	Δm / mg
I	0.5	0.5 ± 0.2
II	0.5	0.7 ± 0.2
III	1.8	0.7 ± 0.2
IV	4.0	0.6 ± 0.2

Table 3.1: Measured aerosol amount in dependency of the flow. Aerosols have been collected on a filter for seven hours. By weighing the filter before and after the collection the aerosol mass has been determined.

in the measurement. Hence, this has to be tested independently from the Classifier and thus independently from the aerosol size. As already mentioned before, it is not possible to perform a chemical analysis since the filter and the aerosols both consist of carbon. Thus, the aerosols have been collected on a filter with a sufficient small pore size and a high durability as behind the filter a low-pressure has to be created to prevent turbulences as much as possible. Aerosols have been collected for seven hours on a filter at different flows and its weight has been measured to determine the amount of the collected carbon.
With the result shown in Tab. 3.1 it is clear that the mass of the vaporized carbon is the same for all helium gas flows. The large error of the measured weight is due to the method itself: As it is not possible to separate filter and aerosols, the mass of the filter is weighted, which causes an error of 0.1 mg due to the precision of the balance. After each day of operation the aerosol generator has to be cleaned and therefore dismounted. As it is not possible to adjust exactly the same distance between the two electrodes, the discharge frequency and therefore the evaporated mass can not be exactly reproduced keeping all other settings identical. Nevertheless, the independency of the produced mass from the gas flow was verified within the given uncertainties with this method.

3.3.4 Aerosol production in dependency on the gas pressure

For the thermalization of fission products an overpressure of 1.7 bar is required inside the target chamber. Hence, also the aerosol generator is operated at overpressure under experimental conditions and therefore investigations on the aerosol production process at different pressures are necessary. To avoid effects of a changing flow it is necessary to obtain different pressures at the same flow. This has been realized by using a capillary with an inner diameter of 0.86 mm and a length varying from 0.1 m to 5.2 m mounted between aerosol generator and SMPS. To reach the lowest pressure the capillary has been entirely removed. Particles can get lost due to sedimentation in case of large particles and for very small aerosols due to collisions with the capillary wall caused by Brownian motion. After the experiment was continuously performed for several hours it was observed that the capillary was blocked by aerosols, which attached themselves to the wall of the capillary. The ideal solution is a tube-filter, which is a rolled-up tube of about 10 to 15 meters length and a diameter of several millimeters, mounted between aerosol generator and capillary in order to give the light and heavy aerosols enough time to attach to the tube wall. Hence,

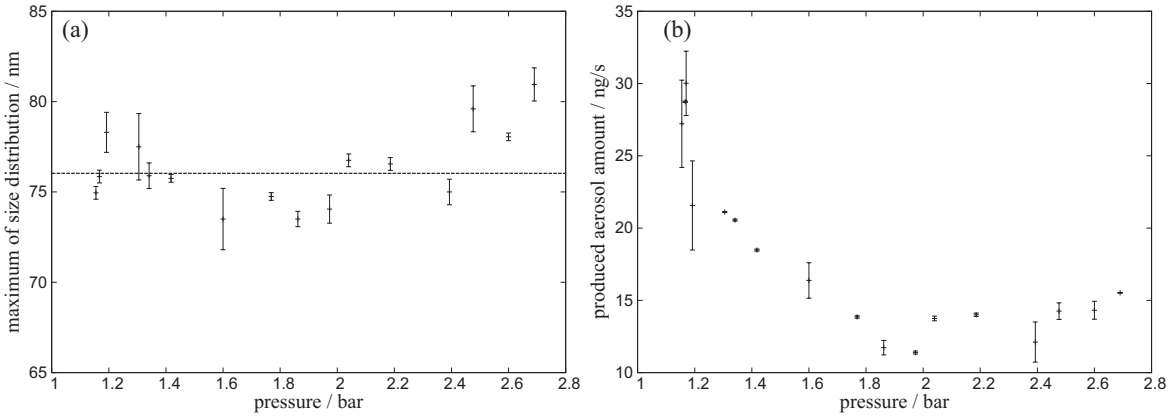

Figure 3.10: Maximum of the size distribution (a) and produced amount of aerosols per unit time (b) in dependency of the helium gas pressure. The measurements have been performed at a flow of $1.8\,\frac{\mathrm{l}}{\mathrm{min}}$ and a loading current of $I_C = 2.35\,\mathrm{mA}$. The maximum of the size distribution fluctuates in a range of about 10 nm with a calculated mean value of (76.0 ± 3.9) nm, whereas the produced amount of aerosols decreases down to 12 ng/s by increasing the pressure.

most of these aerosols are cut off in this tube and can not block the capillary, which causes a decreasing transport efficiency.
The values shown in Fig. 3.10 are in both cases the weighted means of two measurements whereas the maxima are calculated from a fit to the size distributions with the errors being the calculated weighted standard deviations. The measurements have been performed at a flow of $1.8\,\frac{\mathrm{l}}{\mathrm{min}}$ and a loading current of $I_C = 2.35\,\mathrm{mA}$. In Fig. 3.10(a) the position of the maxima of the aerosol size distribution is presented. The values fluctuate around a mean size of (76.0 ± 3.9) nm, which means in conclusion that the size is as expected not effected by the pressure.
The produced mass per unit time is shown in Fig. 3.10(b). It has been observed that the number of aerosols decreased at higher pressures. However, since the length of the capillary was changed as well for each data point it is most likely that the transport efficiency of the aerosols to the SMPS is less for longer capillaries, since the possibility that an aerosol particle attaches to the wall of the capillary due to diffusion processes increases with the capillary length. Therefore it was not possible to investigate whether the produced amount of aerosols depends on the gas pressure or not. As the pressure only fluctuates in a small range this has no effect on the experiment and according to the required pressure inside the target chamber only the increase of the loading current can increase the number of aerosols.

3.3.5 Structure of the aerosols

The determination of the aerosol size distribution is based on the assumption that they form spheres. Thus, it is interesting to know the real shape of the aerosols, which can

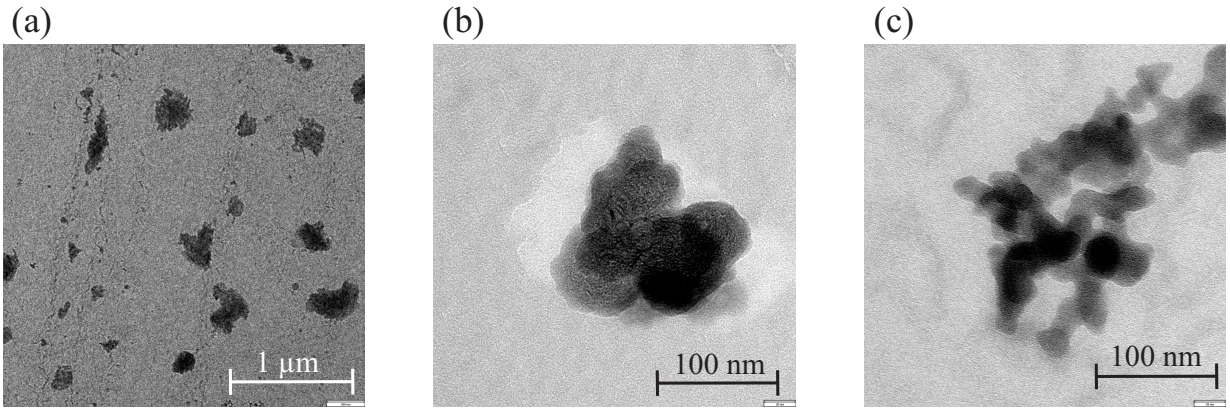

Figure 3.11: TEM pictures of different aerosol particles. As the particles are tridimensional, the darkness of a region indicates the amount of carbon in the third dimension, whereas the gray background belongs to the lattice. An overview of a larger region is presented in (a) containing particles with sizes between 50 nm and 500 nm. In (b) a single particle with a mean diameter of about 100 nm is shown with a non-spherical shape. Photo (c) shows the structure of a larger particle, which is neither massive nor spherical.

be investigated with transmission electron microscopy (TEM). Therefore the aerosols are collected on copper lattices with a diameter of 3 mm covered with a thin carbon layer. Several of these lattices are fixed on a filter with 27 mm diameter and placed inside a small chamber with a filter holder. The gas containing the aerosols is guided into the chamber in such a way that the aerosols hit it perpendicular to their direction of motion. A collection time for the aerosols of one minute was used to provide a sufficient particle density on the samples and in order to locate them faster with the TEM. In case of longer collection times the aerosols agglomerate to larger particles if they touch each other on the lattice and the particles become indistinguishable. A loading current of $I_C = 1.25\,\mathrm{mA}$ and a helium gas flow of $1.4\,\frac{\mathrm{l}}{\mathrm{min}}$ were used for collection.
Some representative pictures taken with the TEM are presented in Fig. 3.11. The gray scale is an indicator for the amount of carbon in this region, the darker the spots the higher is the amount of carbon, whereas the brighter background belongs to the lattice. The overview in Fig. 3.11(a) shows several aerosols with sizes from less than 100 nm to nearly 1 μm. In Fig. 3.11(b) a particle with a size of about 100 nm is shown, which is according to Fig. 3.9(a) the maximum of the size distribution for the chosen helium flow. In order to analyze the structure of the aerosols Fig. 3.11(c) shows a photography of a large particle. The conglomerates are not massive spherical particles as indicated by the gray areas within the aerosol. In comparison with Fig. 3.11(a) and Fig. 3.11(b) it was observed that smaller particles are mainly massive but most likely no spheres as well.
This raises the question to what extent the made assumptions are correct. Since the shape of small particles is partially spherical and the shape of large particles deviates significantly from a sphere the deviation between the real non-spherical and the assumed spherical shape is small for small particles up to diameters of about 100 nm. In addition, the properties

of the Electrostatic Classifier do not allow to detect large particles with a size > 500 nm. Thus, the spherical assumption represents the reality in a sufficient way for the detected aerosol sizes.
For KCl aerosols the result has been different as they do not form agglomerates like carbon. It was investigated that the KCl particles form small crystals of cubic or rectangular shape with a mean diameter between 50 and 200 nm [36].

3.3.6 Long-time stability of the aerosol production

Laser spectroscopic and mass spectrometric investigations on fission products with low production rates can last several hours. As the aerosol generator has to run continuously during the experiment it is important to know, whether the aerosol production process is stable enough on a long timescale. Thus a long-time stability test has been performed with a helium gas flow of 0.6 $\frac{\mathrm{l}}{\mathrm{min}}$ and a loading current of $I_C = 2.35\,\mathrm{mA}$. In order to assure ideal conditions the electrodes have been sharpened and the aerosol generator has been cleaned

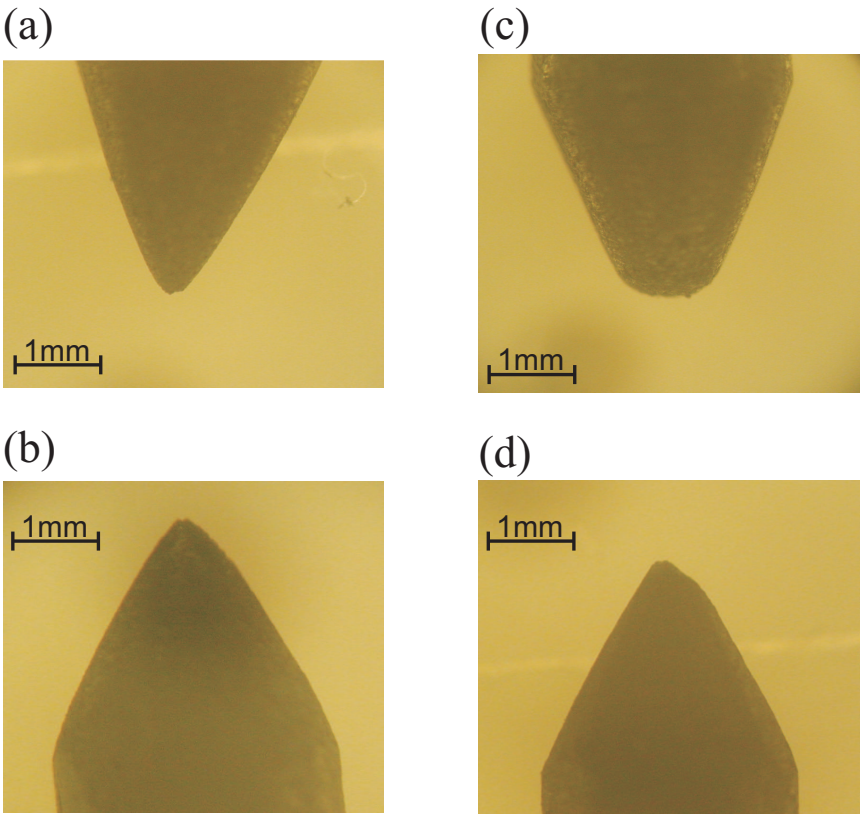

Figure 3.12: Photographies of the electrodes. The upper (a) and lower electrode (b) after maintenance are sharp and clean. In figure (c) and (d) the electrodes are shown after eight hours of continuous operation. Due to the evaporation of carbon during operation the electrodes are slightly deformed especially the upper electrode (c).

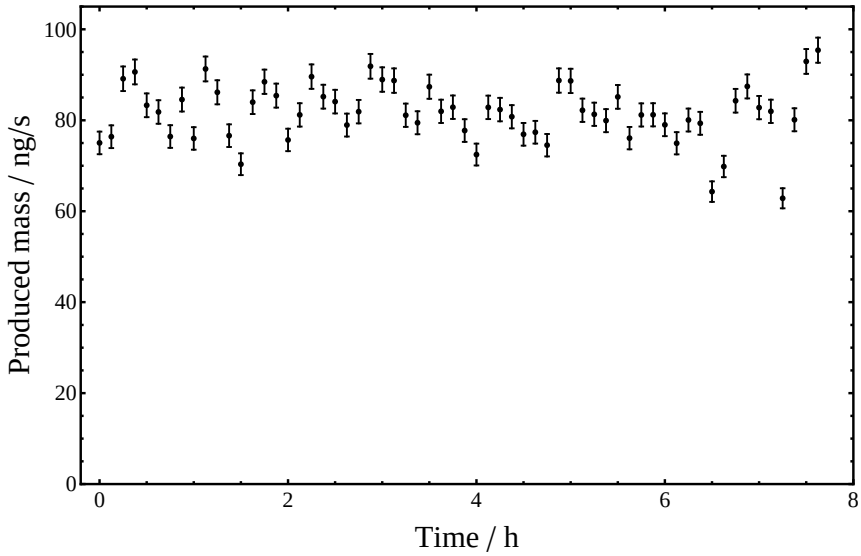

Figure 3.13: Long-time measurement of the produced aerosol amount at a helium flow of 0.6 l/min and a loading current of $I_C = 2.35\,\mathrm{mA}$. The mass flow remains (81.6 ± 6.5) ng/s during the whole measurement period.

properly. It is expected that produced amount of aerosols fluctuates around a certain value and decreases due to deformations of the electrode tips and an increase of their distance due to constant erosion of the electrodes by the carbon evaporation in discharges. Also a sudden increase might happen if the shape of the tips changes due to mechanical changes like truncations.
Photographies of the sharpened upper and lower electrodes, respectively, are shown in Fig. 3.12(a) and (b), Fig. 3.12(c) and (d) show the same electrodes after about 8 hours of continuous operation with about two discharges per second. A deformation is clearly visible at the upper electrode (see Fig. 3.12(c)) but not at the lower one (see Fig. 3.12(d)). The produced mass flow of aerosols is presented in Fig. 3.13. An average production rate represented by the mass flow of (81.6 ± 6.5) ng/s was observed. As one measurement cycle takes about 10 min the measured value is the average amount produced in this time and the points are placed in the center of this time interval. The error of the values result from the counting error of the number of aerosols, from which the mass is calculated.

One can conclude that the aerosol production is at least stable for eight hours and it is possible to run the experiments TRIGA-TRAP and TRIGA-LASER for this time without maintenance of the aerosol generator. As instead of the capillary only a short tube has been used the measured production is almost completely free of losses. This is an important result as it provides the possibility to get a constant rate of aerosol particles for a long time. Furthermore the aerosol generator itself is not the source of larger fluctuations or decrease of the transmission rate in case that this is observed during the experiment since the production rate is constant.

3.3.7 Offline tests of the aerosol transport under experimental conditions

During the investigations of fission products the target chamber containing the fissionable material is placed inside the reactor. Thus, target chamber, beam tube, and gas tubes are irradiated by neutrons as well during irradiation of the target. For radiation safety issues the following test construction has been chosen: The target chamber is made of titanium and the tubes are made of polyethylene containing mainly carbon, which are by neutron capture only transformed into short-lived radionuclides. The connectors between tubes and target chamber contain steel, which is activated by neutron capture and contains thus nuclides with half-lives of several years. The beam tube, a huge three meters long aluminum pipe, contributes as strongest source to the overall activity due to activated material impurities. Additional radiation coming from the irradiated target is not dominating. Therefore the target chamber and the beam tube are not accessible for any maintenance for at least two days if they were once irradiated. Thus, offline tests for the fission product transport are important to study the behavior of the aerosols in the setup as occurring blockages can not be removed and maintenance is impossible for all pieces in the beam tube during the decay time. It is expected that the aerosols block the capillary during operation as this has been observed during the investigation of the effect of a pressure variation.
Therefore the general setup shown in Fig. 2.5 has been used outside the reactor. As the target chamber which will be used inside the reactor has already been activated, a Plexiglas model has been used to have access during operation. The aerosols were produced in the aerosol generator and guided to the target chamber through a tube filter, which was in this case a 13 m long polyethylene tube with an inner diameter of 4 mm rolled up in 20 windings to let the major part of the heavy and the light ones sediment and diffuse to the wall, respectively. The gas flow of 2 $\frac{\text{l}}{\text{min}}$ has been chosen, which is the maximum flow that is accepted by the Classifier. At this flow the pressure in the target chamber is not always 1.7 bar, which is necessary for efficient thermalization in helium. Thus, the flow is increased until the thermalization pressure is reached. The aerosols were flushed out of the target chamber through an 8 m long capillary, which has been placed in straight line with an 180° turn after 4 m, to the classifier where they are counted. Directly in front of the classifier the gas flow is reduced by removing the additional gas in a direction being perpendicular to the aerosol flow to remove as less aerosols as possible. The turn represents the curve, when the capillary leaves the concrete shielding of the reactor and goes to the experiment. One measurement has been performed for each of the three capillaries of inner diameters 0.86 mm, 1.0 mm and 1.4 mm. During the measurement only the aerosol generator has been maintained to simulate real experimental conditions.
The result is presented in Fig. 3.14, in which the surface of the aerosols produced per second is plotted as a function of the operation time. This is a measure of the transport efficiency as the attachment of the fission products to the aerosols depends on their surface (see Eq. (2.14)). In Fig. 3.14(a) the transport through the small capillary with a diameter of 0.86 mm is presented. The surface flow and thus the efficiency decreases during operation. Some fluctuations were observed but maintenance of the aerosol generator like

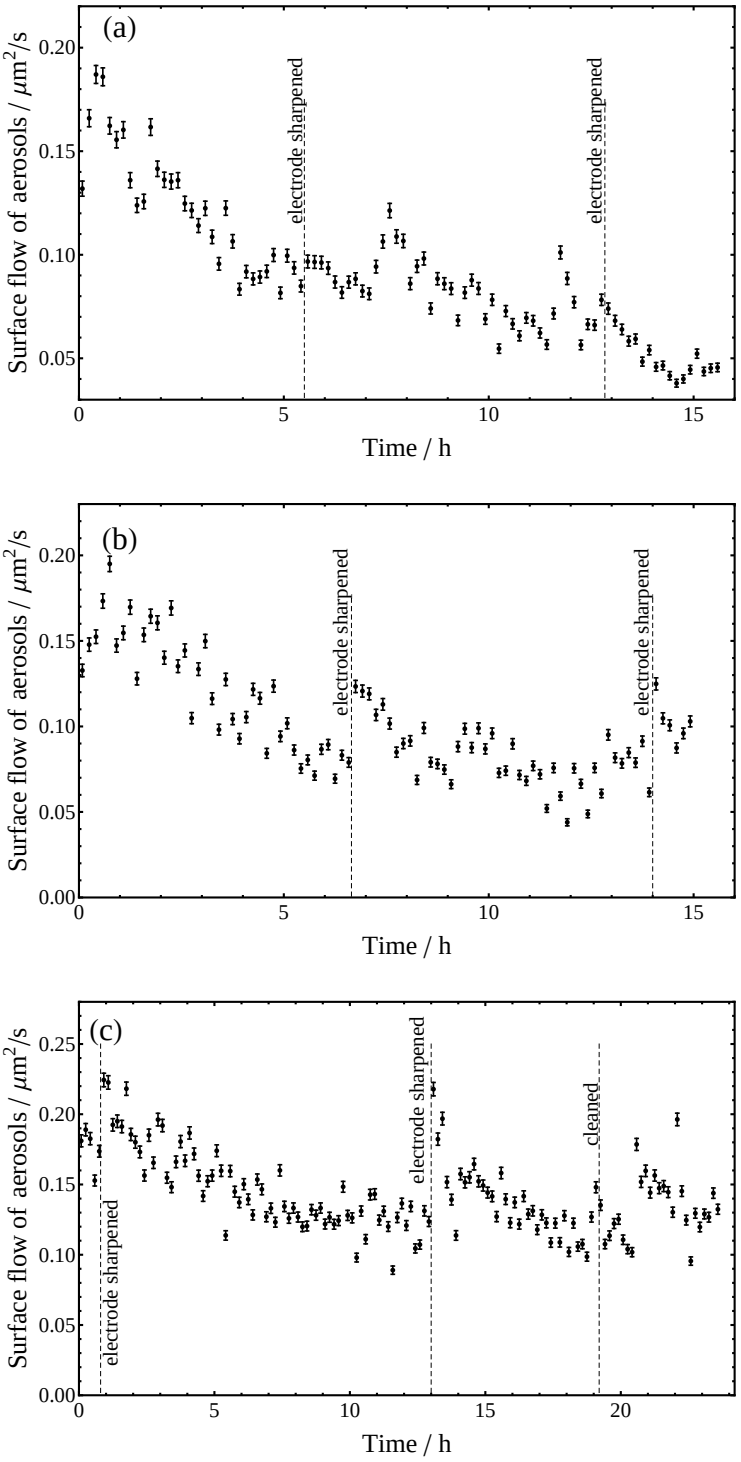

Figure 3.14: The surface flow of aerosols is plotted as function of time for capillaries with diameters of (a) 0.86 mm, (b) 1.0 mm, and (c) 1.4 mm. The surface is a measure of the transport efficiency as the attachment is proportional to the surface of the aerosols. A detailed description of the method and the drawn conclusions are presented in the text.

sharpening of the electrodes did not have any effect. The decrease of the produced aerosol surface is due to the deposition of aerosols inside the capillary during operation, especially at the entrance, which causes a decrease of the entrance diameter. Capillaries with an inner diameter of 0.86 mm have been used several times before [36, 67, 85] as they provide the necessary pressure inside the target chamber for efficient stopping of the fission products with a helium gas flow of about 1.4 $\frac{\text{l}}{\text{min}}$. Thus a capillary with this diameter has also been used later for the determination of the transport efficiency and several other investigations. Fig. 3.14(b) shows the trend of aerosol production for the capillary with an inner diameter of 1 mm. The decrease of the transport was observed as well within the first hours but with a smaller slope than for the smaller capillary. After a few hours the decrease became almost constant, whereas maintenances did not have any significant effects. This behavior has been in principle observed as well for the capillary with the largest diameter of 1.4 mm, as shown in Fig. 3.14(c). The difference is that after the first decrease, which lasted about eight hours, the transport has been more or less constant for additional 16 hours. So it has been demonstrated that it is possible to gain a rather constant flow with a capillary of a diameter of 1.4 mm for about 24 hours, which means in conclusion that this capillary is ideal for the experiment as a constant and sufficient high transport efficiency of fission products can be expected. For usage of the largest capillary a gas flow of about 7 $\frac{\text{l}}{\text{min}}$ is required to generate the pressure of 1.7 bar that is necessary for thermalization of the fission products. Hence, the gas load increases and a higher pumping capacity is required. Thus, the pressure inside the ECR ion source increases as well and the ionization efficiency decreases. Therefore the smaller capillary may be more useful under experimental conditions despite the decreasing transport efficiency. Before these tests it is required to investigate the extraction of the fission products through capillaries with different diameters to investigate parameters for efficient and fast transmission on a long timescale.

Chapter 4

Extraction of fission products

In the previous chapters the production method of the fission products as well as the transport mechanism were introduced and the properties of the aerosol generator were presented. In this chapter the results of online experiments are discussed, which aimed at the test of the extraction of fission products from the TRIGA reactor with a carbon aerosol gas-jet for the first time. The most important properties of the extraction process are transport efficiency, transport time and the absolute number of transported radionuclides. These parameters are of high interest for the experiments, since they determine which nuclides are available for later measurements at TRIGA-SPEC. The transport time to the ion source limits the accessibility of short-lived nuclides, whereas the transport efficiency limits the accessibility of nuclides with low production rates.
To determine the above mentioned specifications investigations with a ^{235}U target were performed, which required the operation of the TRIGA reactor in pulsed as well as in continuous mode. For optimization purposes it has been investigated how the transport of the fission products depends on the gas-jet parameters and which fission products could already be observed by a simple detection method used for the investigations presented in the following.

4.1 Experimental setup

A sketch of the setup for the extraction of fission products is shown in Fig. 4.1. A detailed description of the setup, which has been used within this thesis to characterize the extraction, is presented in the following. The carbon aerosols are produced inside a carrier gas within an electric discharge between two graphite electrodes as described in detail in Sect. 3.1.1. After the production they are guided through a 7 m long polyethylene tube to the target chamber. A detailed sketch of the chamber is presented in Fig. 4.2(a), a photography in Fig. 4.2(b).

The fissionable target material has been deposited on a titanium substrate and is fixed in the target chamber with an aluminum holder. The target chamber is inserted at beam port A and irradiated with a neutron flux of $9.8 \times 10^{10}\,\mathrm{n/(cm^2\,s)}$. During the irradiation

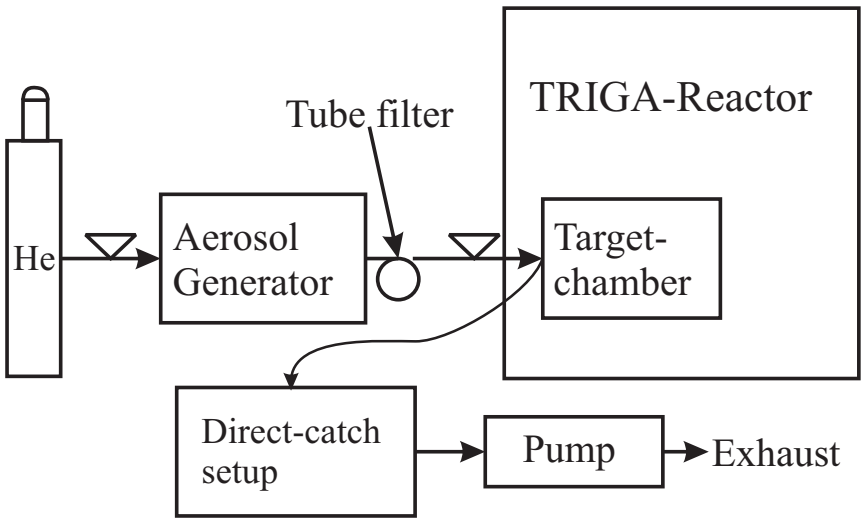

Figure 4.1: Setup used for investigations on the extraction of fission products. The carbon aerosols produced in a discharge within a helium gas atmosphere are guided to the target chamber close to the reactor core, where the fission products thermalize and attach to them. Afterwards they are extracted through a capillary to a chamber with a filter on which all particles are collected and subsequently identified by measuring the energy and intensity of their γ-radiation with a germanium-lithium detector (direct-catch setup). Further details are given in the text.

the fission products leave the target with kinetic energies of about 100 MeV and are thermalized inside a helium atmosphere at a pressure of 2.7 bar. The target has been covered with a thin aluminum foil in order to prevent heavy nuclides to leave the target since they are completely stopped inside the foil while a fraction of the light nuclides is transmitted partly losing their initial energies [86]. In this way the foil prevents the contamination of the setup with long-lived nuclides since most of the light radionuclides have half-lives of less than one day. The fission products coming from an uncovered target have to be thermalized in heavier gases, i.e. with nitrogen or argon, since the pressure needed to thermalize the fission products with helium would be too high for the target chamber. Thus some of the results presented here are only valid for covered targets. A list of the available targets is shown in Tab. 4.1. For all tests performed within this thesis the ^{235}U one covered with

Nuclide	Mass μg	Fission cross section / barn
^{235}U	310	586
^{239}Pu	300	752
^{249}Cf	300	1700

Table 4.1: Standard available targets for irradiation at the research reactor TRIGA Mainz. For all tests performed within this thesis the ^{235}U target covered with a 13 μm thick aluminum foil has been used. The fission cross sections are given as well [24].

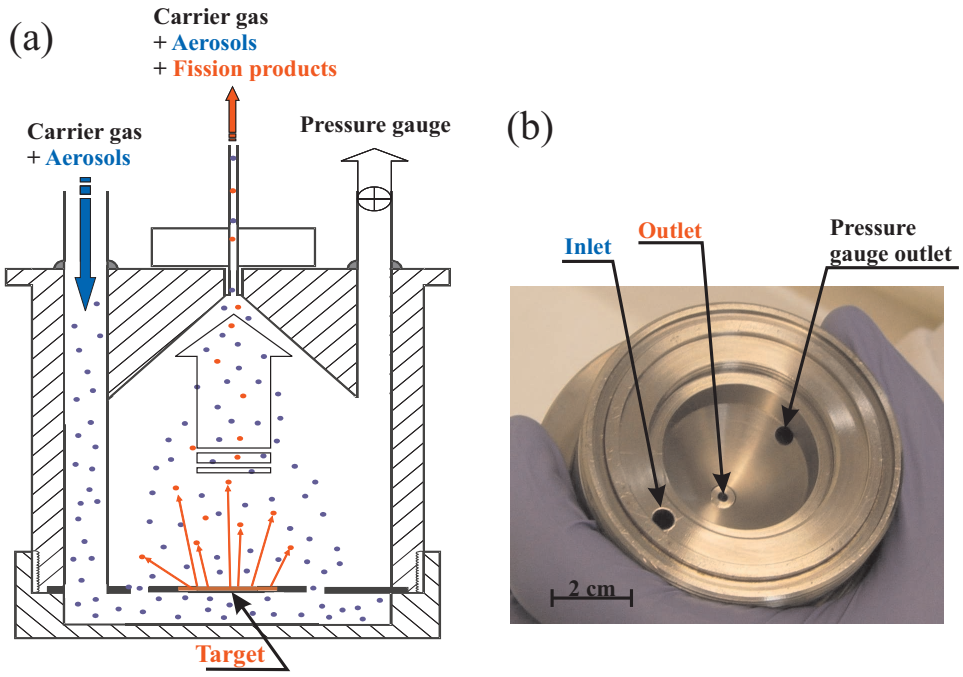

Figure 4.2: Sketch (a) and photography (b) of the target chamber. The target is placed inside the target chamber at a gas pressure of 2.7 bar. The aerosols pass the target as close as possible. This ensures that most of the radionuclides attach to the aerosols and leave the chamber through a capillary. Aerosols are marked blue and aerosols with attached fission products are marked red.

a 13 μm thick aluminum foil has been used.
After the production the aerosols are guided through the tube filter, a rolled up tube in which the heavy aerosols sediment due to gravity and their inertia and the light aerosols attach to the wall of the tube due to diffusion. The aerosols enter the target chamber through an inlet with a large diameter as shown in Fig. 4.2, are guided around the target and enter the thermalization area through small holes at the edge of the target holder. This ensures that the aerosols pass the target as close as possible to increase the possibility that fission products attach to them. The optimal shape of the target chamber, which is shown in Fig. 4.2(a), provides the highest efficiency and the fastest extraction as the gas is directed to the outlet without turbulences. This shape has been considered optimal after comparison with other designs [36]. During operation the pressure in the target chamber has to be controlled as it has to be high enough to ensure thermalization before the fission products reach the wall and low enough to prevent damaging the target chamber as radionuclides can exit through a leak. Therefore the flow is monitored by a pressure gauge that is directly connected to the thermalization region. As the pressure is dependent on the length and the diameter of the capillary at the outlet the pressure inside the chamber is regulated by changing the helium flow.
After thermalization and attachment to the aerosols the particles are flushed out through a

7 m long polyethylene capillary with an inner diameter that can be selected from 0.86 mm to 1.4 mm. The capillary guides the fission products to a small chamber, in which a filter with a very small pore size is placed to collect all transported particles. A vacuum pump is connected to the other side of the chamber. Thereby, turbulences inside the chamber are suppressed as well and thus the collection of all fission products on the filter is assured. After a short decay time of two minutes the filter with the collected fission products is placed in front of a germanium-lithium detector with an energy resolution of $E/\Delta E = 8000$ to measure the intensity and the energy of the emitted radiation. This waiting time is necessary to ensure that the short-lived radionuclides do not contribute to the following measurement, which is important because their presence disturbs the detection as they decay to observed long-lived species and thus even differences of milliseconds in the measurement cycle of collection, decay and detection can cause large differences in the measured result. This is in addition important if their emitted γ-quanta have energies near the ones of the observed fission products. Hence, it has to be waited until most of the short-lived fission products are decayed. As the radiation emitted during the decay of an excited nuclear state has a characteristic energy, the radionuclides inside the sample can be identified. For the observation time of the fission products investigated here a cycle of two minutes collection time, two minutes decay time and five minutes measurement was used.

4.2 Detection of fission products

Considering the production rates of fission products from the ^{235}U target, which are presented in Fig. 4.3, the radionuclides in the production rate maximum of the light masses are most likely detectable. These are nuclides of krypton, rubidium, strontium, yttrium and zirconium. Krypton can be neglected as it is a noble gas and therefore will rarely attach to the aerosols. Thus its characteristic γ-lines will be hidden in the background. The short half-life of some of the fission products, e.g. ^{101}Nb with 7.1 seconds, has to be considered as well. It is clear that only radionuclides with a sufficient high production rate and a half-life of more than approximately thirty seconds are observable as it is not possible to remove the filter from the chamber and place it in front of the detector in a shorter time. In addition radionuclides with a very long half-life, e.g. ^{97}Zr with 16.9 hours, will not be detected as their γ-activity is so low that they are hidden in the background. This could be realized by an extension of the measurement time but is most likely not possible due to the background radiation emitted by the reactor and the other collected fission products as well. Other parameters are important for the observation of fission products as well. The experimental limitations are that only nuclides that emit γ-radiation of a certain energy with a sufficient high intensity can be detected. Another crucial point is the detector itself as it is possible that some lines overlap due to its resolution of $E/\Delta E = 8000$ and that the efficiency of the radiation detection is too low in a certain energy region to count enough quanta.

After the fission products have been collected on a filter, which has been placed in front

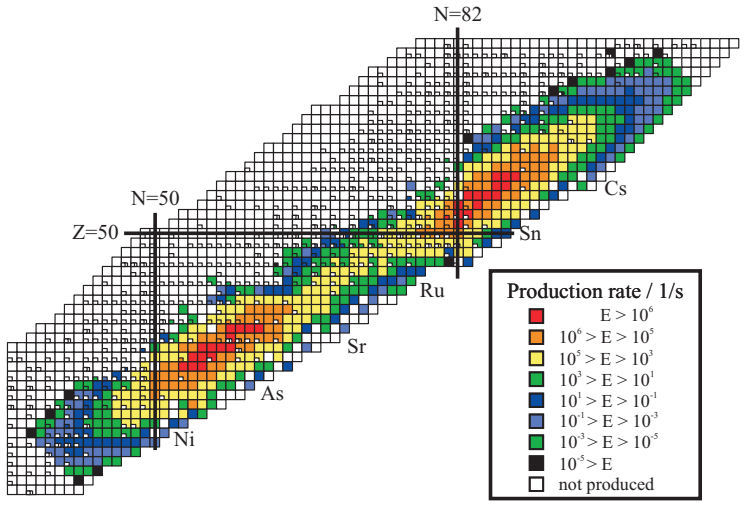

Figure 4.3: Individual production rates of fission products from the ^{235}U target at beam port A at a steady state power of 100 $\mathrm{kW_{th}}$. According to Fig. 2.3 the production rate has been calculated for the uncovered ^{235}U target with a mass of 310 μg irradiated with a neutron flux of 9.8×10^{10} n/(cm^2 s).

of a germanium-lithium detector, the emitted radiation was detected and its energy has been determined in order to identify the transported radionuclides. The number of emitted γ-quanta in dependency of their energy has been counted by the detector and is presented in Fig. 4.4. The identified γ-lines are presented in the plot and belong to ^{84}Se, ^{93}Sr, ^{94,95}Y,

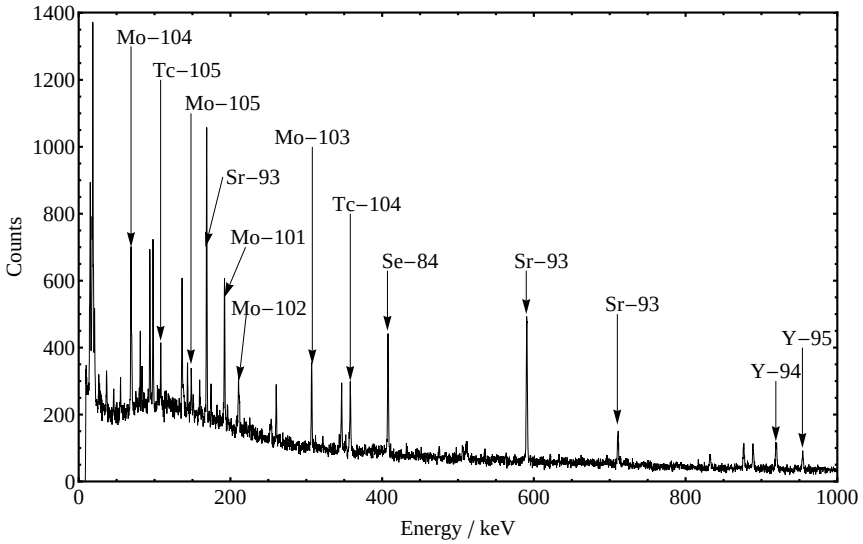

Figure 4.4: γ-spectrum of the fission products of ^{235}U. Activity in dependency of energy has been recorded and the identified radionuclides have been marked. The peaks without marks could not be identified with fission products extracted from the reactor.

Nuclide	Half-life	γ-line / keV	Mass uncertainty Δm / keV	Relative mass uncertainty $\Delta m/m$ / 10^{-8}	Ref.
^{84}Se	3.1 min	408	2	2.6	[87]
^{93}Sr	7.45 min	168, 590, 710	8	8.5	[1]
^{94}Y	18.7 min	918	7	8.5	[1]
^{95}Y	10.3 min	954	7	8.4	[88]
^{101}Mo	14.6 min	192	6	6.0	[1]
^{102}Mo	11.3 min	211.5	10	21.6	[89]
^{103}Mo	67.5 s	308.5	10	68.0	[89]
^{104}Mo	60 s	69	10	57.7	[89]
^{105}Mo	35.6 s	148	10	76.3	[89]
^{104}Tc	18.2 min	358	50	48.1	[1]
^{105}Tc	7.6 min	108	60	57.2	[1]

Table 4.2: Properties of the observed fission products. The values for half-life and γ-energy were taken from [90]. The mass values are taken from the references given in the last column.

$^{101-105}$Mo and ^{104,105}Tc (see Tab. 4.2). Since the mass uncertainties of the detected molybdenum and technetium isotopes are about $6 \cdot 10^{-7}$, it is expected that their masses can be measured at TRIGA-TRAP with higher precision. In addition high-precision laser spectroscopic data is not existing for these isotopes, which can be obtained at TRIGA-LASER. With $T_{1/2} = 35.6\,\mathrm{s}$ ^{105}Mo is the shortest-lived nuclide that has been identified with this method, which has only been possible due to its high cumulative production rate[1]. In the low energy region background lines are observed, which belong to characteristic X-rays emitted by other fission products on the filter or to radiation emitted by fission products inside the fuel rods of the reactor.

4.2.1 Verification of the calibration of the γ-detector

To confirm the identity of the detected radionuclides it is necessary to verify the energy calibration of the detector. Therefore, the same measurement cycle has been used as for the identification of the fission products in order to associate a nuclide to a γ-line by the determination of its half-life considering the decrease of the radiation intensity. In this case a line at $E_\gamma = 192\,\mathrm{keV}$ was investigated, which should correspond to ^{101}Mo with a half-life of $(14.61 \pm 0.03)\,\mathrm{min}$. The 192-keV line of ^{101}Mo provides ideal conditions for this test, since there is no line of other expected fission products close in energy and the half-life of ^{101}Mo is long enough to record a sufficient number of data points.
First a Gaussian distribution modified with a stretching factor A reflecting the area under the curve has been fitted to the recorded peak at 192 keV in each recorded spectrum as

[1] The cumulative production rate of a nuclide is the sum of the individual production rate of the nuclide of interest and the individual production rates of its mother nuclides.

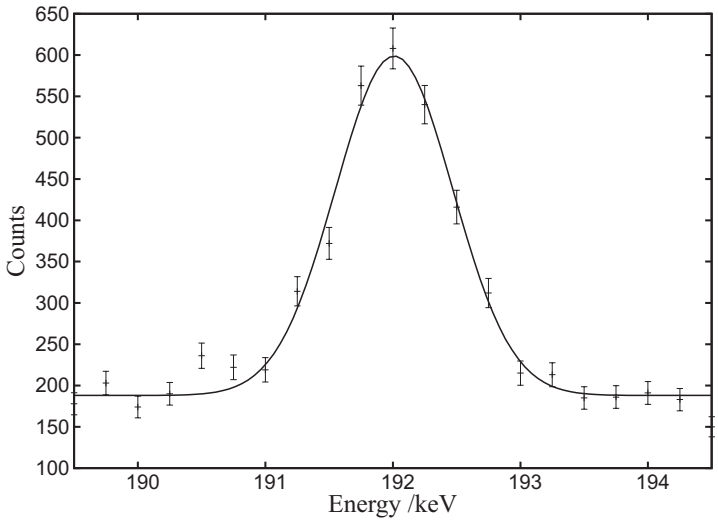

Figure 4.5: Fit of a modified Gaussian distribution to the ^{101}Mo γ-peak at $E_\gamma = 192\,\mathrm{keV}$.

shown in Fig. 4.5. A straight line with offset respects the background, which is approximated to be linear on a small scale:

$$f(x) = \frac{A}{\sqrt{2\pi}\sigma} \exp\left(-\frac{(x-x_a)^2}{2\sigma^2}\right) + s \cdot x + y_a \quad . \tag{4.1}$$

In this equation x_a denotes the position of the line maximum, σ the line width, s and y_a the slope and offset of the straight line, respectively. The number of decay events is calculated by integration of the Gaussian distribution after subtracting the background. Considering the decay law the number of counts N_1 in the first measurement interval is the difference of the nuclides at the beginning $t = 0$ and the number of nuclides remaining at the end of the interval $t = \Delta T$, which leads to

$$N_1 = N_0 \left(1 - e^{-\frac{\ln 2}{T_{1/2}}\Delta T}\right) \quad . \tag{4.2}$$

Dead time effects and the detector efficiency can be neglected as the absolute number of particles is unimportant for this calculation. A generalization to any other interval can easily be done by the integration of the decay law:

$$N_i = \int_{(i-1)\Delta T}^{i\Delta T} \mathrm{d}t\, \lambda N_0\, e^{-\lambda t} = N_0\, e^{-(i-1)\lambda\Delta T}\left(1 - e^{-\lambda\Delta T}\right) \overset{\text{Eq. (4.2)}}{=} N_1\, e^{-(i-1)\lambda\Delta T} \tag{4.3}$$

with the decay constant $\lambda = \frac{\ln 2}{T_{1/2}}$, the length of the detection intervals ΔT and the total number of nuclides at the beginning N_0, which is here a modified value due to the neglected dead time and detector efficiency. Thus, the decay law is fitted to the data to obtain the half-life $T_{1/2}$ of the 192 keV line. In Fig. 4.6 the experimental data and the fit curve are shown. A half-life of $(14.56 \pm 0.26)\,\mathrm{min}$ has been determined, which is in excellent agreement with the published value of $(14.61 \pm 0.03)\,\mathrm{min}$. Hence, it has been verified that the peak at $E_\gamma = 192\,\mathrm{keV}$ belongs to ^{101}Mo and thus the energy calibration is correct.

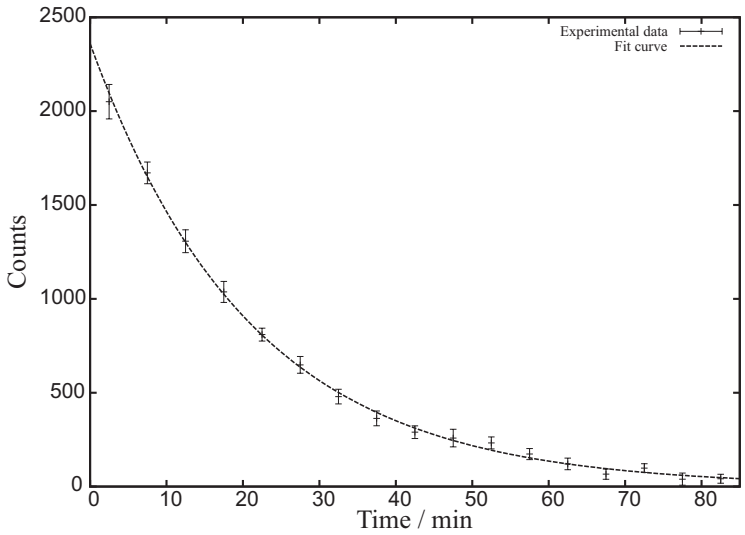

Figure 4.6: Fit of the decay law to the data. The half-life of the nuclide corresponding to the 192-keV line was determined to be (14.56 ± 0.26) min. This is in excellent agreement with the published value of (14.61 ± 0.03) min [90].

4.2.2 Extracted fission products as a function of the number of aerosols

The number of aerosols is a crucial parameter for the transport of the fission products, since a higher aerosol density increases the probability that fission products attach to the aerosols and are transported to the detector. As aerosols deposit themselves at the capillary walls and block the route of transport at critical positions like the outlet of the target chamber, a too high aerosol density can also decrease the transport efficiency. This shows that it is important to investigate the dependency of the transport of the fission products on the number of aerosols, which is represented by the loading current applied to the capacitor of the aerosol generator, to find a compromise between the number of transported fission products and used amount of aerosols.
For these investigations the number of aerosols has been varied by setting different values of the loading current of the capacitor and recording the associated γ-spectra. In order to assure comparability of the individual spectra, the measurement cycle, which was identical with the one used for the fission product identification, has been kept equal for all measurements. Before the data evaluation the number of counts has to be corrected for dead-time effects with the formula

$$c_{\text{true}} = c_{\text{meas}} \frac{1}{1 - T_{\text{sat}}/T_{\text{meas}}} \tag{4.4}$$

where c_{true} denotes the true count rate, c_{meas} the measured count rate, T_{meas} the measurement time and $T_{\text{sat}} = N_{\text{meas}} \cdot \tau$ the saturation time of the detector with the measured number of counts N_{meas} and the dead time of the detector τ. The rest of the evaluation has been done in two different ways to verify that they yield the same result.

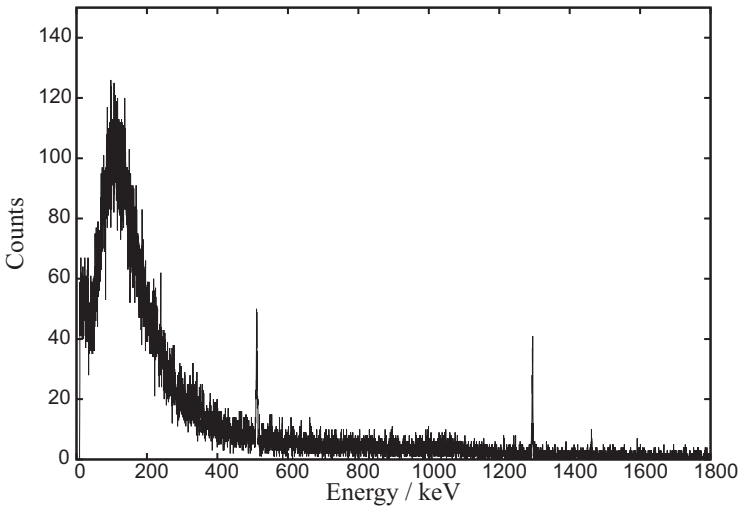

Figure 4.7: Typical background spectrum in the reactor hall during the operation of the reactor in continuous mode at 100 kW_{th}. The maximum of X-ray and Compton radiation is determined to be at an energy of approximately 120 keV. The peaks at $E_\gamma = 511$ keV and $E_\gamma = 1461$ keV are due to the positron-electron annihilation and the decay of ^{40}K, respectively. The peak at $E_\gamma = 1294$ keV is due to the decay of ^{41}Ar, which is produced during the reactor operation from the naturally existing argon.

The first method compares the sum of all counts in the spectra. During the previous measurements the appearance of a γ-line at $E_\gamma = 1294$ keV was observed. Thus, it has been decided to determine the background before the first, after the last measurement and sometimes between two measurement cycles while the reactor was running to examine its change during the day. A typical background spectrum is shown in Fig. 4.7. The major part of the background consists of X-ray and Compton radiation, which is mainly constant and only present when the reactor is running. In addition a γ-line at 511 keV from positron-electron annihilation is visible. The positrons appear due to pair production from photons having higher energies than 1022 keV. The only directly visible change during the day is the increase of the line at $E_\gamma = 1294$ keV, which was identified as ^{41}Ar. Due to the activation of naturally existing argon in the air by neutron capture, ^{41}Ar is continuously produced during the operation of the reactor and decays with a half-life of 1.83 h. According to the sensitivity of the measurement, which is limited due to the emission of γ-radiation from the filter in front of the detector, only the line at 511 keV can be observed under experimental conditions. In addition a straight line has been fitted to the total amount of background counts in dependency of the time and its slope has been found to be negligible. Thus only a mean background spectrum has been subtracted from each γ-spectrum of the fission products. The second method is basically the same as the one described in Sect. 4.2.1, which makes a background correction unnecessary as it is included in the fit of the Gaussian distribution. The now confirmed peak of ^{101}Mo has been integrated to calculate the numbers of counts as before.

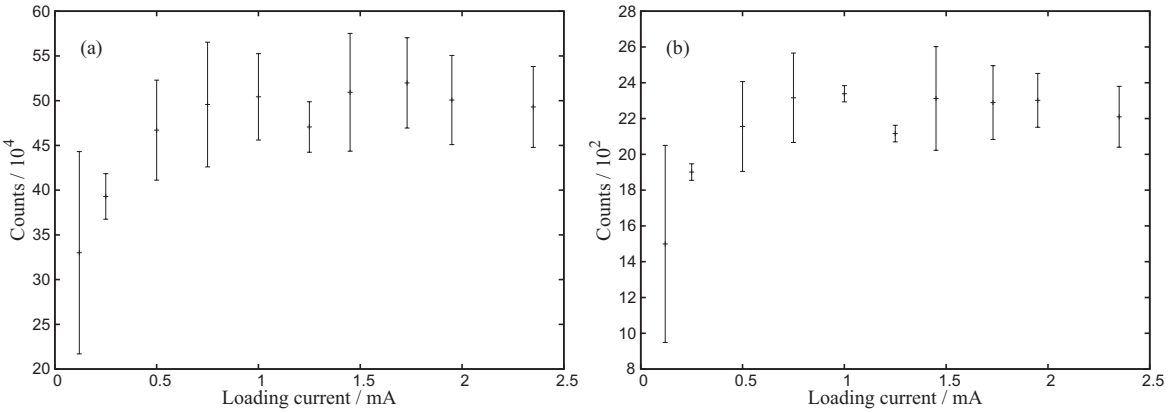

Figure 4.8: Sum of all counts in the overall spectrum (a) and sum of the counts in the integrated ^{101}Mo peak at $E_\gamma = 192\,\mathrm{keV}$ (b) in dependency of the number of aerosols reflected by the loading current. Each data point is the weighted mean of two to three integrated γ-spectra with statistical uncertainties. A total online running time of about four hours was used for these measurements. The errors given here are the weighted standard deviations of these values.

To gain better statistics two to three measurements have been performed for each data point. The result of these measurements evaluated with the first and the second method is presented in Fig. 4.8(a) and (b), respectively, where each data point is the weighted mean of its associated measurements and the errors are their weighted standard deviations.
As one can see, Fig. 4.8(a) and (b) are very similar and the tendency is clearly visible. Currents of approximately 0.75 mA and higher result in the same transported amount of fission products. The uncertainty of the first value is very huge with about 33% due to the limited statistics. In addition it is remarkable that the errors in Fig. 4.8(b) vary in a large range and in addition the errors are a little bit smaller than in Fig. 4.8(a) since the second method does not depend on small variations in the background or in other γ-lines. The difference of the error of the first value is an indication for mechanical changings of the electrodes during one measurement or it is due to the very unstable discharge frequency for low currents. Thus, the produced aerosol amount per unit time can vary in a wide range. This indicates the severe problem of fluctuations of the transport efficiency already observed and discussed by Wollnik *et al.* [91]. Thus, the conclusion is drawn that both methods produce qualitative equal results for investigations concerning the whole energy range at high activities.
Since the aerosols deposit themselves inside the capillary it is necessary to guide as less aerosols as possible through the setup. Thus, a loading current of about 0.8 mA seems to be optimal for the aerosol under experimental conditions as the transported amount of fission products saturates at this point.

4.2.3 Extracted fission products as a function of the aerosol size

It has been demonstrated in Sect. 2.3 and 3.3.3 that the attachment of fission products to aerosols depends on their surface and that it is possible to vary the maximum of the aerosol size distribution by the variation of the helium flow. Thus investigations on the transport with aerosols of different sizes are required to prove this behavior. For this purpose the setup was modified. As indicated in Fig. 4.9 the classifier has been attached between the target chamber and the direct catch setup in order to select one single size interval of particles after the attachment of the fission products (see Sect. 3.1.1). The aerosols of the selected size have been collected on a filter to measure their radiation. The remaining aerosols have been guided to a second filter, which has the function to clean the gas before reaching the exhaust. During the selection process aerosols that are smaller and thus lighter than the ones in the selected size interval attach themselves to the collector rod. Hence, during the whole measurement cycle fission products are deposited inside the Electrostatic Classifier. Therefore this kind of investigation is only suitable in combination with a covered target as almost none of the fission products has a half-life of more than a few days. In addition the few light long-lived radionuclides have very low production rates. Since only short-lived radionuclides have been investigated a contamination of the classifier is of no concern after a couple of hours waiting time. If this test would be performed with an uncovered target it would be necessary to provide a monodisperse aerosol to the fission products. Thus the size selection would have to be mounted in the overpressure region in front of the target chamber, which is complicated as the flowmeters inside the classifier are calibrated to normal pressure and the selection would have to be done at approximately 1.7 bar overpressure. A calibration for that pressure is not available and thus a proper selection of the aerosol size in this configuration is not possible.
Thus, for this measurement it was required to extend the collection time as the number of particles in one size interval is at least two orders of magnitude less than the total number of particles. On the other hand the collection time is limited as ^{101}Mo, which is used again as a test candidate, has only a half-life of about 14.6 minutes. To determine a sufficient collection time it has to be considered that the existing ^{101}Mo-nuclides decay according to the decay law while a constant rate k is collected assuming that the gas jet efficiency is constant. Thus the change of the particle number $N(t)$ on the filter is

$$\dot{N}(t) = -\lambda\, N(t) + k \tag{4.5}$$

with the decay constant $\lambda = \frac{\ln 2}{T_{1/2}}$. Solving this differential equation results in the number of particles at a time t

$$N(t) = \frac{k}{\lambda}\left(1 - e^{-\lambda t}\right) = \frac{k\, T_{1/2}}{\ln 2}\left(1 - e^{-\frac{\ln 2}{T_{1/2}}\, t}\right) \quad , \tag{4.6}$$

which converges to a constant value and thus to a constant maximum activity for long collection times. Hence, it is not necessary to collect longer than $3.5 \cdot T_{1/2}$ since already more than 90% of the maximum number is reached then. This implies a collection time

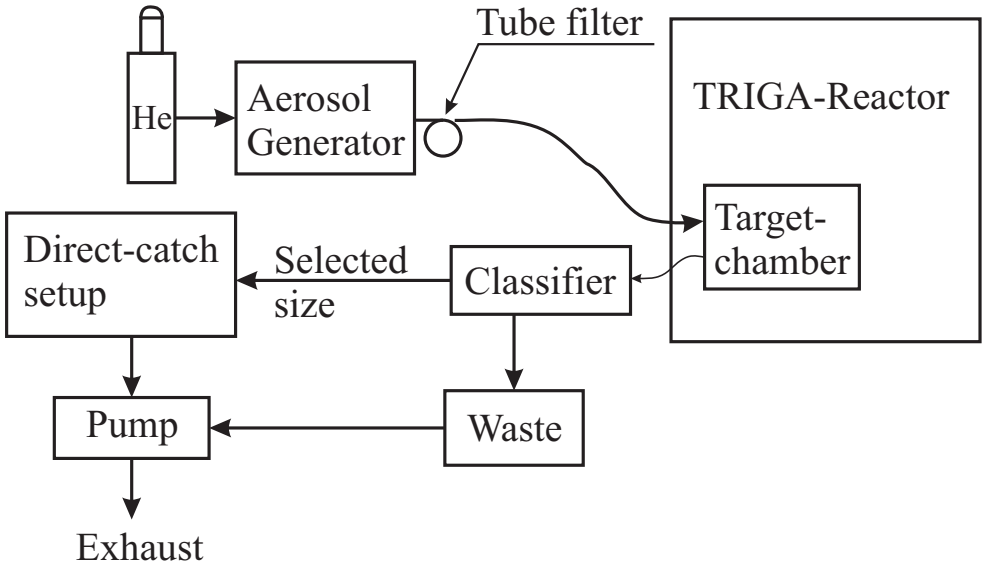

Figure 4.9: Sketch of the setup for the aerosol size selective activity measurement. Fission products attach to the aerosols in the target chamber and are guided to the particle classifier where one size interval is selected. Particles of the selected size are collected on a filter for later investigations whereas the others are guided to the waste.

of about 52 minutes for ^{101}Mo, which was considered to be too long due to limited online running time. It has been decided to extend the collection time only to 20 minutes while the time for decay and measurement remained two and five minutes, respectively. According to Eq. (4.6) about 60% of the maximum activity is reached within this time. Due to the very low expected activity the detector has been shielded with lead from the reactor radiation in order to decrease the background activity.
It is assumed that the number of transported fission products is proportional to the number of aerosols in the size interval selected by the classifier, which is valid until the saturation region is reached (see Sect. 4.2.2). Furthermore, it was observed in case of KCl aerosols that the number of attached fission products is proportional to the aerosol surface and thus to the square of their diameters [36] and proved by theoretical calculations as well [37]. The activity of the ^{101}Mo peak at $E_\gamma = 192\,\mathrm{keV}$ has been determined and is shown in Fig. 4.10.
In Fig. 4.10(a) the measured counts as function of the aerosol surface are presented assuming that the aerosols are spheres. The distribution of the activity is determined by the lognormal distribution of the aerosol quantity. Thus one has to account for the number of aerosols, which is done by the calculation of the average counts per aerosol particle for each surface interval as presented in Fig. 4.10(b). The presented values are the weighted mean of three measurements and the errors the weighted standard deviation. The errors in both figures are very large, which is due to the long measurement time and thus due to fluctuations and decrease of the transport efficiency, as will be discussed in Sect. 4.4. The errors in Fig. 4.10(b) are even larger as size distribution and activity cannot be recorded

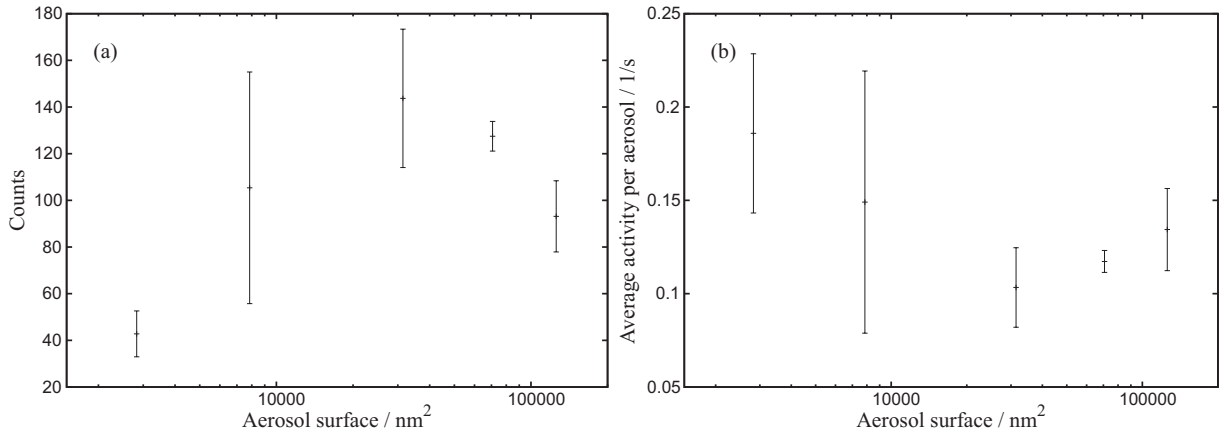

Figure 4.10: Counts (a) and average transported activity per aerosol (b) in dependency of the aerosol surface assuming that the aerosols are spheres. The activity is the area under the peak of ^{101}Mo at $E_\gamma = 192\,\mathrm{keV}$. With the fitted number of counts the presented values have been determined by calculation of the weighted mean and standard deviation of three measurements using identical parameters.

at the same time and the errors here indicate mechanical changes of the electrodes or large fluctuations of the discharge frequency. The presented information verifies the linear correlation between aerosol surface and transported fission products. Thus, a certain aerosol size interval can be selected if it will be investigated that the chemical bond cannot be released sufficiently for all intervals in the ECR ion source to increase the number of ionized radionuclides.

4.3 Measurement of the transport time

Long transportation times from the target chamber to the ion source decrease the possibility to access very short-lived radionuclides as they may decay before they can be investigated. To estimate the accessible half-life, the extraction time for the fission products has been studied. This can most easily be performed when the reactor is pulsed while aerosols are guided through the target chamber to the detector. During the pulse the reactor emits γ-radiation, which is detected by the germanium-lithium detector. Therefore, the experimental setup as shown in Fig. 4.1 has been chosen whereas the filter, on which the aerosols are collected, was mounted directly in front of the detector [67]. The detector had to be shielded with lead as it would otherwise become saturated during a reactor pulse. Due to this change in the setup the filter had not to be changed during the whole measurement. One representative measurement of the recorded activity as a function of time is shown in Fig. 4.11. The shape of the immediately emitted radiation by the reactor pulse can be approximated with a Gaussian distribution due to the time dependency of the neutron flux in the reactor. After a few hundred milliseconds the first fission products arrive and the intensity of the radiation increases a second time until no fission products arrive any

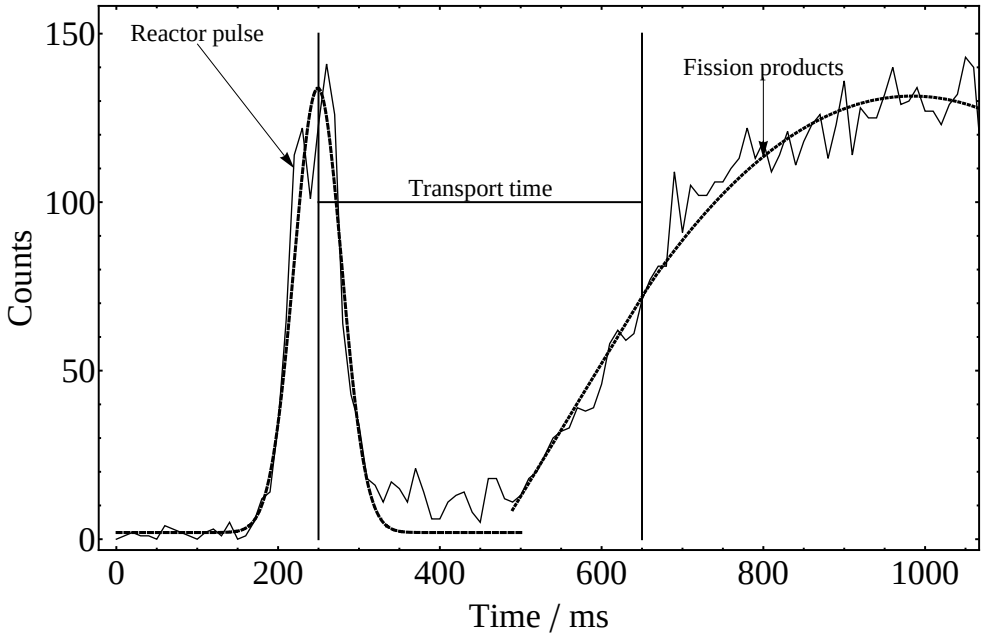

Figure 4.11: γ-radiation recorded during and after a reactor pulse. The first peak is related to radiation emitted from the reactor, the second increase of the radiation intensity is due to the deposition of fission products on the filter in front of the detector. The dashed line is a Gaussian fit to the pulse shape, the dotted line is a parabola fit to the increasing activity during the arrival of the fission products. For more details see text.

longer and the deposited fission products decay within about two minutes until their activity reaches the background level again. This is not shown as the measurement time could not be chosen so long with the necessary resolution. The start of the measurement $t = 0$ has been chosen arbitrarily as it does not effect the determination of the transport time.
It is well known that the shape of the pulse is not exactly a Gaussian distribution as the radiation is emitted by a great variety of radionuclides. But nevertheless it is also verified that the approximation is sufficient as can be seen from Fig. 4.11. It is more difficult to find an appropriate function to fit the second increase of activity.
An analytical solution of the differential equations, which describe the arrival and decay of the particles, is very complicated and contains too many degrees of freedom to calculate a fitting function to the data. According to the shape of the second rising edge at about $t = 500$ ms it seems to be appropriate to fit an empirical function, in this case a parabola, to the data to describe the arrival of the radionuclides on the filter:

$$A(t) = at^2 + bt + c \tag{4.7}$$

with a, b and c being fit parameters. Eq. (4.7) fits very well to the data as presented in Fig. 4.11, which is confirmed by a χ^2 value of 0.74.
After the determination of the functions describing the time evolution of the recorded radiation triggered by a reactor pulse, the transport time has been defined as the time

difference between the maximum of the activity of the reactor pulse and the time when the activity that is caused by the fission products reaches 50% of its maximum (see. Fig. 4.11). With this definition the transport time has been determined from four measurements to be

$$T_{\text{trans}} = 390 \pm 90\,\text{ms} \ , \tag{4.8}$$

which is less than the approximately 0.8 s that has been observed in other experiments [67]. This means that fission products with half-lives down to about 400 ms can be investigated if the overall efficiency is sufficiently high. Shorter-lived radionuclides can be detected as well if their production rate is high enough that a sufficient number of ions reaches the experiment before they decay. However, the transport time in Eq. (4.8) should be considered as an average transport time, since the first fission products arrive already after about 250 ms on the filter.

4.4 Measurement of the transport efficiency

Other crucial parameters, which limit investigations of radionuclides, are their production rates and transport efficiencies. The production rate of the radionuclides in thermal neutron induced fission of the available ^{235}U target under experimental conditions inside beam port A is shown in Fig. 4.3. It is determined by the target properties and the neutron flux for every radionuclide, while the transport efficiency of the fission products is determined by the properties of the gas-jet system.
The transport efficiency is determined relatively by the comparison of γ-lines at equal energies from a standard sample and samples of extracted fission products. Since the standard has to represent all available fission products, a 0.5 mm thick Teflon foil has been positioned directly in front of the target inside the target chamber. The thickness of the foil ensures the collection of all fission products that are in principle available for transportation. Afterwards the target chamber has been placed inside the reactor, irradiated for twenty minutes with a power of 10 kW_{th}, which is equal to a neutron flux of $9.8 \cdot 10^9 \frac{\text{n}}{\text{cm}^2\text{s}}$, and removed after an additional waiting time of 24 minutes. Subsequently the γ-spectrum has been measured and can be regarded as a standard measurement. After the removal of the Teflon foil the target chamber has been returned into the reactor and the helium including the carbon aerosols is guided through the target chamber and the capillary as in the previous measurements. Afterwards the aerosols with attached fission products were collected on a filter and the equal measurement cycle of 20 minutes collection, 24 minutes of waiting, and 15 minutes of detection has been used. Due to the equal experimental conditions the γ-spectra are comparable and the transport efficiency can be calculated by the comparison of the fitted areas of one γ-line with the associated one of the standard spectrum for all measurements.
In order to test the principle, the first three measurements have been done at 10 kW_{th} reactor power. An increase of the reactor power to 100 kW_{th}, which is directly proportional to the neutron flux, increases the number of fissions by a factor of ten as well as the number

Nuclide	Half-life	Mother nuclide	Half-life of mother nuclide
^{93}Sr	7.45 min	^{93}Rb	5.8 s
^{94}Y	18.7 min	^{94}Sr	74 s
^{95}Y	10.3 min	^{95}Sr	24.4 s
^{101}Mo	14.6 min	^{101}Nb	7.1 s
^{104}Tc	18.2 min	^{104}Mo	1.0 min

Table 4.3: Investigated fission products with a sufficient long half-life and short-lived mother nuclides. Values are taken from [90].

of fission products being available for transportation due to the isotropy of their emission. In order to increase statistics the irradiation power has been subsequently increased to 100 kW_{th}, which was not possible for the standard measurement due to radiation safety issues. As the production rate R is proportional to the number of fissionable atoms N_{fiss}, the fission cross section σ_n, and the neutron flux ϕ_n, described by

$$R = \phi_n \, \sigma_n \, N_{\text{fiss}} \quad , \tag{4.9}$$

the areas of the standard γ-lines can be multiplied with factor ten to be comparable with the other determined values. It is expected that the transport efficiency is equal for all different species besides the noble gases.
It is important to investigate only γ-lines of radionuclides with sufficient long half-lives and mother nuclides with a half-life of less than 2.4 min as after $10 \cdot T_{1/2}$ more than 99% of the nuclides are decayed. These parameters are very important as it has to be assured that all mother nuclides are decayed when the radiation measurement is started. Otherwise even short variations of collection, decay or detection time have a significant influence on the result due to the fast decay of the nuclide of interest and the decay of the mother nuclides into a nuclide of interest, respectively. On the other hand a too long half-life results in a small amount of decays, which would require longer detection times. Radionuclides with these properties, which could be identified in the spectrum, are listed in Tab. 4.3.
According to Sect. 3.3.7 the transport efficiency has been recorded for a capillary with an inner diameter of 0.86 mm and for one with an inner diameter of 1.4 mm. It is expected that the transport efficiency is almost constant for long time periods for the thicker capillary as the surface flow of the aerosols has been constant as shown in Fig. 3.14(c). The transport efficiency for the smaller capillary is expected to decrease during operation, as shown in Fig. 3.14(a), but as this capillary has been used several times before for gas jet extraction [36,67,85], its transport efficiency has been tested and compared to the efficiency of the thicker capillary. This comparison is anyhow necessary as it is not yet tested, at which gas pressures the ECR ion source can be operated.
The areas of the γ-lines under investigation have been determined by fitting a modified Gaussian distribution (see Eq. (4.1)) to the data. Afterwards the areas have been compared with the standard measurement and were plotted in dependency of the time. The time evolution of the transport efficiency has been examined for the five radionuclides listed in

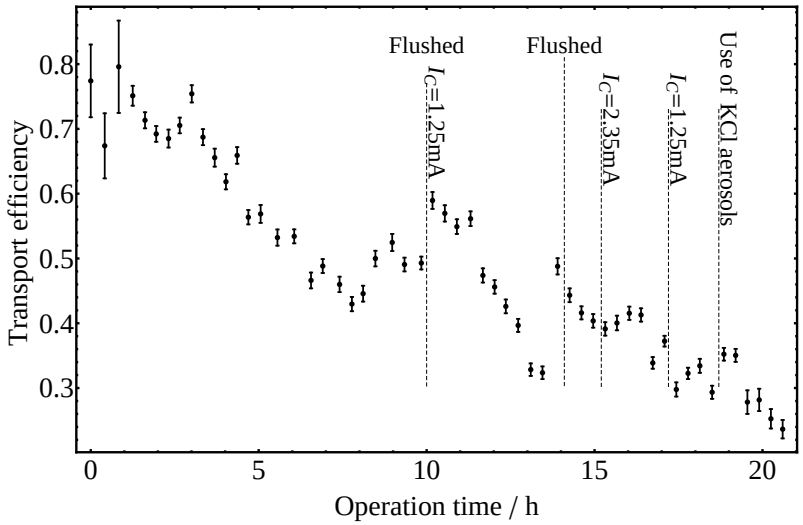

Figure 4.12: Transport efficiency of ^{104}Tc through a capillary with an inner diameter of 0.86 mm as a function of operation time. I_C is the capacitor loading current. Further details are given in the text.

Tab. 4.3. A representative measurement of ^{104}Tc is shown in Fig. 4.12 for a polyethylene capillary with an inner diameter of 0.86 mm recorded with a gas flow of 1.4 $\frac{\text{l}}{\text{min}}$ and a loading current of $I_C = 2.35\,\text{mA}$ at the beginning. Every time when a parameter was changed it is marked. For the first three hours the transport efficiency was measured to be about 70% and decreased in the following five hours down to about 50%. Since the decrease of the transport efficiency is most likely caused by deposited aerosols in the capillary and especially at its inlet, the capillary was flushed with clean helium and the loading current has been decreased to $I_C = 1.25\,\text{mA}$. Thereby the amount of aerosols, which attach to the walls, is expected to be reduced while the amount of transported fission products remains the same (see Sect. 4.2.2). At first an increase of the transport efficiency was observed after the decrease of the loading current, but as strong fluctuations are observed in the preceeding and following data points it is probably not correlated to the flushing of the system. Also flushing and variation of the loading current had no influence on the transport efficiency as can be seen in Fig. 4.12. In general the transport efficiency continued to decrease. The subsequent change of the aerosol material to potassium chloride did not show any difference as well. For the transport efficiencies of the other radionuclides a similar decreasing behaviour has been observed. The presented time evolution of the transport efficiency can be explained by the time dependency of the transported aerosols shown in Fig. 3.14(a) due to the similar behavior of the decrease of the surface flow in the first eight hours, with similar experimental conditions to the online experiment.
As already mentioned the transport efficiencies presented in Fig. 4.12 are calculated by the comparison of the fitted areas of the γ-lines of the radionuclides. Thus the error bars in Fig. 4.12 are determined by Gaussian error propagation. The errors of the first three values are very large. This is due to the fact that for the collection of aerosols with fis-

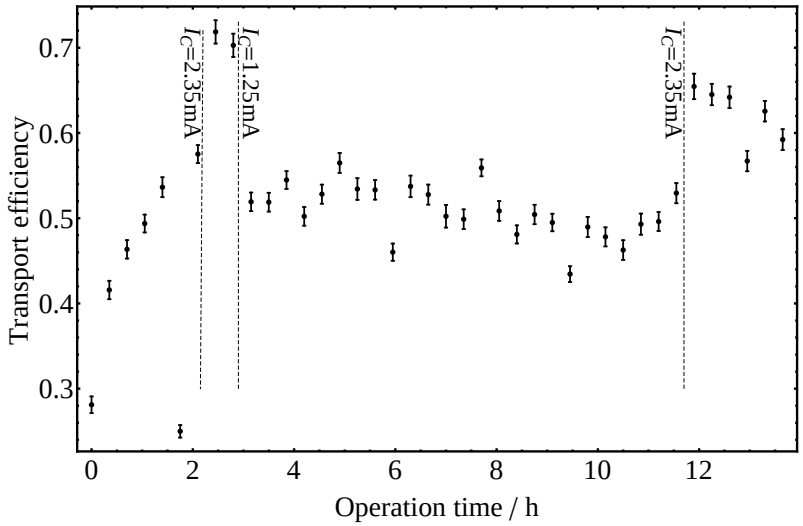

Figure 4.13: Transport efficiency of ^{104}Tc through a capillary with an inner diameter of 1.4 mm. In the first two hours the efficiency increases from less than 30% to about 60% and stays constant for about eight hours without maintenance. I_C is the capacitor loading current.

sion products the reactor has been operated at the beginning with a power of 10 kW_{th} to record spectra, which are directly comparable to the standard. Therefore the activity of the collected sample and the peak-to-background ratio are very low. It has been decided to operate the reactor in the following with 100 kW_{th} in order to improve statistics. The uncertainties of the last four values are larger than the others as well. This is due to an increase of the background radiation caused by ^{18}F from another experiment in the PET-Lab near beam port A.
Afterwards the capillary has been replaced by another polyethylene tube with an inner diameter of 1.4 mm. With this capillary it was expected that the transport efficiency stays constant for a longer time since previously the aerosol transport was stable for a longer time compared to the 0.86 mm capillary under similar experimental conditions (see Fig. 3.14). Due to the larger diameter a helium gas flow of about 7 $\frac{l}{min}$ is required to generate the thermalization pressure of 1.7 bar. A loading current of 1.25 mA has been used and the reactor has been operated at 100 kW_{th}. Other variations of parameters are indicated in the plot. The values of the transport efficiency of ^{104}Tc are exemplarily presented in Fig. 4.13. An increase of the transport efficiency has been observed during the first two hours from about 30% up to 60%. Subsequently, the loading current was shortly increased to 2.35 mA to demonstrate that it is in principle possible to increase the transport efficiency up to the values reached with the smaller capillary before. With I_C = 1.25 mA the transport efficiency was constant over a long time period of about 8 hours, which is in agreement with Fig. 3.14(c). After a total operation time of about 11.5 hours the loading current has been increased again to 2.35 mA and an increase of the efficiency has been observed followed by a slow decrease. This important measurement shows that it is possible to transport fission

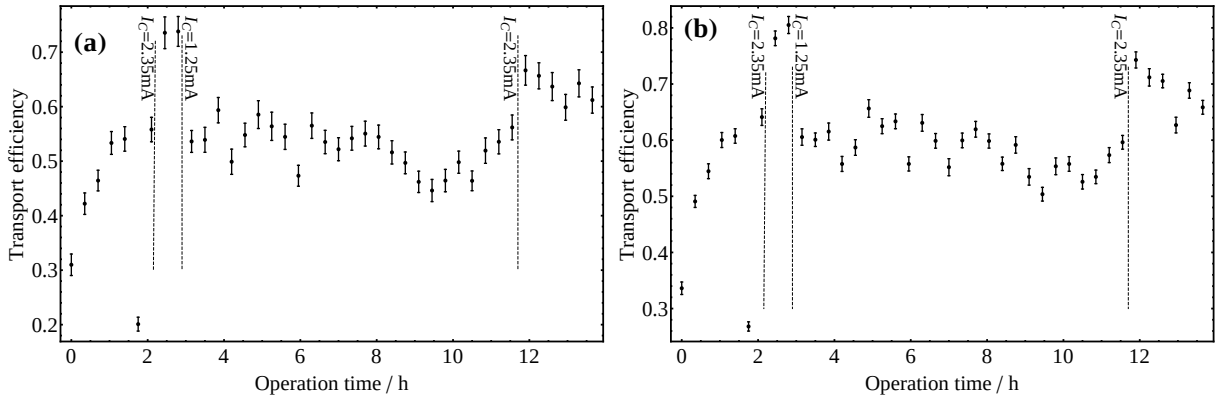

Figure 4.14: Transport efficiency of ^{101}Mo (a) and ^{94}Y (b) through a capillary with an inner diameter of 1.4 mm. The observed time evolution is similar to the one observed for ^{104}Tc.

products with a constant efficiency of $(51 \pm 3)\,\%$ for several hours. Due to the observed increase for higher loading currents it is possible to compensate decreases and keep the efficiency constant for even longer times.

It was expected that the transport efficiency is similar for all radionuclides besides noble gases. This has been tested by the comparison of the transport efficiencies of all nuclides mentioned in Tab. 4.3. For comparison the transport efficiency as a function of time is shown for ^{101}Mo and ^{94}Y in Fig. 4.14. It has been observed that the qualitative behavior of the time evolution is similar to the one of ^{104}Tc, only the absolute efficiency is different (see Tab. 4.4). For the examination of the transport efficiencies of other fission products it is necessary to make a faster standard measurement.

This result shows that the transport of the extracted fission products is qualitatively similar, whereas the absolute values deviate. Furthermore it has been shown that the gas-jet system can be operated with a constant transport efficiency of about 50% for at least eight hours of operation, which is necessary for a constant ion production. Also small changes can be compensated with an increase of the number of aerosols and therefore the loading current. The stability of the gas-jet system is good enough to enable investigations on nuclides with low yields, which require continuous production for several hours.

Nuclide	Average transport efficiency / %
^{93}Sr	68 ± 4
^{94}Y	58 ± 4
^{95}Y	72 ± 7
^{101}Mo	53 ± 4
^{104}Tc	51 ± 3

Table 4.4: Average transport efficiency of the investigated nuclides .

4.5 Determination of the absolute transport rate

For later experiments on radionuclides provided from the reactor with the TRIGA-SPEC facility it is important to know how many particles will finally be available after extraction. Besides the fission yields this number is mainly determined by the overall transport efficiency of the setup, including the efficiency of the helium gas jet, the ionization efficiency of the ECR ion source, the efficiency of the subsequent ion transport to the experiments, and their detection efficiency.
For the determination of the absolute number of transported particles behind the gas-jet system, the germanium-lithium detector has to be calibrated as the efficiency of the γ-detection is characteristic for each device. Therefore, a filter of the type that has been used for aerosol collection has been prepared. A fluid activity standard containing several long-lived radionuclides, whose decay energies cover the whole detection range from 60 keV up to 1836 keV, has been used. To this end 80 μl of the activity standard have been deposited on the filter in a circular shape to imitate the area covered by the aerosols during collection and subsequently the γ-spectra were recorded for three times 24 hours. Due to the necessary efficiency calculation the data was evaluated with the radiation acquisition and analysis software Genie$^{\text{TM}}$2000 [92]. Since the activity of the nuclides in the activity standard is well-known at its creation time, it is possible to correct the activity of the standard due to the half-life of the contained radionuclides and to calculate the efficiency of the detector as a function of the energy of the detected radiation. The calibration procedure was performed for the detector used in the measurements described below.
With the calibrated detector it was possible to determine the absolute number of particles that are transported per unit time through the capillary. Therefore the measured activity of one γ-line was corrected for the decay losses during the decay and measurement time as well as due to the relative occurrence of the emitted radiation. In addition, the data was corrected for the dead time of the detector. The determination of the absolute transport rate requires the solution of Eq. (4.6). With the number of particles $N = \frac{A\,T_{1/2}}{\ln 2}$ the transport rate k can be calculated as:

$$k = A\left(1 - e^{-\ln 2 \frac{T_{1/2}}{T_{\text{coll}}}}\right) \quad . \tag{4.10}$$

$T_{1/2}$ denotes the half-life of the considered nuclide and A its activity after the collection at the time T_{coll}. As shown in Fig. 4.13 the transport efficiency is not constant for the whole observation time due to the change of gas-jet parameters. Thus, the absolute numbers of transported particles have been calculated from the time period of constant transport efficiency. Due to the long waiting time of 24 minutes this value is a cumulative transport rate, which includes also all nuclides produced by the decay of the mother nuclides. Assuming that the mother nuclides are all transported with the same efficiency, the individual transport rate can be determined by the multiplication with the factor $k^{\text{ind}}_{\text{prod}}/k^{\text{cum}}_{\text{prod}}$ with the values taken from [22, 23]. Here $k^{\text{ind}}_{\text{prod}}$ denotes the individual and $k^{\text{cum}}_{\text{prod}}$ the cumulative production rate of the considered nuclide. To increase statistics the weighted mean of 15 measurements has been taken. The values $k^{\text{ind}}_{\text{trans}}$ presented in Tab. 4.5 are the numbers

of the considered radionuclides that exit the capillary and are available in the skimmer region.
It was indicated in Fig. 4.3 that the individual production rate of the fission products increases up to 10^6 per second, which rises the question why the absolute number of detected particles is about two orders of magnitude smaller although the transport efficiency has been measured to be more than 50%. Therefore the geometry of the target has to be considered. As the fission products are emitted in a 4π angle the sketch of the target chamber in Fig. 4.2(a) indicates that 50% of the fission products are transmitted in the wrong direction and are absorbed by the wall of the target holder. In addition the target is surrounded by a 1 mm high edge of the target holder, which decreases the amount of available fission products as well. As the target is not pointshaped the fraction of produced fission products that are available for transport has been simulated by particle propagation simulations. Therefore it has been assumed that they are completely absorbed by the edge of the capillary holder and that their trajectory is straight. In several simulations it has been determined that 41.4(1)% of the produced fission products enter the thermalization region for a cylindrical target. The fraction is the mean value of 100 simulations each with $2 \cdot 10^9$ simulated particles with the error being the standard deviation. The target material has been assumed to be distributed on an area with the same diameter as the opening of the target holder - 20 mm, which increases the error as the diameter is a little bit smaller and the shape is not exactly circular. Thus the fraction has been determined to be $(42 \pm 2)\%$.
In addition the 13 μm thick aluminum foil that covered the target has been considered. In the mass range of the detected fission products only 3% to 6% are transmitted through the foil [86]. This fraction has been considered to be approximately a linear function of the atomic mass in the small range between $A = 93$ and $A = 104$ as only a little amount of experimental transmission data is available [86]. $k_{\text{trans}}^{\text{cum}}$ denotes the cumulative transport rate of radionuclides presented in Tab. 4.5, σ_{geo} respects the reduction of the transmission due to geometry and σ_{foil} is the absorption factor of the aluminum foil. k_{prod} denotes the production rate calculated from the relative fission yield [22, 23], target properties and neutron flux, whereas here the cumulative fission yield has been considered since during the waiting time all mother nuclides have been decayed. With the consideration of these

Nuclide	$k_{\text{prod}}^{\text{cum}}$ / 10^5/s	$k_{\text{prod}}^{\text{ind}}$ / 10^5/s	$k_{\text{trans}}^{\text{cum}}$ / 10^3/s	$k_{\text{trans}}^{\text{ind}}$ / 10^3/s
^{93}Sr	28.5	11.7	40.6 ± 6.0	16.7 ± 2.5
^{94}Y	29.4	1.78	15.3 ± 1.1	0.9 ± 0.1
^{95}Y	29.1	5.11	26.9 ± 5.0	5.2 ± 1.0
^{101}Mo	23.6	0.85	21.6 ± 1.8	0.8 ± 0.2
^{104}Tc	8.6	0.42	4.1 ± 0.4	0.2 ± 0.1

Table 4.5: Measured transport rates of the observed radionuclides. The cumulative transport rate includes all mother nuclides.

Nuclide	k_{prod} / 10^6/s	σ_{foil} / %	R_{trans} / %
^{93}Sr	2.85	5.0 ± 1.2	66±19
^{94}Y	2.94	4.8 ± 1.2	25±7
^{95}Y	2.91	4.6 ± 1.3	47±16
^{101}Mo	2.36	3.3 ± 1.3	66±26
^{104}Tc	0.86	2.6 ± 1.3	43±22

Table 4.6: Transport efficiency calculated from the absolute transport rate. k_{prod} denotes the cumulative production rate calculated from the relative fission yield [22, 23]

parameters the transport efficiency R_{trans} can be calculated:

$$R_{\text{trans}} = \frac{k_{\text{trans}}^{\text{cum}}}{k_{\text{prod}} \cdot \sigma_{\text{geo}} \cdot \sigma_{\text{foil}}} \quad . \tag{4.11}$$

The resulting transport efficiencies are presented in Tab. 4.6. In comparison with Tab. 4.4 three values are equal within the given uncertainties and only the transport efficiency of ^{94}Y differs significantly. The large errors for the transport efficiency shown in Tab. 4.6 are due to the fact that the uncertainty of the transmission through the aluminum foil and of the absolute transport rate as well as the assumption that the target has a circular shape increase the uncertainty significantly. On the other hand the direct comparison of the spectra contains no assumptions as the uncertainties are only statistical errors. By collecting the fission products directly after leaving the target it is possible to determine the denominator in Eq. (4.11) more precisely than by calculating it with the available literature data. Thus, the absolute transport rates have been verified.
Considering Eq. (4.11) the transport rate can be increased by a factor of 20-40 (see Tab. 4.6) by removing the aluminum foil that covers the target. As this foil prevents the heavy fission products to leave the target this will be anyhow necessary for investigations in this mass region. In contrast, the foil prevents the setup to be contaminated with long-lived fission products. Thus, it is better to perform first tests with the covered target as mechanical work may be necessary on skimmer and ECR ion source, which would require for an uncovered target a huge effort due to radiation safety issues. The number of available fission products can be increased as well by increasing the amount of fissionable material, which increases the production rate. In addition it is possible to use another material with a higher fission cross section. Hence, a ^{235}U target and the available 300 μg ^{249}Cf target are considered. Based on the maximum diameter of the target, which is about 2 cm, the maximum uranium density of about 0.8 mg/cm^2, and the determined transport efficiency in Tab. 4.4, a prediction of the transport rate is made for an uncovered 2.5 mg ^{235}U target. Based on the determined transport efficiency a prediction of the transport rate is made for the available ^{249}Cf target as well. The results are listed in Tab. 4.7. In comparison with the production of fission products from the californium target it is clear that the number of available particles depends as well on the choice of the target material. This shows that it is possible to achieve transport rates in the range of $(10^5 - 10^6)\,\text{s}^{-1}$ as an upper limit with uranium, whereas the low production rates between the fission yield maxima can be

Nuclide	$k_{\text{prod}}^{\text{ind}}(^{235}\text{U})$ / 10^6/s	$k_{\text{trans}}^{\text{predicted}}(^{235}\text{U})$ / 10^5/s	$k_{\text{prod}}^{\text{ind}}(^{249}\text{Cf})$ / 10^5/s	$k_{\text{trans}}^{\text{predicted}}(^{249}\text{Cf})$ / 10^5/s
^{93}Sr	17.4	50.1±4.0	10.6	3.1 ± 0.2
^{94}Y	2.5	6.4±0.6	4.0	1.0 ± 0.1
^{95}Y	7.5	22.8±2.5	13.5	3.9 ± 0.4
^{101}Mo	1.2	2.8±0.2	9.6	2.1 ± 0.2
^{104}Tc	0.6	1.3±0.2	15.6	3.3 ± 0.3

Table 4.7: Predicted transport rate for an uncovered 2.5 mg ^{235}U and the available 300 μg ^{249}Cf target based on the results presented in the text. The prediction is based on the transport efficiency shown in Tab. 4.4 and the calculation of the production rates from target and the neutron flux in beam port B.

compensated using a californium target due to the shift of the lower maximum to higher masses, as it is shown in Fig. 2.3. To reach higher rates with uranium a new target chamber has to be designed for the usage of a larger target. A larger californium target can most likely not be prepared since the material is not available and very expensive.
With the calibration of the γ-detector it was possible to determine absolute transport rates of the gas-jet system for the long-lived nuclides ^{93}Sr, ^{94,95}Y, ^{101}Mo and ^{104}Tc. For these nuclides transport rates from $2 \cdot 10^2\,\text{s}^{-1}$ (^{104}Tc) up to $1.7 \cdot 10^4\,\text{s}^{-1}$ (^{93}Sr) have been reached and can be fed into the ion source. As a maximum for a new uncovered target transport rates from $1.3 \cdot 10^5\,\text{s}^{-1}$ (^{104}Tc) up to $5 \cdot 10^6\,\text{s}^{-1}$ (^{93}Sr) are predicted. An increase of the numbers of available particles is possible by using more fissionable material or by using the californium target depending on the wanted ion species.
Depending on the element, ionization efficiencies between 40% (sulfur) and 90% (noble gases) are expected for the ECR ion source [93]. However, that still needs to be confirmed after installation and operation of the ion source. Thus, it is apparently possible to perform mass measurement of the frequently produced fission products with the covered target using the TOF-ICR technique, whereas FT-ICR measurements are most likely only limited by the half-life of the particles. Due to the fast decrease of the production rate apart the maximum it is necessary to use an uncovered target with more fissionable material for studies of rarely produced nuclides. Since for collinear laser spectroscopy studies transport rates of about $10^5\,\text{s}^{-1}$ without an RFQ are needed, it depends on the efficiency of the ECR ion source whether a new target has to be prepared.

Chapter 5

Summary and Outlook

Nuclear models aim for the description of known and the prediction of unknown nuclear properties. Thus, experimental investigations of radionuclides far away from the valley of stability are necessary for the test and the improvement of these models. Investigations of neutron-induced fission products push the border of direct measurements further into the neutron-rich area of the nuclear chart. Direct measurements of nuclear ground-state properties of these nuclides are the main goals of the TRIGA-SPEC facility, which consists of the double Penning trap mass spectrometer TRIGA-TRAP and the collinear laser spectroscopy beamline TRIGA-LASER. The nuclides are produced by thermal neutron induced fission of a fissionable target placed inside the research reactor TRIGA Mainz. For the extraction a helium gas-jet containing carbon aerosols needed as transport medium has been developed and aerosol production as well as transport properties have been characterized within this thesis.
It has been verified in agreement with theory [80] and previous experiments [36,84] that the size of the aerosols is lognormally distributed. In a number of measurements it has been investigated how their mean size can be varied under experimental conditions. Within this thesis it has been demonstrated for the first time at TRIGA Mainz that fission products can be transported with the gas-jet recoil-transport method using carbon aerosols. Some of the extracted fission products have been identified by means of γ-spectroscopy as the nuclides ^{84}Se, ^{93}Sr, ^{94,95}Y, $^{103-105}$Mo and ^{104,105}Tc. These are the nuclides with the highest production rate having the required properties to be detected with the method used within this thesis. The transport time of the radionuclides is a limiting factor for online investigations due to their half-life and the finite measurement time. Thus, it is required to determine the transport time of the fission products as it marks the limit of observable radionuclides at a given production rate and transport efficiency. The extraction time of fission products has been determined to (390 ± 90) ms.
An efficient transport is important as well for investigations of rarely produced nuclides. Thus, the efficiency of the transport out of the target chamber through the capillary has been recorded for some of the detected fission products and it has been demonstrated that values up to 80% can be reached. It has been clearly demonstrated by the efficiency measurement that it is possible to operate the gas-jet with a constant efficiency of more

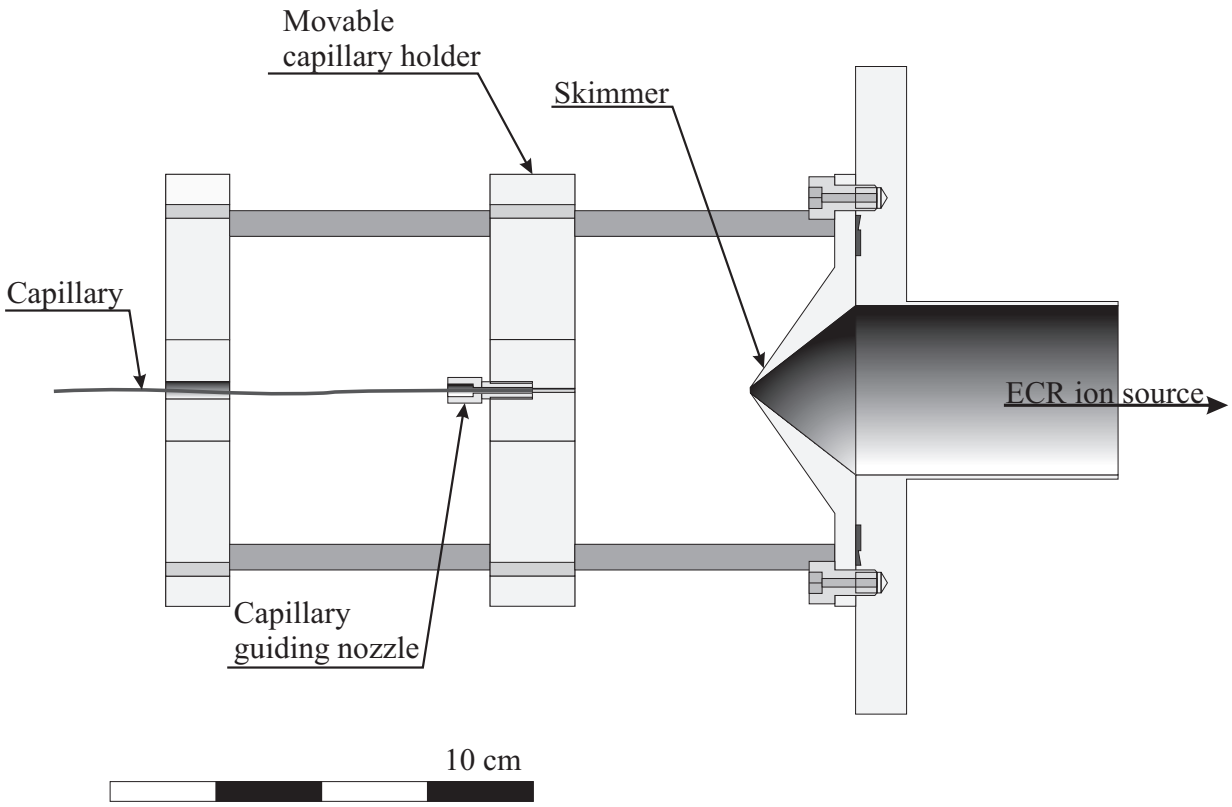

Figure 5.1: Detailed drawing of the skimmer system. The nozzle in the movable capillary holder ensures the alignment of capillary and skimmer, which is required for ideal aerosol transmission to the ECR ion source.

than 50% for at least eight hours, which is a very important result as data collection in a typical experiment is up to a few hours. In addition the absolute transport rate was determined for the radionuclides observed during a period of constant efficiency. Rates from $(2 \pm 1)10^2\, s^{-1}$ for ^{104}Tc up to $(16.7 \pm 2.5)10^3\, s^{-1}$ for ^{93}Sr have been measured with a $300\,\mu$g target ^{235}U covered with a $13\,\mu$m thick aluminum foil.
This target has been used for all experiments within this thesis, whereas ^{239}Pu and ^{249}Cf targets are also available. This offers the opportunity to investigate very rarely produced fission products as the production rates can be increased by using the other targets instead of ^{235}U due to their higher thermal-neutron fission cross sections and different fission yields. Especially the determination of the transport time and the transport efficiency were big steps forward since it is now clearly known, which numbers of particles per unit time can be expected for the different fission products after the calculation of their production rates, and it can be estimated down to which half-life it will be possible to perform mass spectrometric and laser spectroscopic measurements.
The next step will be the preparation of a target with more material that will be in addition used uncovered to gain higher transport rates. The use of helium as carrier gas requires the target to be covered with a thin aluminum foil as the pressure inside the target chamber

can not be increased until the particles emitted by the uncovered target are thermalized. Thus, for investigations of the heavy fission products it is necessary to use argon or nitrogen as carrier gas as the mean free path of a particle is smaller than in helium. In preparation for these investigations it is necessary to measure the transport time since the maximum laminar velocity in a gas depends on its sonic speed. Due to the longer transport time in argon and nitrogen it is also necessary to determine the transport efficiency for this gases. After the extraction the aerosols have to be guided into the ion source region for ionization. When carrier gas and aerosols exit the capillary into a region of lower pressure the gas expands turbulently with the so-called zone of silence, a region without turbulences, in the center. As the aerosols are very heavy compared to helium they exit the capillary in the center of the beam. For the separation of helium and aerosols a skimmer is placed inside the expanding gas with its tip inside the zone of silence and its hole aligned to the exit of the capillary [38, 94]. While the aerosols pass the skimmer inside the laminar flow region the helium is pumped away by a roots pump. A skimmer has been designed [41] to transmit the aerosols into the ECR-ion source and to remove the helium without reflections into the aerosol beam simultaneously. In Fig. 5.1 a sketch of the skimmer is presented. A certain optimal angle of the outer wall of the skimmer has been found in empirical investigations [94], whereas its opening in the tip must have at least the same diameter as the capillary outlet for efficient aerosol transmission. A larger hole increases the transmission of aerosols and thus also the pressure inside the ion source. Therefore it has to be tested, up to which pressure efficient ionization is possible.
The next steps for the online coupling of TRIGA-SPEC to the reactor are offline tests with the skimmer system to investigate its properties for a sufficient high transmission with a sufficient low pressure inside the ECR ion source. The transmission can be tested with sodium aerosols, which are guided through the skimmer system and subsequently collected on a filter with the simultaneous determination of the pressure inside the ion source. The amount of sodium on the filter can be investigated with neutron activation analysis, which requires the irradiation of the filter with the aerosols inside the reactor and a subsequent analysis of the emitted γ-radiation. Then a plasma has to be created inside the ECR ion source, which requires a reflection free guide of the microwave from the magnetron into the plasma chamber where the fission products will be separated from the aerosols. Therefore it is important to know the maximum operation pressure to create singly charged ions inside the plasma. Furthermore, the magnetic mass separator will be included in the setup in order to mass separate the ions of interest from the unwanted species. Here a resolving power of a few hundred is foreseen at a transport energy of 30 keV. Finally the mass separated beam will be electrostatically guided through a switchyard to the two experimental beamlines. For the TRIGA-TRAP experiment the ion beam has to be bunched and the energy has to be lowered to a few hundred eV, which will be done by a pulsed drift tube. First tests will be performed with the already mentioned covered ^{235}U target. Thus, the first radionuclides that will be investigated online are the already detected ^{84}Se, ^{93}Sr, ^{94,95}Y, $^{101-105}$Mo and ^{104,105}Tc and other zirconium, strontium, niobium and yttrium isotopes with high production rates.

Bibliography

[1] G. Audi, A. Wapstra, C. Thibault, *The AME2003 Atomic Mass Evaluation (II). Tables, Graphs and References*, Nucl. Phys. A **729**, 337 (2003).

[2] H. Schatz, K. Blaum, *Nuclear masses and the origin of the elements*, Europhys. News **37**, 16 (2006).

[3] K. Blaum, *High-accuracy mass spectrometry with stored ions*, Phys. Rep. **425**, 1 (2006).

[4] J. Ketelaer, et al., *TRIGA-SPEC: A setup for mass spectrometry and laser spectroscopy at the research reactor TRIGA Mainz*, Nucl. Instrum. Meth. A **594**, 162 (2008).

[5] H.-J. Kluge, W. Nörtershäuser, *Lasers for nuclear physics*, Spectrochim. Acta B **58**, 1031 (2003).

[6] E. Stender, et al., Use of Alkali Halide Clusters in a Gas-Jet Recoil-Transport System, Radiochem. Radioanal. Lett. **42**, 291 (1980).

[7] I. Tanihata, *Radioactive beam science, past, present and future*, Nucl. Instrum. Meth. B **266**, 4067 (2008).

[8] G. Münzenberg, et al., *The velocity filter SHIP, a separator of unslowed heavy ion fusion products*, Nucl. Instr. Meth. **161**, 65 (1979).

[9] E. Kugler, *The ISOLDE facility*, Hyperfine Interact. **129**, 23 (2000).

[10] J. Äystö, *Development and applications of the IGISOL technique*, Nucl. Phys. A **693**, 477 (2001).

[11] H. Grunder, *Radioactive nuclear beam facilities in North America: Status and outlook*, Nucl. Phys. A **701**, 43 (2002).

[12] P. Bricault, et al., *TRIUMF-ISAC target station and mass separator commissioning*, Nucl. Phys. A **701**, 49 (2002).

[13] H. Geissel, et al., *The GSI projectile fragment separator (FRS): a versatile magnetic system for relativistic heavy ions*, Nucl. Instrum. Meth. B **70**, 286 (1992).

[14] E. Hyde, I. Perlman, G. Seaborg, *The nuclear properties of the heavy elements*, Prentice-Hall Englewood Cliffs, NJ (1964).

[15] G. Savard, et al., *Radioactive beams from gas catchers: The CARIBU facility*, Nucl. Instrum. Meth. B **266**, 4086 (2008).

[16] J. Duflo, A. Zuker, *Microscopic mass formulas*, Phys. Rev. C **52**, R23 (1995).

[17] D. Lunney, J. M. Pearson, C. Thibault, *Recent trends in the determination of nuclear masses*, Rev. Mod. Phys. **75**, 1021 (2003).

[18] C. Weizsäcker, *Zur Theorie der Kernmassen*, Z. Phys. A **96**, 431 (1935).

[19] N. Bohr, J. Wheeler, *The mechanism of nuclear fission*, Phys. Rev. **56**, 426 (1939).

[20] V. Strutinsky, *Shell effects in nuclear masses and deformation energies*, Nucl. Phys. A **95**, 420 (1967).

[21] J. Nix, *Calculation of fission barriers for heavy and superheavy nuclei*, Annu. Rev. Nucl. Sci. **22**, 65 (1972).

[22] T. England, B. Rider, *Evaluation and compilation of fission product yields 1993*, *Tech. rep.*, Los Alamos National Lab. (1994).

[23] http://ie.lbl.gov/fission.html.

[24] J. Magill, J. Galy, G. Pfennig, *Karlsruher Nuklidkarte*, Haberbeck (2006).

[25] K. Lieser, *Einführung in die Kernchemie*, VCH (1991).

[26] G. Friedlander, *Nuclear and radiochemistry*, John Wiley & Sons (1981).

[27] H. Newson, *Symmetric and Asymmetric Fission*, Phys. Rev. **122**, 1224 (1961).

[28] D. Fouquet, J. Razvi, W. Whittemore, TRIGA research reactors: A pathway to the peaceful applications of nuclear energy, Nucl. News **46**, 46 (2003).

[29] H. Menke, N. Trautmann, W. Krebs, Irradiations by means of reactor pulses, Kerntechnik **3**, 281 (1975).

[30] K. Eberhardt, A. Kronenberg, The research reactor TRIGA Mainz: A neutron source for versatile applications in research and education, Kerntechnik **65**, 269 (2000).

[31] R. Macfarlane, R. Gough, N. Oakey, D. Torgerson, *The helium-jet recoil transport method*, Nucl. Instr. Meth. **73**, 285 (1969).

[32] H. Bethe, J. Ashkin, *Experimental nuclear physics*, Wiley New York (1933).

[33] F. Zude, *Transportverhalten von Spaltprodukten in Gasjetsystemen*, Diploma thesis, Johannes Gutenberg-Universität Mainz (1986).

[34] J. Äystö, K. Valli, *Transport efficiency of the helium-jet recoil-transport method with pure helium*, Nucl. Instr. Meth. **3**, 531 (1973).

[35] H. Wollnik, *Principles behind a He-jet system and its application for isotope separation*, Nucl. Instr. Meth. **139**, 311 (1976).

[36] R. Günther, *Charakterisierung der Eigenschaften der KCl-Aerosolpartikel eines He-Gasjets*, Diploma thesis, Johannes Gutenberg-Universität Mainz (1993).

[37] W. Ho, P. Hopke, J. Stukel, *The attachment of RaA (Po-218) to monodisperse aerosols*, Atmos. Environ. **16**, 825 (1982).

[38] G. Scoles, D. Bassi, U. Buck, D. Laine, C. Braun, *Atomic and Molecular Beam Methods, Vol. I*, Oxford University Press, Oxford (1989).

[39] C. Smorra, A Carbon cluster laser ion source for TRIGA-TRAP, J. Phys. B **accepted** (2009).

[40] R. Geller, *Electron cyclotron resonance ion sources and ECR plasmas*, Institute of Physics Publishing (1996).

[41] C. Smorra, *Setup of an online ion source for the TRIGA-SPEC facility and online mass measurements on neutron-rich fission products*, Ph.D. thesis, Ruprecht-Karls-Universität Heidelberg (in preparation).

[42] F. Herfurth, et al., *A linear radiofrequency ion trap for accumulation, bunching, and emittance improvement of radioactive ion beams*, Nucl. Instrum. Meth. A **469**, 254 (2001).

[43] http://www.gsi.de/fair/.

[44] http://www.gsi.de/forschung/ap/projects/shiptrap/.

[45] R. Neugart, *Laser spectroscopy on mass-separated radioactive beams*, Nucl. Instr. Meth. **186**, 165 (1981).

[46] E. Otten, *Nuclear radii and moments of unstable isotopes*, Springer, New York (1989).

[47] A. Nieminen, et al., *On-Line Ion Cooling and Bunching for Collinear Laser Spectroscopy*, Phys. Rev. Lett. **88**, 094801 (2002).

[48] P. Lievens, et al., *Very high sensitivity in collinear laser spectroscopy: resonance detection by particle counting techniques*, Nucl. Instrum. Meth. B **70**, 532 (1992).

[49] E. Arnold, et al., *Nuclear spin and magnetic moment of* ^{11}Li, Phys. Lett. B **197**, 311 (1987).

[50] R. Neugart, et al., *Precision Measurement of* ^{11}Li *Moments: Influence of Halo Neutrons on the* ^{9}Li *Core*, Phys. Rev. Lett. **101**, 132502 (2008).

[51] H. Frånberg, et al., *Off-line commissioning of the ISOLDE cooler*, Nucl. Instrum. Meth. B **266**, 4502 (2008).

[52] L. Brown, G. Gabrielse, *Geonium theory: Physics of a single electron or ion in a Penning trap*, Rev. Mod. Phys. **58**, 233 (1986).

[53] J. Repp, *Setup of a non-destructive ion detection system and magnetic field investigations for precision mass measurements at TRIGA-TRAP*, Diploma thesis, Johannes Gutenberg-Universität Mainz (2008).

[54] G. Savard, et al., *A new cooling technique for heavy ions in a Penning trap*, Phys. Lett. A **158**, 247 (1991).

[55] D. Neidherr, et al., *Measurement and simulation of the pressure ratio between the two traps of double Penning trap mass spectrometers*, Nucl. Instrum. Meth. B **266**, 4556 (2008).

[56] K. Knuth, *Aufbau eines breitbandigen FT-ICR-Nachweissystems für TRIGA-TRAP*, Diploma thesis, Johannes Gutenberg-Universität Mainz (in preparation).

[57] L. Schweikhard, Theory of quadrupole detection fourier transform-ion cyclotron resonance, Int. J. Mass Spectrom. Ion Processes **107**, 281 (1991).

[58] S. Stahl, *Aufbau eines Experimentes zur Bestimmung elektronischer g-Faktoren einzelner wasserstoffähnlicher Ionen*, Ph.D. thesis, Johannes Gutenberg-Universität Mainz (1998).

[59] M. König, G. Bollen, H.-J. Kluge, T. Otto, J. Szerypo, *Quadrupole excitation of stored ion motion at the true cyclotron frequency*, Int. J. Mass Spectrom. Ion Processes **142**, 95 (1995).

[60] S. George, et al., *The Ramsey method in high-precision mass spectrometry with Penning traps: Experimental results*, Int. J. Mass Spectrom. **264**, 110 (2007).

[61] M. Kretzschmar, *The Ramsey method in high-precision mass spectrometry with Penning traps: Theoretical foundations*, Int. J. Mass Spectrom. **264**, 122 (2007).

[62] M. Marie-Jeanne, et al., *Towards a magnetic field stabilization at ISOLTRAP for high-accuracy mass measurements on exotic nuclides*, Nucl. Instrum. Meth. A **587**, 464 (2008).

[63] D. Beck, et al., *Electric and magnetic field optimization procedure for Penning trap mass spectrometers*, Nucl. Instrum. Meth. A **598**, 635 (2009).

[64] M. Smith, et al., *First Penning-trap mass measurement in the millisecond half-life range: the halo nucleus* ^{11}Li, Phys. Rev. Lett. **101**, 202501 (2008).

[65] A. Marshall, C. Hendrickson, G. Jackson, *Fourier transform ion cyclotron resonance mass spectrometry: a primer*, Mass Spectrom. Rev. **17**, 1 (1998).

[66] J. Ketelaer, *Developement of a non-destructive Fourier Transform-Ion Cyclotron Resonance detection system for singly charged ions in a cryogenicning trap*, Diploma thesis, Johannes Gutenberg-Universität Mainz (2006).

[67] A. Mazumdar, H. Wagner, G. Kromer, W. Walcher, *The on-line isotope separation facility helios at the mainz reactor*, Nucl. Instr. Meth. **174**, 183 (1980).

[68] H. Horvath, M. Gangl, *A low-voltage spark generator for production of carbon particles*, J. Aerosol Sci. **34**, 1581 (2003).

[69] N. Fuchs, *On the stationary charge distribution on aerosol particles in a bipolar ionic atmosphere*, Pure Appl. Geophys. **56**, 185 (1963).

[70] A. Hussin, H. Scheibel, K. Becker, J. Porstendörfer, *Bipolar diffusion charging of aerosol particles. I: Experimental results within the diameter range 4-30 nm*, J. Aerosol Sci. **14**, 671 (1983).

[71] TSI, *Models 3077/3077A Aerosol Neutralizers*, TSI Incorporated (2003).

[72] S. Wang, R. Flagan, *Scanning electrical mobility spectrometer*, Aerosol Sci. Technol. **13**, 230 (1990).

[73] H. Butt, K. Graf, M. Kappl, *Physics and chemistry of interfaces*, Wiley-Vch Weinheim (2003).

[74] K. Lee, H. Chen, J. Gieseke, *Log-normally preserving size distribution for Brownian coagulation in the free-molecule regime*, Aerosol Sci. Technol. **3**, 53 (1984).

[75] E. Limpert, W. Stahel, M. Abbt, *Log-normal Distributions across the Sciences: Keys and Clues*, BioScience **51**, 341 (2001).

[76] M. Smoluchowski, Attempt of a mathematical theory for the kinetics of coagulation of colloid solutions, Z. Phys. Chem. **92**, 129 (1917).

[77] I. Lifshitz, V. Slyozov, *The kinetics of precipitation from supersaturated solid solutions*, J. Phys. Chem. Solids **19**, 35 (1961).

[78] C. Granqvist, R. Buhrman, *Ultrafine metal particles*, J. Appl. Phys. **47**, 2200 (1976).

[79] E. Otto, H. Fissan, *Brownian coagulation of submicron particles*, Adv. Powder Technol. **10**, 1 (1999).

[80] J. Söderlund, L. Kiss, G. Niklasson, C. Granqvist, *Lognormal Size Distributions in Particle Growth Processes without Coagulation*, Phys. Rev. Lett. **80**, 2386 (1998).

[81] G. Margolin, B. Berkowitz, *Continuous time random walks revisited: first passage time and spatial distributions*, Physica A **334**, 46 (2004).

[82] M. Matsumoto, T. Nishimura, *Mersenne twister: a 623-dimensionally equidistributed uniform pseudo-random number generator*, TOMACS **8**, 3 (1998).

[83] M. Luscher, *A portable high-quality random number generator for lattice field theory simulations*, Comput. Phys. Commun. **79**, 100 (1994).

[84] S. Schwyn, E. Garwin, A. Schmidt-Ott, *Aerosol generation by spark discharge*, J. Aerosol Sci. **19**, 639 (1988).

[85] J. Even, *Unterpotentialabscheidung von Ruthenium und Osmium*, Diploma thesis, Philipps-Universität Marburg (2008).

[86] B. Finkle, E. Hoagland, S. Katcoff, N. Sugarman, *Radiochemical Studies: The fission products*, McGraw-Hill Book Company, Inc. (1951).

[87] J. Hakala, et al., *Evolution of the N=50 shell gap energy towards* ^{78}Ni, Phys. Rev. Lett. **101**, 052502 (2008).

[88] U. Hager, et al., *Precision mass measurements of neutron-rich yttrium and niobium isotopes*, Nucl. Phys. A **793**, 20 (2007).

[89] U. Hager, et al., *First precision mass measurements of refractory fission fragments*, Phys. Rev. Lett. **96**, 042504 (2006).

[90] U. Reus, W. Westmeier, *Catalog of Gamma Rays from Radioactive Decay, Part I*, Atom. Data Nucl. Data **29**, 1 (1983).

[91] H. Wollnik, H. Wilhelm, G. Robig, H. Jungclas, *The improvement of a gas-jet system by the use of an aerosol generator*, Nucl. Instr. Meth. **127**, 539 (1975).

[92] Canberra Industries, 800 Research Parkway, Meriden, CT 06450, *Genie^{TM}2000 Spectroscopy Software*.

[93] P. Jardin, et al., *Mono 1000: A simple and efficient 2.45 GHz electron cyclotron resonance ion source using a new magnetic structure concept*, Rev. Sci. Instrum. **73**, 789 (2002).

[94] R. Campargue, *Progress in overexpanded supersonic jets and skimmed molecular beams in free-jet zones of silence*, J. Phys. Chem. US **88**, 4466 (1984).

Danksagung

An dieser Stelle bedanke ich mich bei allen, die mir während des Studiums beigestanden und zum Gelingen dieser Arbeit beigetragen haben:

Zuerst bedanke ich mich bei Klaus Blaum, der bereits zu Schulzeiten mein Interesse für Physik weckte und mich durch seine Vorlesungen für die Penningfallen Massenspektrometrie begeisterte. Trotz seiner Berufung nach Heidelberg, hatte er immer Zeit für mich. Vielen Dank für die Unterstützung und für die Möglichkeit in deiner Arbeitsgruppe mitzuarbeiten.
Ich danke Christian Smorra, Szilard Nagy und Jens Ketelaer, dass sie immer für Fragen zur Verfügung standen und mich immer bei Problemen aller Art tatkräftig unterstützt haben. Vor allem danke ich dafür, dass ihr mich in die TRIGA-TRAP Gruppe aufgenommen habt und mir abseits meiner Diplomarbeit viel über die Penningfallen Massenspekrometrie beigebracht habt.
Mein Dank gilt auch Klaus Eberhardt, der mir immer mit Rat zur Seite stand und ohne den viele Experimente nicht möglich gewesen wären. Außerdem bedanke ich mich bei Julia Even, die ebenfalls eine wichtige Ansprechpartnerin für mich geworden ist.
Des Weiteren danke ich den restlichen Mitgliedern der TRIGA-SPEC Kollaboration: Jochen Ketter, Julia Repp, Konstantin Knuth, Wilfried Nörthershäuser, Christopher Geppert, Jörg Krämer, Andreas Krieger, Frank Herfurth und Michael Block, sowie den übrigen Mitgliedern der MATS-Gruppe für die tolle Arbeitsatmosphäre.
Außerdem gilt mein Dank Rudolf Würfel und Ute Kolb für die TEM Untersuchungen der Aerosole und den technischen Mitarbeitern der Kernchemie sowie den Operateuren ohne die meine Experimente ebenfalls nicht möglich gewesen wären.
Ich bedanke mich bei meinen Freunden für die tolle Zeit während des Studiums und dafür, dass sie immer für mich da waren. Vielen Dank, dass ihr mich während der Diplomarbeit häufig zu Problemlösungen inspiriert habt und dass ich mit euch so viel Spaß hatte.
Ein ganz besonderer Dank gilt meiner Familie. Ich danke euch, dass ihr mir das Physikstudium ermöglicht und mich in den vergangenen Jahren immer unterstützt habt.
Meiner Freundin Jennifer danke ich für die moralische Unterstützung während des Studiums und der Diplomarbeit. Vielen Dank, dass du mir immer zur Seite gestanden und an mich geglaubt hast.